Universidade de Lisboa
Faculdade de Ciências
Departamento de Física

Evaluation of the D-SPECT System: *geometry considerations and respiratory motion*

Débora Sofia Almeida Silva Salvado

Dissertação
Mestrado Integrado em
Engenharia Biomédica e Biofísica
Perfil de Radiações em Diagnóstico e Terapia

2012

Universidade de Lisboa
Faculdade de Ciências
Departamento de Física

Evaluation of the D-SPECT System: *geometry considerations and respiratory motion*

Débora Sofia Almeida Silva Salvado

Orientador interno: Professor Doutor Pedro Almeida, IBEB, FCUL
Orientador externo: Professor Doutor Brian F. Hutton, INM, UCL

Dissertação
Mestrado Integrado em
Engenharia Biomédica e Biofísica
Perfil de Radiações em Diagnóstico e Terapia

2012

To my family

Resumo

O D-SPECT é um sistema de aquisição SPECT (do inglês *Single Photon Emission Computed Tomography*), desenvolvido especificamente para imagiologia cardíaca e está apenas disponível em alguns países no mundo. Este sistema tem uma configuração curva para se adaptar ao lado esquerdo do torso do paciente, que é onde se localiza o coração. É constituído por 9 detectores CZT (cádmio-zinco-telúrio), montados verticalmente e que têm a possibilidade de rodar individualmente sobre o seu eixo. Esta capacidade permite que sejam utilizados diferentes padrões de aquisição, nomeadamente uma aquisição centrada numa região de interesse pré-definida. A rápida amostragem do FOV (do inglês *field of view*) permite tempos de aquisição mais curtos ou menor exposição à radiação. As maiores vantagens deste sistema são a elevada sensibilidade, resolução em energia e resolução espacial, que possibilitam a obtenção de imagens cardíacas com qualidade superior comparativamente às imagens obtidas com sistemas SPECT convencionais.

Assim, devido à sua geometria de aquisição única e ao *design* dos detectores, a sensibilidade, resolução e cobertura angular podem variar ao longo do FOV. Além disso, um possível problema na aquisição da imagem é o posicionamento do coração. Uma vez que os pacientes são anatomicamente diferentes uns dos outros, o coração não estará posicionado no mesmo local do FOV para todos eles, podendo introduzir artefactos nas imagens. Um outro problema é o facto de, com o D-SPECT, não ser possível adquirir *scans* de transmissão, logo não existe informação relativa a mapas de atenuação para efectuar correcção de atenuação. No entanto, este é um ponto crucial, uma vez que os pacientes têm tamanhos e formas diferentes, o que faz com que sejam esperados maiores efeitos de atenuação para pacientes maiores. O movimento do paciente seja ele involuntário, como por exemplo a respiração e os batimentos cardíacos, ou voluntário também impõe alguns problemas na quantificação da imagem SPECT. Em relação a este último ponto, a ausência de sincronismo entre a aquisição da imagem e a distribuição de radiação no paciente podem levar a inconsistências nos dados adquiridos ou a outros efeitos nas imagens relacionados com o tempo. Todos estes problemas influenciam a reconstrução dos dados adquiridos e, em alguns casos, podem mesmo levar à introdução de artefactos nas imagens. Por sua vez, estes artefactos podem ser interpretados como defeitos de perfusão, comprometendo a precisão do diagnóstico clínico.

O objectivo deste estudo é então avaliar o sistema D-SPECT, tanto em termos de parâmetros relacionados com a geometria de aquisição, como em termos de efeitos do movimento da respiração na imagem reconstruída. Em específico, pretende-se investigar se parâmetros como a posição do coração no FOV, atenuação, amostragem angular, tempo de aquisição, padrão de respiração e desvio de fase entre a aquisição e o ciclo respiratório afectam a reconstrução do miocárdio. Assim, esta tese foi dividida em dois estudos em separado, um relativo à geometria de aquisição e outro relacionado com os efeitos do movimento coração devido à respiração.

Como metodologia geral, foram executados os seguintes passos. Para simular a fonte de actividade, isto é, o coração, foi utilizado o *software* NCAT que gera fantomas do torso humano. De seguida, uma ferramenta de simulação desenvolvida na University College of London foi utilizada para estimar as projecções: o Simulador D-SPECT. Esta ferramenta teve de ser modificada para possibilitar o estudo de todos os parâmetros já mencionados. Depois, reconstruiu-se cada simulação com o programa utilizado clinicamente no Institute of Nuclear Medicine, que se baseia no algoritmo de reconstrução OSEM (do inglês *Ordered Subsets Expectation Maximization*). As imagens cardíacas obtidas foram depois co-registadas com uma imagem modelo, reorientadas de acordo com o eixo do coração e analisadas através de gráficos de perfusão (denominados em inglês, *bull's eye plots*) e da análise dos valores de COV (coeficiente de variação), R^2 e NRMSE (erro quadrático médio normalizado, do inglês *Normalized Root-Mean-Square Error*) calculados para cada imagem.

Em relação ao primeiro estudo, foram simuladas 8 posições diferentes do coração no FOV, deslocando todo o fantoma para posições cada vez mais afastadas dos detectores do D-SPECT. Cada simulação foi efectuada com e sem modelação da atenuação. É importante referir que as imagens simuladas sem modelação de atenuação são semelhantes a imagens obtidas após sofrerem correcção de atenuação, pois não incluem os efeitos da atenuação. Por outro lado, as imagens obtidas com modelação de atenuação são mais semelhantes às obtidas na prática, pois não têm correcção de atenuação. Quanto às projecções, estas foram adquiridas sem ruído, com modelação da resolução e com um padrão de aquisição de varrimento simples de 120 ângulos por detector. As imagens foram posteriormente reconstruídas com 7 iterações OSEM.

Os resultados obtidos mostram que a uniformidade e a forma do miocárdio reconstruído são afectadas pela variação da distância miocárdio-detector e pela atenuação. Com atenuação, a actividade decresce com a distância, especialmente para distâncias em que o miocárdio está praticamente fora do FOV. Isto pode resultar de um padrão de atenuação diferente, uma vez que os fotões têm de percorrer trajectórias diferentes no fantoma para chegar aos detectores. Por outro lado, sem atenuação, a distribuição de actividade no miocárdio reconstruído melhora em relação ao obtido com atenuação, mas

piora drasticamente para a maior distância miocárdio-detector simulada. Isto mostra que a atenuação é também um factor a ter em conta na qualidade da imagem obtida. Portanto, estes resultados demonstram a importância do posicionamento do paciente aquando da aquisição da imagem D-SPECT e do desenvolvimento de algoritmos de correcção de atenuação, com o intuito de obter imagens de boa qualidade.

Em relação ao segundo estudo, utilizou-se o *software* 4D NCAT para gerar os fantomas do torso humano. A diferença entre este *software* e o utilizado no estudo anterior é que em vez de se obter apenas um fantoma para efectuar cada simulação, é obtido um conjunto de fantomas (as denominadas *frames* em inglês). Mais precisamente, são obtidos 32 fantomas num ciclo respiratório. Por defeito, o ciclo respiratório simulado tem um padrão sinusoidal e 5 segundos de duração, o que corresponde a uma respiração tidal. Portanto, os 32 fantomas são repetidos consecutivamente para simular aquisições superiores a 5 segundos. Para cada ângulo de aquisição, a respectiva projecção é estimada pela média das projecções dos fantomas ocorridos durante o intervalo de tempo em que o detector está a adquirir nesse ângulo. Todas as simulações foram realizadas com uma aquisição centrada numa região de interesse definida previamente. Os restantes parâmetros das simulações variaram consoante o parâmetro de aquisição avaliado.

Um total de 12 simulações foram realizadas para estudar os efeitos de desfasamento entre a aquisição e o ciclo respiratório. Os resultados obtidos sugerem que um gating respiratório e/ou treino da respiração poderão melhorar as imagens obtidas.

Para estudar os efeitos do parâmetro tempo de aquisição, foram efectuadas 7 simulações com tempos de aquisição diferentes e, para a aquisição de 1 minuto, repetiu-se a simulação com 3 amostragens angulares diferentes. Os resultados obtidos mostram que existe um compromisso entre o tempo de aquisição e a qualidade da imagem reconstruída. Por um lado, é possível reduzir a amostragem angular sem comprometer a imagem reconstruída, diminuindo assim o tempo de aquisição. Mas quando o tempo de aquisição é da ordem da duração do ciclo respiratório, a imagem reconstruída apresenta maiores artefactos.

Em relação ao padrão do ciclo respiratório, 4 simulações com um padrão de respiração sinusoidal e tempos aquisição diferentes foram comparadas com simulações com um padrão de respiração mais real: padrão de expiração lenta. Os resultados obtidos mostram que um padrão de respiração mais regular contribui para uma melhor qualidade de imagem.

No entanto, estes estudos apresentam algumas limitações. O ruído e a dispersão de radiação não são tidos em conta nas simulações realizadas. A influência dos batimentos cardíacos também não está incluída nas simulações, o que poderia contribuir com mais fontes de erro nas imagens cardíacas. No entanto, esta última questão poderia ser resolvida aplicando gating cardíaco. Como trabalho futuro, seria benéfico fazer algumas

alterações ao Simulador D-SPECT de modo a incluir estes efeitos, e também realizar um maior número de simulações do que o apresentado nesta tese, para confirmar os resultados. Além disso, seria também interessante comparar os resultados obtidos com os obtidos com um fantoma físico e investigar diferentes padrões de respiração reais e tamanhos de paciente, e novos padrões de aquisição de imagem.

Por fim, é de referir que apesar dos efeitos da geometria de aquisição, atenuação e movimento da coração devido à respiração serem foco de muitos estudos científicos relativamente a sistemas SPECT convencionais, não existem estudos semelhantes para o sistema D-SPECT. Deste modo, é aconselhável que sejam feitas mais pesquisas nesta área. Contudo, este estudo já contribui para um melhor conhecimento geral do sistema D-SPECT e mostra que os protocolos clínicos e os diagnósticos podem ser melhorados para benefício do prestador de cuidados de saúde e do paciente.

Palavras-chave: D-SPECT, Reconstrução SPECT, Ferramentas de Simulação, Geometria da Aquisição, Atenuação, Movimento Respiratório, Artefactos

Abstract

This thesis focuses the evaluation of a new cardiac-dedicated system only available to a few countries worldwide: the D-SPECT system. It comprises 9 collimated CZT detectors, mounted vertically in a curved configuration that conforms to the left side of the patient's torso. Each detector is able to rotate independently, allowing for the selection of different scanning patterns. The fast sampling yields reduced scanning times or radiation exposure. Due to its novel design and scanning geometry, unexpected time-related effects may occur, and lead to the inclusion of artefacts in the myocardial reconstructed images. These artefacts can be interpreted as perfusion defects, compromising cardiac assessment.

The purpose of this thesis is to investigate critical acquisition parameters of the D-SPECT system, that could lead to artefacts in the reconstructed images. In particular, it was divided into two studies, one regarding geometry-related issues and another related to effects of respiratory motion, namely due to LV-detector distance, attenuation, angular sampling, scanning time, breathing pattern, and phase shift between the acquisition and the respiratory cycle. These issues were tackled using the NCAT software to obtain torso phantoms, a simulation tool to estimate projection data, and the clinical reconstruction procedure to reconstruct these data. Myocardial reconstructed images were assessed via bull's eye plots, and analysis of COV, R^2 and NRMSE values.

Results demonstrated the importance of patient positioning, and attenuation correction algorithms, in order to obtain good-quality images. They also showed the compromise between reduced acquisition times and accurate reconstruction, and suggested that respiratory gating and breathing training could be applied to improve results.

Although these issues have been the focus of several research work for standard SPECT systems, there are no similar studies for the D-SPECT. Consequently further research in this area would be advisable. In any case, this study provides significant findings related to the D-SPECT system operation, and suggests that clinical protocols and diagnoses can be improved, for the benefit of both the healthcare provider and the patient.

Keywords: D-SPECT, SPECT Reconstruction, Simulation Tools, Acquisition Geometry, Attenuation, Respiratory Motion, Artefacts

Acknowledgements

I would like to express the deepest appreciation to both my supervisors Professor Brian F. Hutton, and Professor Pedro Almeida. Professor Pedro Almeida provided the first contact with Professor Brian F. Hutton, and was always supportive and encouraging during the development of this thesis. On the other hand, Professor Brian F. Hutton guided me throughout the project, criticising and encouraging my work. Much I learnt from him, and I consider it an honour to have worked with him at the Institute of Nuclear Medicine (INM), University College of London (UCL).

In addition, I am indebted to Dr Kjell Herlandsson, who guided me on a daily basis. He was always available to discuss ideas, give suggestions, and clarify doubts.

I would like to thank the INM staff for the warming reception and work atmosphere. To Filipa Costa, Stefano Pedemonte, Niccoló Fuin, Maria Holstensson, and Alexandre Bousse, I thank for their companionship, and helpful and enlightening discussions.

It is with immense gratitude that I thank Professor Eduardo Ducla-Soares, not only a professor, but also a friend who believed that I could succeed. His commitment for students of Biomedical Engineering and Biophysics of the Faculty of Sciences of the University of Lisbon (FCUL) is very much appreciated.

I gratefully acknowledge financial support from the LLP/Erasmus Grant, IBEB and INM.

I also wish to thank my closest friends, Marta Dias, Maria João Bigode, Patrícia Ribeiro, Joana Loureiro, André Ribeiro, João Monteiro and Rafael Henriques, who were always there for me; and the Ferreira family to whom I cannot find words to express my gratitude.

Finally a special word to my parents, grandparents and godparents for their dedication and support throughout my life.

Contents

List of Figures

List of Tables

List of Abbreviations

2D two-Dimensional

3D three-Dimensional

4D four-Dimensional

ADC Analogue-to-Digital Converters

AP Anterior-Posterior

AV Atrioventricular

BNMS British Nuclear Medicine Society

bpm beats per minute

BSc Bachelor of Science

CA California

CHD Coronary Heart Disease

COV Coefficient Of Variation

CT Computed Tomography

CZT Cadmium-Zinc-Telluride

ECG Electrocardiogram

EEG Electroencephalogram

EU European Union

FBP Filtered Backprojection

FCUL Faculty of Sciences of the University of Lisbon

FOV Field Of View

FT Fourier Transform

FWHM Full-Width at Half Maximum

HEAP High-Energy, All-Purpose

HLA Horizontal Long Axis

IBEB Institute of Biophysics and Biomedical Engineering

IDL Interface Description Language

INM Institute of Nuclear Medicine

IS Inferior-Superior

LEGP Low-Energy, General-Purpose

LEHR Low-Energy, High-Resolution

LLP Lifelong Learning Programme

LV Left Ventricle

MA Massachusetts

MEAP Medium-Energy, All-Purpose

MEG Magnetoencephalography

MLEM Maximum Likelihood Expectation Maximization

MPI Myocardial Perfusion Imaging

MRI Magnetic Resonance Imaging

MSc Master of Science

NCAT NURBS-based Cardiac-Torso

NURBS Non-Uniform Rational B-Splines

OSEM Ordered Subsets Expectation Maximization

PET Positron Emission Tomography

PhD Philosophiae Doctor

PMTs Photomultiplier Tubes

PSF Point-Spread Function

QPS Quantitative Perfusion SPECT

ROI Region Of Interest

RSNA Radiological Society of North America

SA Short Axis

SPECT Single-Photon Emission Computed Tomography

UCL University College of London

UK United Kingdom

USA United States of America

VLA Vertical Long Axis

WBME Workshop on Biomedical Engineering

Chapter 1

Introduction

1.1 Project Scope

This thesis was submitted in partial fulfilment of the requirements for the Master's Degree in Biomedical Engineering and Biophysics - Radiation in Diagnosis and Therapy, at the Faculty of Sciences of the University of Lisbon (FCUL). It was developed under the LLP/Erasmus Programme, which is an European Union (EU) student exchange programme, at the Institute of Nuclear Medicine (INM), University College of London (UCL), London, United Kingdom (UK), in collaboration with the Institute of Biophysics and Biomedical Engineering (IBEB), FCUL, Lisbon, Portugal.

The main focus of IBEB is on research and post-graduate teaching. They have been supervising both Masters and PhD students, and more recently they started the 5-year BSc+MSc programme in Biomedical Engineering and Biophysics. Research areas include Biophysics and the areas of contact between Physics and Medicine. The current main fields of interest are Nuclear Medicine; processing of EEG, MEG and ECG; MRI and transcranial magnetic stimulation.

Furthermore, the Research Physics Group at INM focus on Medical Physics applied to Nuclear Medicine and Molecular Imaging Science. A wide range of research projects are carried out mainly on the field of emission tomography. The areas of interest include SPECT system design, optimized tomographic reconstruction for PET and SPECT, and multi-modality image analysis applied to clinical research studies in Nuclear Medicine, using combined PET/CT, SPECT/CT, and PET/MRI.

This thesis' research project involved the evaluation of a new SPECT system, the D-SPECT, investigating geometry-related issues and respiratory motion effects in the reconstructed images. Professor Brian Hutton, who is Chair of Medical Physics in Nuclear Medicine and Molecular Imaging Science, was the external supervisor, along with Dr Kjell Erlandsson, senior research fellow at the same institute. The internal supervisor was Professor Pedro Almeida, Head of IBEB and full professor at FCUL.

1.2 Research Aim

SPECT is a nuclear medicine tomographic imaging technique that provides functional information about biological processes.

In a SPECT scan, the patient is administered with a radiopharmaceutical, which contains a specific biochemical compound that has binding properties to certain types of tissues. In addition, the radioactive properties of the radiopharmaceutical generate a distribution of radiation within the body that can be detected by the SPECT system, allowing for the reconstruction of a 3D image. This image carries important information for diagnostic purposes.

The D-SPECT is a recent cardiac-dedicated SPECT system that introduces a novel geometry and image acquisition.

The camera comprises 9 collimated CZT detectors, mounted vertically in a curved configuration that conforms to the left side of the patient torso. Since each detector is able to rotate independently about its own axis, different scanning patterns can be performed focused in a pre-defined ROI. Also the fast sampling yields reduced scanning times or radiation exposure.

The main advantages of this system include great sensitivity, and good energy and spatial resolution, providing cardiac images with superior quality when compared to conventional SPECT systems.

However, due to the novel detector design and sampling, spatial acquisition is limited and patient-specific. Therefore D-SPECT sensitivity, resolution and angular coverage may vary over the FOV. Furthermore acquisition and activity distribution within the patient have different timings due to the unconventional scanning geometry. As a result, mismatches in projection data and other time-related effects may occur.

The overall goal of this project is to evaluate the D-SPECT system, investigating critical parameters that can lead to artefacts in the reconstructed images. In other words, the aim of the project is to fully understand the limitations of this new system, and the effects of such features in the final reconstructed images. To achieve this, the project has been divided into two parts. As an initial approach, some geometric considerations are made, concerning the position of the heart in FOV and the effects of attenuation. This will give support to the development of some methodology and analysis tools. The ultimate aim of the project is to examine the effects of different timings between the acquisition protocol and the patient's respiratory motion, with special concern in parameters such as sampling and scanning time, angular sampling, respiratory cycle pattern and phase shift between acquisition and breathing.

1.3 Thesis Outline

This thesis is divided into six chapters.

Chapter 1 is this chapter. A brief introduction to the supervisors and respective institutions involved in this project is presented, giving an overview of their research focus. It has also presented a scope of the developed work. Additionally, the scope and motivation of this thesis are introduced, and the main objectives are summarized.

Chapter 2 presents background information. It introduces important concepts of SPECT imaging, related to instrumentation, acquisition and reconstruction. A detailed description of the D-SPECT system is given, and some considerations on sources of image degradation are discussed. In addition, the cardiovascular system is described, as well as its assessment via Myocardial Perfusion Imaging (MPI). It also covers the respiratory system and the effects of respiratory motion in the heart, and its evaluation. Furthermore, simulation and analysis tools essential for the developed research are described here.

Chapter 3 presents the developed tools for the simulation and analysis of D-SPECT images.

Chapter 4 presents the first research project: geometry considerations of the D-SPECT system. A comprehensive description of the methods and results is given, followed by the discussion and major conclusions.

Chapter 5 covers the second research project: effects of respiratory motion. Again, a comprehensive description of the methods and results is given, followed by the discussion and major conclusions.

Chapter 6 is a summary of this thesis, including the conclusions drawn from this research and major contributions. In addition, recommendations for related future work are suggested. This chapter is followed by bibliography.

Appendix A and Appendix B present the D-SPECT *Simulator* and the reconstruction interface, respectively.

Chapter 2

Background

2.1 SPECT Imaging

Single-Photon Emission Computed Tomography (SPECT) is a well-established nuclear medicine imaging technique with multiple applications in the field of cardiac imaging[1–3].

In a SPECT scan, the patient is administered with a radiopharmaceutical, which can be injected, ingested, or inhaled. This compound is a pharmaceutically-active molecule labelled with a single-photon emitter, that is a radionuclide tracer that emits one gamma-ray per radioactive decay. The pharmaceutically-active molecule is chosen on the basis of its preferential localization in a given organ, or its participation in a physiological process. The most common radiotracers in cardiac nuclear medicine are thallium (^{201}Tl) chloride, technetium (^{99m}Tc) sestamibi, and technetium (^{99m}Tc) tetrofosmin[4].

The activity of the radiopharmaceutical within the body generates a distribution of radiation that can be detected by the SPECT system, and then reconstructed to create a three-dimensional (3D) tomographic image. Therefore, this 3D image yields functional information about biological processes, important to assess the patient's health state.

2.1.1 Instrumentation

The main components of a conventional SPECT system include the collimator, the scintillation crystal, photomultiplier tubes (PMTs), analogue-to-digital converters (ADC), and the computer for event positioning, energy determination and image display (Fig. 2.1). The source of gamma photons is usually the patient, although a phantom or a source of radiation can be scanned for other purposes than clinical diagnosis.

A SPECT system typically consists of one or more scintillation cameras mounted on a gantry that rotates about a fixed horizontal axis, where the patient is positioned. The spatial resolution is approximately 10 mm with a count rate of 200 to 300 cpm/μCi in

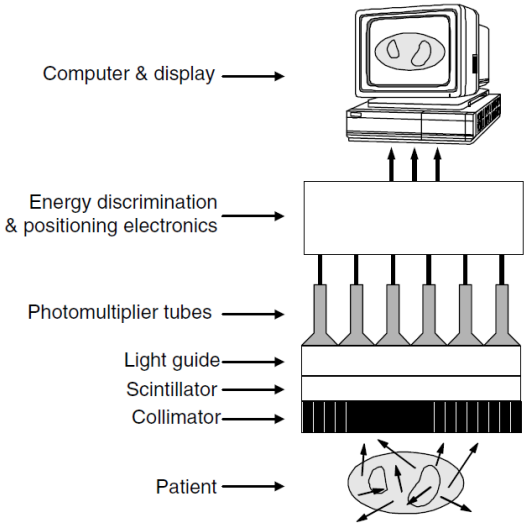

Figure 2.1: Components of a gamma camera. The schematics include a collimator, a scintillator, a light guide, PMTs, electronics for energy discrimination and positioning and a computer for image display. The patient represents the source of activity. Image adapted [5].

the field of view (FOV). The FOV is typically 40 × 50 cm, which covers a large portion of the body of the patient.

The collimator is made of heavy metal septa and holes, which enables it to select preferentially gamma rays travelling in a particular direction. Gamma rays travelling in other directions will be absorbed or highly attenuated. Due to the collimator configuration, the more gamma rays deviate from the selected direction, the more they are attenuated in the collimator material and less is the probability that the gamma ray will reach the scintillation crystal. The probability of detection of a gamma ray by a detector as a function of the distance from the source position is given by the point-spread function (PSF). Septa thickness, collimator thickness and hole size are parameters of the collimator that affect the PSF shape, i.e. full-width at half maximum (FWHM) as well as sensitivity, which is given by the fraction of emitted photons that are detected.

In addition, collimators may have different geometries, such as parallel-hole in which septa are parallel, converging geometry, in which the resulting image is amplified, diverging geometry, in which the resulting image is minimised, and pinhole geometry, in which the image is inverted and magnified or minimised depending on the object position (Fig. 2.2). The design of the collimator depends on the gamma ray energy and the trade-off between photon count sensitivity and spatial resolution. To improve the sensitivity, the collimator hole size can be increased and the hole length shortened so that less photons are absorbed by the collimator. However, spatial resolution is degraded due to the fact that more photons are detected but they are less specific. Spatial resolution also diminishes as the source to collimator distance increases. Taking these factors into

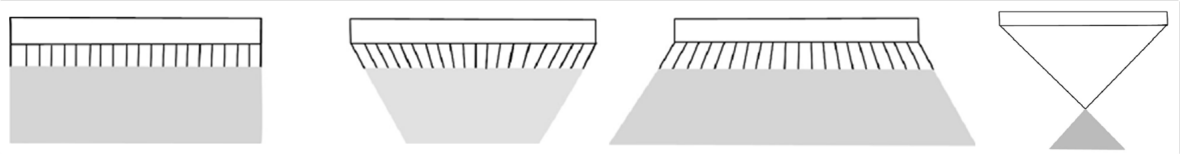

Figure 2.2: Different types of collimator. The schematics shows **a** the parallel-hole collimator; **b** the converging collimator; **c** the diverging collimator and **d** the pinhole collimator. The blue-shaded area corresponds to the field of view of the collimator. Image adapted [6].

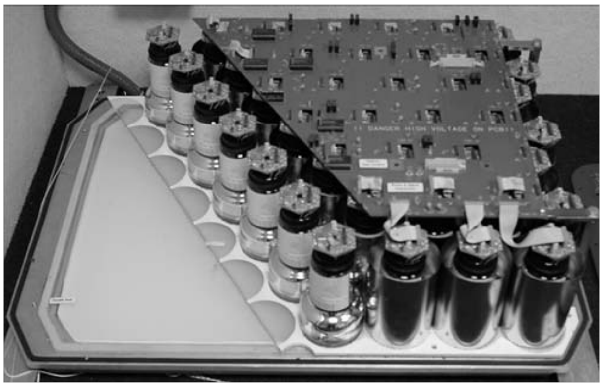

Figure 2.3: Scintillation detector of a gamma camera. The image shows a scintillation crystal, light guide, PMTs, magnetic shielding and signal-processing electronics [5].

account, different collimator designs have been developed. For example, for parallel-hole collimators there are LEHR (low-energy, high-resolution), LEGP (low-energy, general-purpose), MEAP (medium-energy, all-purpose), and HEAP (high-energy, all-purpose) collimators.

Regarding the scintillation crystal, it converts gamma ray energy into visible light. The most common scintillation crystal is the sodium iodide activated with thallium - NaI:Tl - which has high light output proportional to the absorbed energy: a 140 keV gamma ray yields 5000 visible light photons. Additionally NaI:Tl has moderate energy resolution, providing a means to discriminate against scatter radiation, which degrades image quality. Other advantages of this crystal include a good photopeak efficiency which depends on the crystal thickness, and the fact that it can be manufactured in many sizes and shapes. On the other hand, NaI:Tl is hygroscopic and actively absorbs water vapour from the air, resulting in a loss of transparency of the crystal to the scintillation. Furthermore, it has a long persistence of the scintillation, and consequently a dead time in which the crystal cannot detect accurately all the events, providing a limited count rate.

Next to the scintillation crystal is the matrix of PMTs (Fig. 2.3) that converts visible light into an electrical signal. Each PMT is a vacuum tube with a photocathode that emits electrons when hit by visible light. These electrons are accelerated against successive dynodes that will amplify the signal due to a series of cascade-events. The

size of the resulting electrical signal is directly proportional to the energy deposited by the gamma ray.

Finally, PMT output signals are digitized by ADCs and then processed to determine the energy and location of each detected event. The energy is given by the sum of the PMT signals in the proximity of the event. Regarding the location, signals are weighted with a number that accounts for the physical location of each PMT. Then, PMT signals that exceed a pre-determined threshold are summed and if the event falls within the selected energy window, it is accepted as a valid photon count and recorded.

2.1.2 Acquisition

The goal in SPECT data acquisition is to acquire a sufficient set of projection data in order to reconstruct a tomographic image of the tracer activity distribution. To accomplish this, the patient needs to be positioned in the centre of the FOV, so that the camera can rotate around the patient, acquiring 2D projections from multiple slices and angles.

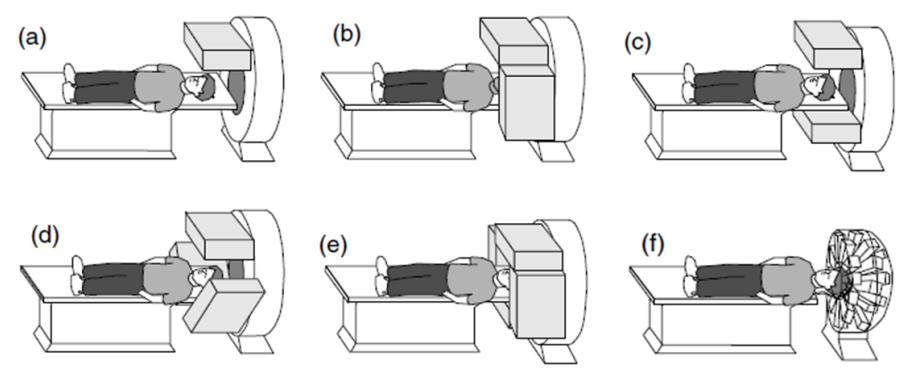

Figure 2.4: SPECT system configurations. Schematics are shown for: a) single head, b) orthogonal heads, c) opposed heads, d) three heads, e) four heads and f) multiple small-FOV detectors[5].

A SPECT detection system can have different configurations, regarding the number of gamma cameras that are incorporated: one, two, three or four detector heads or multiple small-FOV scintillation detectors (Fig. 2.4). In the case of a two camera system, cameras may be positioned orthogonal or opposite to each other. The increased number of detector heads provides a greater sensitivity to the system, because the number of detected gamma photons increases. As a result, the acquisition time is reduced.

Regarding the way the gantry moves, there are two different procedures for data acquisition: continuous acquisition and step-and-shoot acquisition. In the first, data are acquired as the detectors continuously rotate around the patient. In the latter, instead of moving continuously, the gantry rotates with a certain angular step, and only in each step, data are acquired. For each angular stop, 64×64 or 128×128 projections are acquired. Typically projection data are acquired over a full 360^o arc, although perfusion

studies are usually acquired over 180^o, which minimizes effects of attenuation[7].

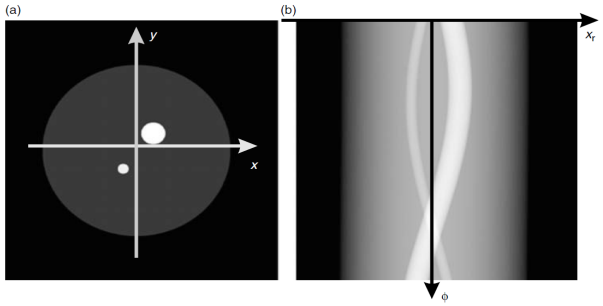

Figure 2.5: Sinogram. Image of a slice of a phantom (left) and the corresponding sinogram (right). Image adapted[8].

After the acquisition protocol, the resultant data are projection data. Usually, projection data are displayed in a single plot called sinogram (Fig. 2.5). The horizontal axis corresponds to projection bins, the vertical axis corresponds to the projection angle, and the resulting plot has a sine wavelike shape. Each wave corresponds to a (x, y) location whose distance from de centre of rotation determines the wave amplitude and angular location determines the wave phase. These measured projection data will then be used by reconstruction algorithms to generate a tomographic image.

2.1.3 Reconstruction

The process of obtaining a SPECT image is based on the acquisition of 2D projections of a 3D volume to reconstruct a contiguous stack of 2D slices of the distribution of activity. The main problem with the reconstruction process is that an infinite number of tracer distributions can yield the same projection. Otherwise stated, photons emitted at different depths, but along the same direction, are detected by the same detector. Since the distance travelled by the photon is not known, the amount of information given by only one projection is insufficient to reconstruct an image. However, the number of possible solutions reduces and becomes more alike as the number of angular positions of the detector increases.

Assuming that the distribution of emitted counts f in the FOV is known, as well as a projection operator A, the distribution of the detected counts g is given by Eq. (2.1):

$$g = Af \tag{2.1}$$

In the reconstruction process, the system of equations described in Eq. (2.1) must be solved to find f, given the measured data g. Two main approaches can be used to solve this system of equations - analytic and iterative reconstruction algorithms.

Analytic methods typically consider the reconstruction process as an inverse problem, estimating the inverse of a formula that represents the image formation process. Thus,

solutions can be computed very quickly and efficiently. However, the resulting images may contain some artefacts due to the fact that attenuation and noise are not suitably accounted for.

On the other hand, iterative reconstruction methods rely on a criterion that can be seen as the strategy used to select the best estimation of the true image, and an algorithm that repetitively attempts to estimate this solution. Usually this is accomplished by statistical estimation methods and probabilistic models which can include factors that contribute to image quality, such as noise, detector response characteristics, scatter and attenuation.

In the next sections, there is a brief description of one analytic reconstruction algorithm - Filtered Backprojection (FBP) -, and two iterative reconstruction algorithms - Maximum Likelihood Expectation Maximization (MLEM) and Ordered Subsets Expectation Maximization (OSEM).

Filtered Backprojection

The backprojection operator, obtained by the inversion of the Radon Transform, can be defined mathematically by:

$$f(x,y) = \int_0^{\pi} g(s,\theta)\mathrm{d}\theta \tag{2.2}$$

where f is the activity distribution, g is the distribution of the detected counts along projection s taken at angle θ.

As Eq. (2.2) suggests, the reconstructed image represents the accumulation (integral) of ray-sums of the object projections acquired over π radians. In the backprojection process, each measured *bin* value is attributed to all pixels that project onto that *bin*, and not only to pixels where the source is, because its location is not known. This process is repeated for as many angles as those acquired, to obtain the reconstructed image. However, the resultant image is blurred due to the fact that the backprojection operation is not the exact inverse of the projection operation. In order to solve this problem, usually a ramp filter is applied first, and then projection data are backprojected - Filtered Backprojection (FBP). The ramp filter gives a weight proportional to the frequency of each sinogram's component, reducing the amplitude of the low frequency components. As a result, image noise increases due to the enhancement of high-frequency components. One way to correct for this effect is to combine the ramp filter with a low-pass filter, such as the Shep-Logan filter. Therefore, some low frequencies as well as high frequencies are attenuated, improving the image quality. However, the selection of the cutoff frequency for this filter is not trivial. A low cutoff value may smooth the reconstructed image, resulting in blurred details and a loss in spatial resolution, while a higher cutoff value may increase the amount of image noise. Thus, there is a trade-off

between noise reduction and spatial resolution.

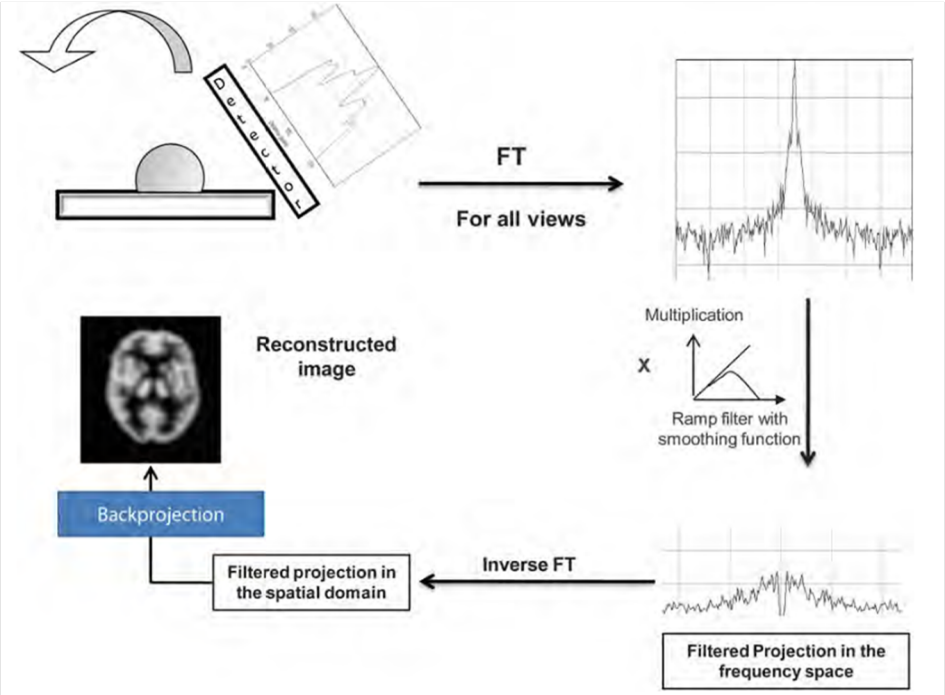

Figure 2.6: FBP reconstruction algorithm. After the acquisition, FT is applied to all views and the result multiplied by a ramp filter with a smoothing function. Then the inverse FT is applied to filtered data and all views are backprojected and superimposed to obtain the reconstructed image. Adapted from[9].

Usually the reconstruction process is performed in the frequency domain instead of the spatial domain, using the central section theorem. This theorem assumes that the 2D Fourier Transform (FT) of the activity distribution of a tomographic image can be seen as the 1D FT of a projection view of that image taken at a specific angle. Therefore the reconstruction process is easy to implement (Fig. 2.6), and the algorithm is fast. First the 1D FT of each projection profile - acquired data - is calculated. Then, in the frequency domain, these data are multiplied by a ramp filter combined with a smoothing filter. The inverse FT is computed, hence filtered data return to the spatial domain. The next step is to backproject these data in order to obtain an estimate of the measured activity distribution.

Note that in a real SPECT system, the number of acquired projections is finite. This angular sampling influences the reconstruction process. When the number of angular projections is low, the reconstructed image will present a streak artefact (Fig. 2.7). But, as more projection angles are added to the reconstruction process, the better is the resulting estimation of the real activity distribution (Fig. 2.7). Moreover the FBP method assumes angular symmetry of projections, a linear and shift-invariant system, and it does not incorporate a noise model. However, it is known that SPECT images are affected by depth-dependent spatial resolution, attenuation and scatter.

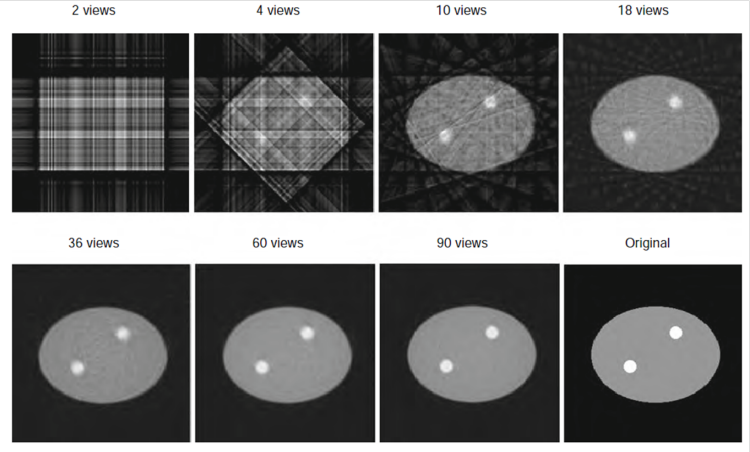

Figure 2.7: Effects of viewing angles in FBP. On the right inferior corner, the original image is shown. All the remaining images correspond to FBP-reconstructed images using different numbers of viewing angles. Image adapted[9].

Maximum Likelihood Expectation Maximization

Proposed by Shepp and Vardi for Emission Tomography[10], MLEM is an iterative reconstruction method based upon the Poisson statistical nature of the radioactive decay. Unlike FBP, MLEM is more robust since it comprises models of the physics of SPECT imaging that account for system spatial resolution, attenuation and scatter effects, and collimator septa penetration.

The main goal of the method is to find the best estimate of the activity distribution given the measured projection data. Therefore, the algorithm is divided into two steps: the expectation step and the maximization step. In the first step, it estimates the mean number of detected counts f given the mean number of projection counts p using the likelihood function based on the Poisson distribution. Typically the logarithm function is applied to simplify calculations - log-likelihood function. Then, the second step is to find an estimate of the detected counts $\hat{f}$, given the projection data, that makes the measured outcome most likely. Now, assuming that the detector D is divided into d units, and the object to reconstruct B is divided into b boxes or voxels, the current estimate of $\hat{f}$, $\hat{f}^{[k+1]}$, is given as a function of the previous estimate $\hat{f}^{[k]}$ by Eq. (2.3):

$$\hat{f}^{[k+1]}(b) = \hat{f}^{[k]}(b) \frac{1}{\sum_{d=1}^{D} p(b,d)} \sum_{d=1}^{D} \frac{n^*(d)}{\sum_{b'=1}^{B} \hat{f}^{[k]}(b')\, p(b',d)} p(b,d) \tag{2.3}$$

where $n^*(d)$ is the number of counts detected in each detector unit d and $p(b,d)$ is the probability or system matrix, which describes the probability of each emission from voxel b be detected in the detector unit d. This matrix can capture depth-dependent resolution, position-dependent scatter in the patient, and depth-dependent attenuation.

Evaluating Eq. (2.3), it is possible to conclude that MLEM is a series of projection

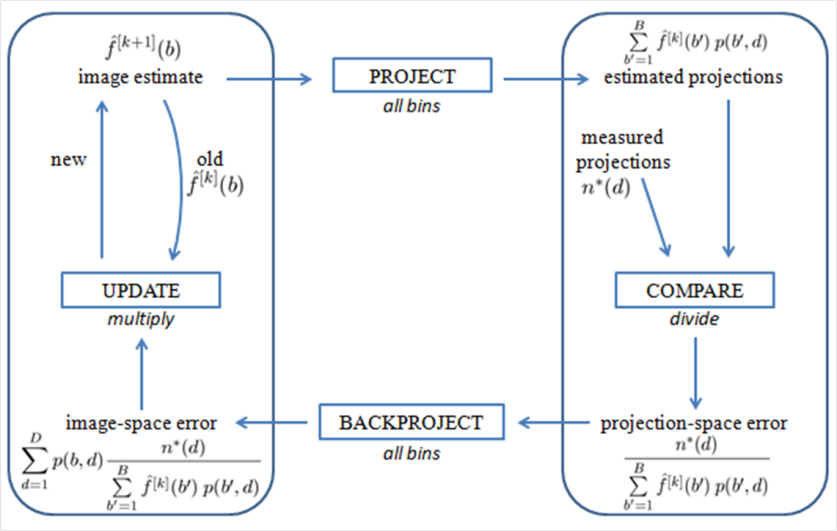

Figure 2.8: MLEM reconstruction algorithm. Starting with an initial image estimate, project all bins and compare the estimated projections with the measured projections. The next steps are to backproject the error, and multiply it by the estimate to obtain a new one. Iterate until the algorithm reaches convergence. Image adapted[11].

and backprojection operations. In each iteration k, the new image estimate $\hat{f}^{[k+1]}$ is obtained projecting the previous image $\hat{f}^{[k]}$ and comparing it with the measured projection by taking the ratio between them; the resulting correction factor is then backprojected and used to update the current estimated image[12] (Fig. 2.8).

The selection of the Poisson distribution as the premise for the detection measurements ensures that convergence is verified, even though several iterations are needed to reach it. Usually, prior knowledge is used to introduce constraints in the model capable of accelerating the convergence of the algorithm. Moreover, the Poisson formula yields a statistically consistent estimate, with good noise properties, and imposes non-negative pixel values, which is in agreement with the assumption that activity cannot physically have a negative value.

A disadvantage of MLEM is the level of noise, which increases as the number of iterations increases. In the MLEM algorithm, noise is correlated with the signal, thus noise amplitude is lower in regions of low counts. In order to solve this, one of two approaches may be taken: regularization which includes control of the difference between neighbouring pixels throughout the reconstruction process, and post-reconstruction filtering, for example with a Gaussian filter. Either one will reduce the noise level in the reconstructed image[13].

Ordered Subsets Expectation Maximization

This iterative reconstruction method has the same concept of projecting and backprojecting as the MLEM. However, instead of using the whole set of projection data to update the reconstructed image, it uses subsets of projection data. These subsets have

an equal number of non-contiguous projections. For example, considering a SPECT acquisition of 64 projections and a total number of 8 subsets, each subset would have 8 projections distributed accordingly: the first subset would be $1, 9, 17, 25, 33, 41, 49, 57$, the second subset $5, 13, 21, 29, 37, 45, 53, 61$, and so on, to obtain more information.

The fact that the OSEM algorithm uses subsets of the total projection data instead of all data makes it much faster than MLEM. For an m number of subsets, OSEM needs only n iterations to get close to the same point of convergence as MLEM at $m \times n$ iterations[14]. This is the main benefit of OSEM, the degree of acceleration increases with the number of subsets. Post-filtering needs to be applied as in the case of MLEM. Furthermore, attention must be provided to the degree of acceleration. Sometimes noisy images appear after a single iteration, since the algorithm has already reached a point of convergence equivalent to many iterations. This issue can be solved using a larger subset size in order to reduce the degree of acceleration[13]. As a consequence, the stopping point of this algorithm is now equivalent to a smaller number of iterations.

The OSEM algorithm operates as follows. At each sub-iteration, the current image is updated using only one subset, and the result is used to start the following sub-iteration. When all subsets are used, a full iteration is completed. The algorithm iterates until it reaches a certain level of convergence and post-filtering is applied to reduce noise.

In conclusion, analytic and iterative algorithms can be used to reconstruct SPECT images taking into account the advantages and disadvantages of each method, and the trade-off between the accuracy provided by iterative methods and the efficiency given by analytic methods.

2.1.4 State-of-the-Art: D-SPECT

Generally, in a conventional SPECT system, only 0.02% of the photons emitted from the heart are collected due to collimation. This low sensitivity results in acquisition times of 10 to 20 minutes[15] or high doses of radiopharmaceuticals administered to the patient. Consequently efforts have been made to develop new cardiac-dedicated SPECT systems[16], such as the D-SPECT.

The D-SPECT system was first introduced at the 2005 RSNA meeting in Chicago by Spectrum Dynamics, Caesarea, Israel. Since then, several D-SPECT systems have been implemented in the United States of America, but only one in England, Thailand and Japan, three in Canada, and eight in France[17]. Specifically developed for cardiac imaging, D-SPECT introduces a novel photon-collection and scanning geometry, providing a good sensitivity combined with a fast acquisition time.

The D-SPECT camera comprises 9 collimated, pixelated cadmium-zinc-telluride (CZT) detector columns, mounted vertically in a curved configuration to conform to the left side of the patient's torso (Fig. 2.9). Each of the 9 detection columns consists of

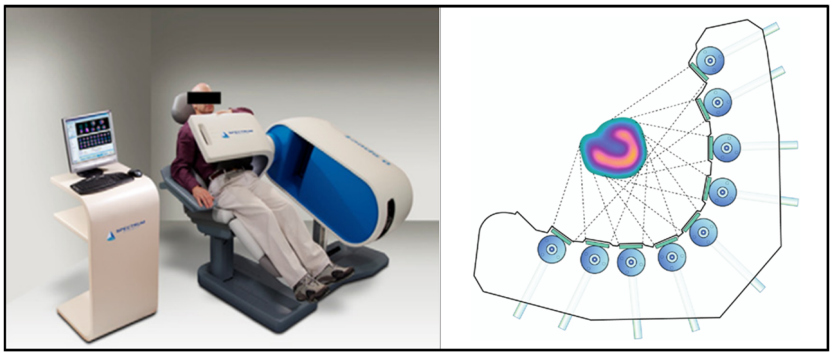

Figure 2.9: D-SPECT system. On the left, the figure shows the positioning of the patient and the camera. On the right, details of the configuration of the 9 detectors and the region of the heart are shown. Image adapted[15,19].

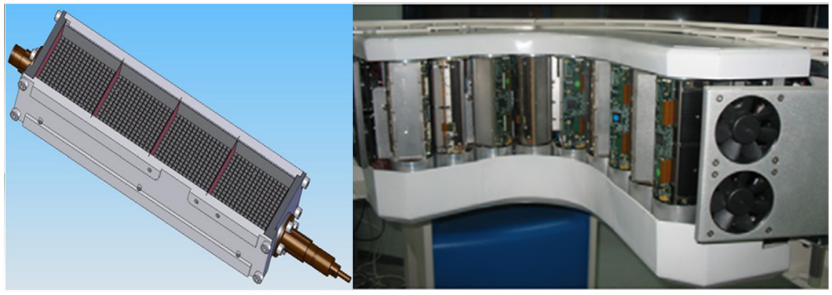

Figure 2.10: D-SPECT detection system. Details of one detector (on the left) and the whole camera (on the right). It is possible to observe that each detector is mounted vertically, and that the camera has a curved configuration. Image adapted[15].

1024 (16×64) CZT elements (Fig. 2.10), with 5 mm of thickness and square geometry ($2.46\ mm \times 2.46\ mm$)[15]. Collimator holes and CZT elements are adjusted so that there is one CZT pixel for each collimator hole, being the intrinsic resolution of the system defined by the size of the CZT pixel. The advantage of solid-state CZT detectors is their superior energy resolution when compared with NaI:Tl crystals. Also they can operate at room temperature and they can be pixelated. This compact nature of CZT detectors provides movement that would not be achievable with conventional thick crystals and large photomultiplier tubes, as well as the miniaturization of the camera dimensions[18]. This leads to an ergonomically optimized camera for both the patient and the operator.

Regarding the D-SPECT collimation system, tungsten parallel-hole collimators have larger square holes, 2.26 mm, and shorter length, 21.7 mm, than conventional lead parallel-hole LEHR collimators, whose holes measure 1.6 mm and 45 mm, respectively[15]. Consequently, the accepted solid angle is 8 times larger than that of conventional collimators, providing a better count sensitivity, although having relatively poor geometric resolution[18]. Additionally, the stopping power of tungsten is greater than that of lead[15] allowing for the use of thinner collimator septa, which provides an increased useful detector area.

One great advantage of the D-SPECT system is that each detector is able to

rotate independently around its central axis with programmable angular orientation, up to a maximum of 110^o [18]. Furthermore, each detector can acquire data stepwise or continuously, giving the possibility to perform different scanning patterns focused on a pre-defined ROI, with a 10-second temporal resolution [15]. It is also important to mention that all detectors will not scan in the same direction. If detectors number 2, 4, 6 and 8 are scanning clockwise, the remaining detectors, numbers 1, 3, 5, 7 and 9, will be scanning counter clockwise.

During the acquisition, the D-SPECT system focuses the sampling on the heart of each patient, yielding a patient-specific image acquisition (Fig. 2.9). This is called a region-centric acquisition. First, the patient is placed in a semi-upright position with the left arm above the detector, or in a supine position with the left arm up. In both ways, the detector is positioned parallel to the patient's chest, as close as possible to the torso. Then a 10-second pre-scan is performed in the sweep mode, which means the acquisition covers the whole FOV, and a preliminary image of the activity distribution is obtained to ensure the heart is in the FOV. If the heart is not in the FOV, the patient is re-positioned. When the patient is well positioned, a region of interest (ROI) is defined by the operator in the camera interface to set the motion pattern and the scanning angle limits for each detector. The way the scanning pattern algorithm works is the following: it determines which detector is the closest to the ROI, then it calculates the angular sampling for this detector taking into account that 80% of the views must be taken from inside the ROI limits. In general, this results in a sampling of 0.5 degrees per view. The angular sampling for the remaining detectors is set to be the same. Usually, the number of views per detector is 60 per scan, which produces a sinogram with 120 projections per detector. In conclusion, each detector will spend more time acquiring data from the ROI compared to the sampling in the remaining FOV, maximizing the number of acquired counts from this region [15]. The main reason to still acquire data from outside the ROI is to avoid truncation effects. After the scanning pattern calculation, image acquisition begins. Detectors will scan the whole FOV, but mostly the ROI, and then the whole system rotates by 9°so as to fill in sampling gaps, and a new scan is performed (Fig. 2.11).

The reconstruction process uses an iterative reconstruction algorithm, the OSEM, and is divided in two stages. After choosing 32 subsets regarding the structure of the D-SPECT and the scanning pattern, a number of OSEM iterations is performed. These are called pre-model iterations. Then data are fitted to a model of the left ventricular wall, and the resulting image is used as the starting point for new OSEM iterations [18]. This time, these iterations are called post-model iterations. In addition, inter-iteration filtering is applied by convolution with a smoothing kernel consisting of two convoluted triangular kernels. At the end of the reconstruction process, a Gaussian filter is applied,

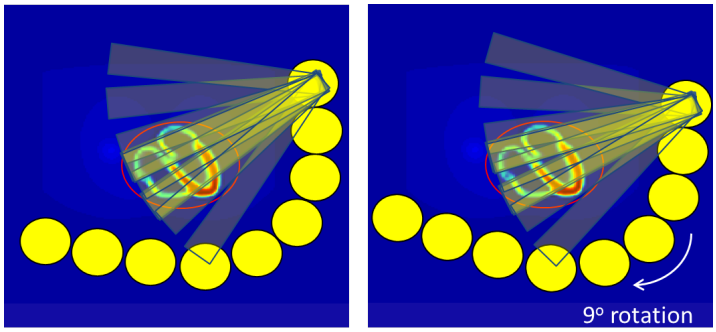

Figure 2.11: Schematics of D-SPECT's clinical scan. The red circle corresponds to the ROI, and light yellow rectangles represent each acquired angle. The operation of only detector is displayed. A first region-centric scan is performed, then the whole system rotates 9°, and a new scan is performed.

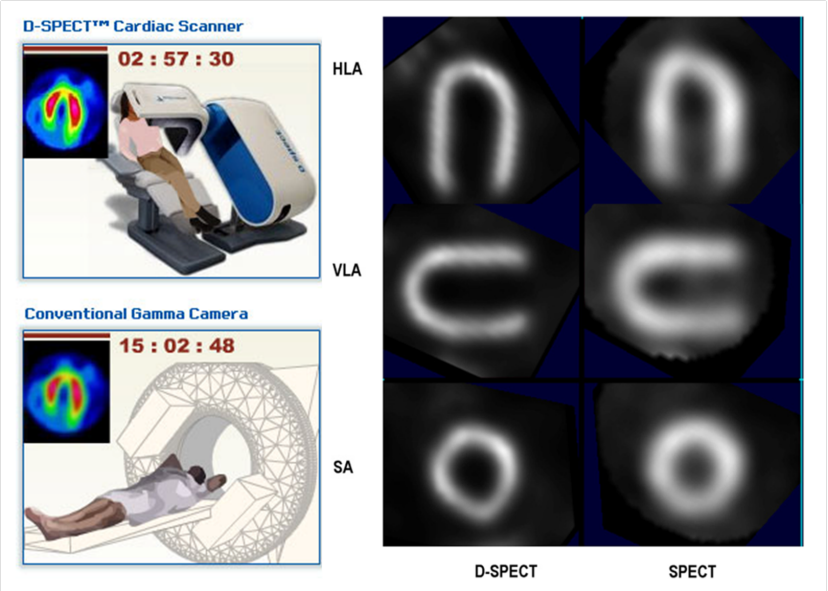

Figure 2.12: SPECT and D-SPECT reconstructed images. On the left, schematics of both D-SPECT and conventional systems, with the respective acquisition time and cardiac reconstructed images. On the right, cardiac images of an anthropomorphic torso phantom scanned with the D-SPECT system and with a conventional SPECT system, they are shown in the three heart axes. Image adapted [15,20].

as well as a non-linear filter to remove hot-spots by detecting and smoothing local maxima [15].

The reconstruction algorithm of the D-SPECT includes a model of the collimator geometry that takes into account the probability of emission of a gamma photon from a certain point (x, y, z) relative to the detector, creating a probability map estimation [15]. However, attenuation and scatter modelling are not included, nor it is possible to obtain intrinsically co-registered attenuation coefficient maps, as a CT scan cannot be performed simultaneously. Having an accurate model for the reconstruction, the loss in spatial resolution due to large-hole collimators is restored in a process called resolution recovery [19]. Due to the non-linear properties of the reconstruction algorithm, reconstructed spatial resolution is variable and object-specific [15].

To conclude, the D-SPECT system offers images of the heart with high quality compared to conventional SPECT systems (Fig. 2.12). The main advantages include great sensitivity, and good energy and spatial resolution, combined with a fast region-centric scanning, providing a means to perform dynamic SPECT acquisitions, and use multiple radionuclides for multidimensional mapping of disease processes. Furthermore, D-SPECT allows decreased scanning times or reduced radiation exposure by lowering the dose of the radiotracer.

2.1.5 Sources of Image Degradation

Factors degrading SPECT imaging propagate through the reconstruction process and can create artefacts in the final tomographic image. Consequently, the acquired projection data may not accurately describe the activity distribution of the administered radiopharmaceutical. Some examples of sources of image degradation will be discussed in this section. It is important to note that the extent of degradation varies with the energy of the emitted photons, the kinetics of the radiopharmaceutical, and the patient scanning time.

Photon Attenuation and Scatter

Photons emitted by the administered radiopharmaceutical will interact within the patient as they pass through different tissues, but only those who escape the body are counted as a measured projection. For the range of energies important to SPECT, photons may interact via photoabsorption, Compton scattering or Rayleigh scattering, but mostly via Compton scattering.

Photon attenuation (Fig. 2.13-a) refers to interactions where the incident photon is completely absorbed or deflected[21]. The degree of attenuation of photons depends on the photon energy, tissue composition and density, and length of the path between the point of emission and the point of detection[22]. For example, photons will be less attenuated when interacting with lungs or soft tissue in relation to interactions with bone. As a result, attenuated photons will not contribute to the image formation as expected, as the number of available counts is reduced, causing non-uniform image artefacts[14]. Attenuation artefacts in cardiac studies may be due to, for example, breast attenuation, lateral chest wall fat attenuation and diaphragmatic attenuation.

To correct for this effect, patient-specific attenuation maps have to be obtained in order to calculate the attenuation that photons emitted from a given location in the patient and detected at a given angle in the detector experience[14]. These attenuation maps, usually derived from CT scans, include patient-specific information on the spatial distribution of attenuation coefficients, and they need to be co-registered with the acquired image so as to obtain a good match between activity and tissue distributions.

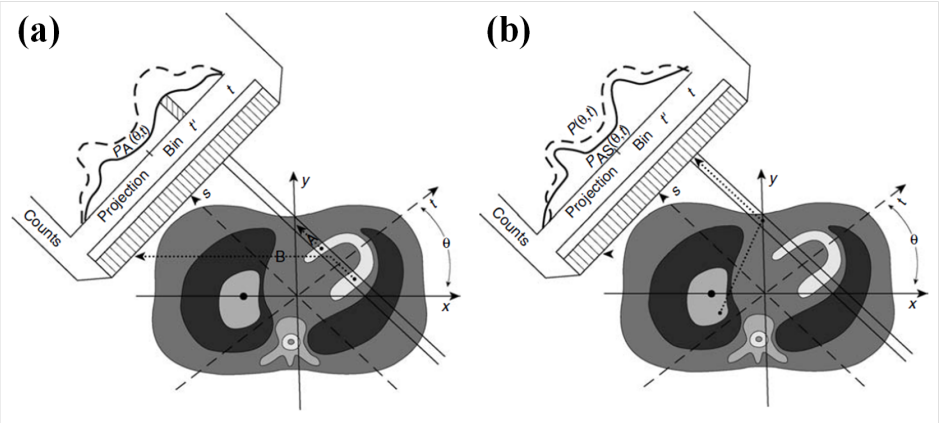

Figure 2.13: Impact of photon attenuation and scatter. In both figures, the dashed line corresponds to the ideal distribution of photon counts and the solid line corresponds to the distribution of photon counts with the effects of photon attenuation (a) and scatter (b). In figure (a), photon A is stopped due to photoabsorption and photon B is scattered so that it is not detected. In figure (b), a photon scattered from the liver is detected in the incorrect projection bin. Image adapted [14].

Photon scatter (Fig. 2.13-b) refers to photons that are deflected from their original path when interacting with collimators, PMTs or surrounding materials. These interactions can occur with or without loss in energy. In SPECT imaging, the dominant mode of interaction is Compton scattering, in which photon energy is reduced [14]. Photons with a small deflection angle and loss of energy will be detected but incorrectly positioned because of their wrong spatial information. Consequently, projection and tomographic images will have poor image quality due to the loss in resolution and contrast [23]. The amount of scattered photons depends on photon energy, source depth and distribution, and tissue composition [22].

Using energy windowing, it is possible to reduce the amount of scattered photons that are detected. Limits for the energy window are set in a way that mostly non-scattered photons are accepted as photon counts. However, it is not possible to eliminate scatter due to Rayleigh scattered photons, since they do not loose energy during the interaction [14]. In addition, even Compton scattered photons are hard to distinguish from primary photons by energy discrimination when the loss in energy is small due to the finite energy resolution of the SPECT system [23].

Collimator Penetration

Collimator penetration is also a factor of image degradation. Although the collimator is designed to select photons travelling in a specific solid angle, there is always a small probability for a photon to penetrate the collimator septa and be detected, due to the exponential characteristics of photon attenuation [22]. These photons will be incorrectly positioned, contributing to a poor image quality.

The use of a collimator with thicker septa reduces the amount of misleading photons,

decreasing collimator penetration effects[22]. However, the sensitivity of the system decreases due to the greater amount of attenuated photons. Therefore there is always a compromise between system sensitivity, spatial resolution and collimator penetration. Another method to handle collimator penetration is to model this effect and include it as a collimator-response function in the iterative reconstruction process[22]. Nevertheless, this modelling may not always be practicable.

Distance-dependent Spatial Resolution

The spatial resolution of a SPECT system depends on the distance from the source to the collimator and the parameters that describe the collimator, such as hole diameter and shape, and septa thickness and length.

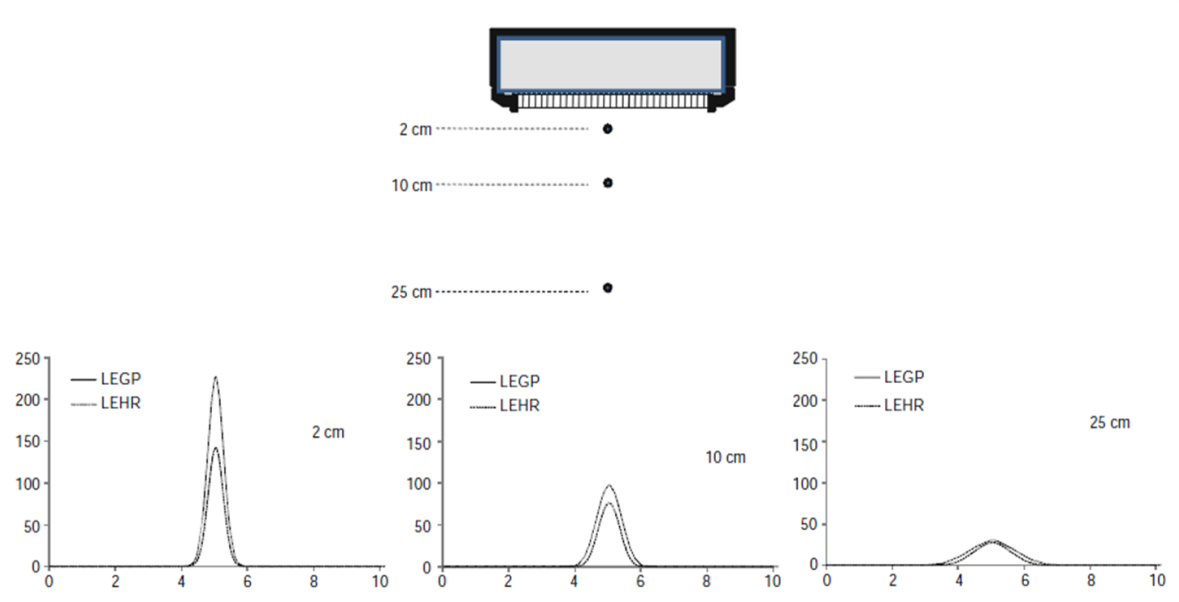

Figure 2.14: Distance-dependent spatial resolution. Simulated point spread functions for three point sources located at distances 2 cm, 10 cm and 25 cm from the collimator surface. Results are shown for both LEGP and LEHR collimators. Image adapted[24].

As the source-to-collimator distance increases, the collimator acceptance cone increases as well. Consequently the positioning of each event will be spread out over a large number of voxels during the reconstruction, so that the number of counts per voxel will not accurately correspond to the activity distribution of the radiopharmaceutical, also known as partial volume effect. As a result, the spatial resolution degrades with distance (Fig. 2.14), leading to a blurred image with poor contrast, which will affect the ability to distinguish small lesions with moderate lesion-to-background activity ratios as well as region boundaries[24]. For a LEHR collimator, this broadening of the FWHM due to the effects of distance-dependent spatial resolution is less pronounced because photons are more attenuated[24]. However, the sensitivity of the system decreases, i.e. the measured count rate is lower.

Statistical Noise

Noise is also present in the acquisition of SPECT images. The problem with noise is not only that it degrades the quality of the reconstructed image, but also the fact that it is amplified during the reconstruction process[25].

The process of photon detection is affected by statistical noise due to the randomness of the photon history. The noise distribution of a planar image, as the photon emission distribution, follows a Poisson distribution with variance equal to the sum of the counts in a selected ROI[22]. As a consequence, a sufficient long acquisition time and a high administered activity must be used to improve image quality. Image noise also depends on the selected matrix size and slice thickness, as well as the acquisition time per projection and the number of projections[22]. Therefore, acquisition parameters need to be optimized for each study.

Dead time

The SPECT system has a finite sampling rate, which accounts for the time the front-end component needs to detect an event and the time the data-processing component needs to accept and store the event. When the incoming data rate is too high compared to the capacity of the system to process it, a fraction of the incoming data will be ignored because of the lack of time. Thus dead time refers to the time the system needs to process an event, during which the system cannot accept a new one. Consequently, the measured count rate will be lower than the true count rate, and as the true count rate increases, so does the error between the measured and the true count rate[26].

Physiologic and patient motions

Another cause of image degradation is physiologic and patient motion. Patient motion occurs especially with long acquisition times because it is difficult for the patient to maintain the same position during the scan. The result is a loss in spatial resolution and/or the formation of artefacts in the projection and tomographic images. These movements can be avoided, for example, providing a more comfortable position for the patient or reducing the scanning time.

Cardiac and respiratory movements are physiological, and unlike patient motions, these movements cannot be avoided. Even if gated SPECT is performed, due to the fact that breathing and myocardial contraction have different frequencies, the resulting image will be blurred[22]. In addition, this motion may contribute to reduced counts in the anterior and inferior walls of the heart[22].

2.2 Function and Assessment of the Heart

2.2.1 The Heart and Cardiovascular System

The heart is a blunt cone-shaped organ, with approximately the size of a closed fist. It is responsible for generating the blood pressure, route the blood, ensure one-way blood flow and the regulation of blood supply.

Located in the mediastinum, which is the midline partition of the thoracic cavity, the heart lies between the lungs, posterior to the sternum and anterior to the vertebrae column (Fig. 2.15). Approximately two-thirds of the heart's mass lies to the left of the sternum's midline due to its oblique direction: the base is directed posteriorly and superiorly, and the apex is directed anteriorly and inferiorly, pointing towards the left hip.

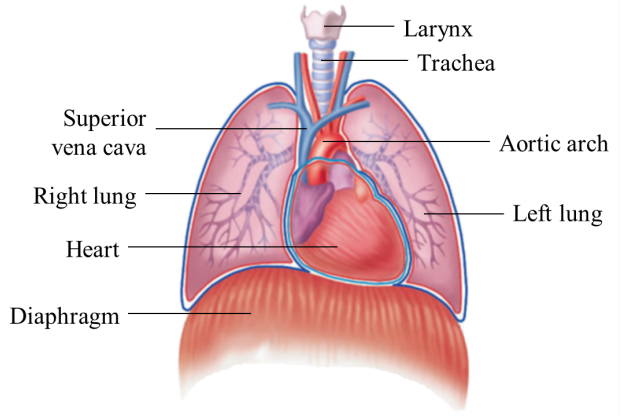

Figure 2.15: Location of the heart in the thorax. The heart lies between the lungs, and is displaced to the left of the midline. Image adapted [27].

Surrounding the heart is the pericardium, a double-layered membrane that provides protection and anchorage.

The heart wall includes three layers: the epicardium, the myocardium and the endocardium. The epicardium is the outer layer of the heart wall and corresponds to the serous pericardium. The myocardium is the thick middle layer composed of cardiac muscle, which is responsible for the heart contraction and conducting system. Finally, the endocardium is the inner layer of the heart wall and is composed of simple squamous epithelium and connective tissue, facilitating the flow of blood through the heart.

As shown in Fig. 2.16, the heart has four chambers: two atria located superiorly and two ventricles located inferiorly. Each atrium is connected to the corresponding ventricle via the atrioventricular valve. The right atrioventricular valve is also called tricuspid, and the left atrioventricular valve is also called bicuspid or mitral valve. On the right side of the heart, the superior and inferior vena cava, along with the coronary sinus, enter the right atrium. In addition, the right ventricle opens to the pulmonary arteries

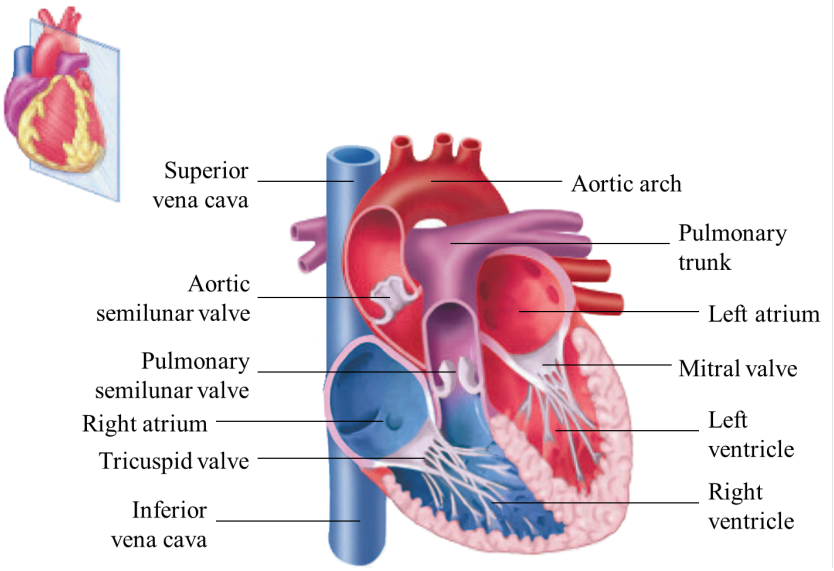

Figure 2.16: Internal anatomy of the heart in a frontal plane cut. Major blood vessels, and heart chambers and valves are labelled. Image adapted[27].

through the pulmonary semilunar valve. On the left side, the pulmonary veins enter the left atrium and the left ventricle opens to the aortic artery through the aortic semilunar valve. Separating the right atrium from the left atrium, as well as the ventricles, is the septum.

Cardiac muscle has an important property called autorhythmicity. Being self-excitable, cardiac muscle cells are able to repeatedly generate spontaneous action potentials that will trigger heart contraction. The conduction system of the heart (Fig. 2.17), which transmits electric signals through the heart, begins in the sinoatrial (SA) node, which sets the pace. The electrical signal then spreads through the atria to the atrioventricular (AV) node, resulting in the contraction of the atria. Once in the AV node, the signal is transmitted to the bundle of His, and then spread to the left and right bundle branches, ending in the Purkinje fibres, and leading to the contraction of the ventricles.

The propagation of the electrical signal can be detected and recorded externally, being the tracings commonly called electrocardiogram (ECG). In normal conditions, the ECG has a special shape (Fig. 2.18) that repeats with a certain pace during the acquisition. The signal is composed of essentially two waves, P and T, and one complex, QRS. The P wave corresponds to the depolarization of the atria and consequently their contraction, the QRS complex corresponds to the depolarization of the ventricles and contraction, and the T wave corresponds to the repolarization of the ventricles, which is their relaxation period. The repolarization of the atria happens at the same time as the depolarization of the ventricles, but with much smaller amplitude. Therefore it is masked by the QRS complex.

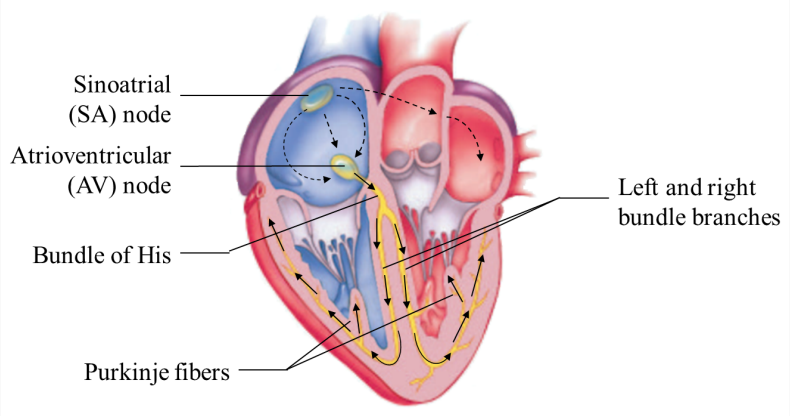

Figure 2.17: Conducting system of the heart. The black arrows represent the electrical signal path. Image adapted[27].

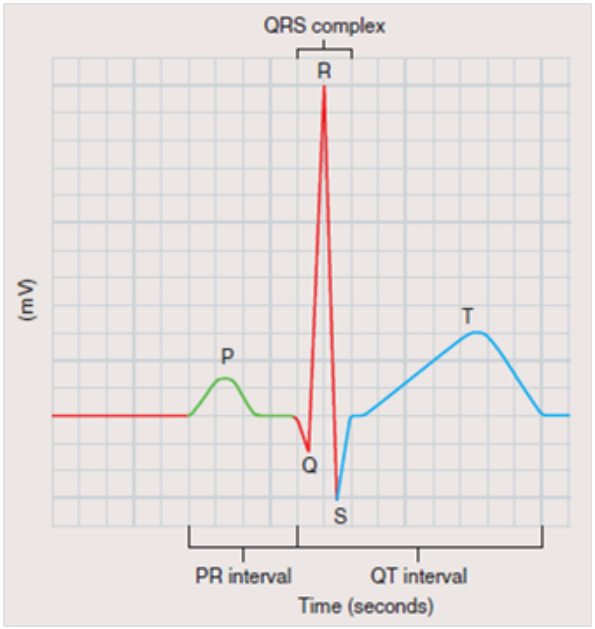

Figure 2.18: Electrocardiogram. The waves and intervals are labelled. Each square corresponds to 1 mV in the vertical direction and 0.04 seconds in the horizontal direction. Image adapted[27].

Regarding the blood flow, the supply chain can be divided into three routes: pulmonary circulation, systemic circulation and coronary circulation. The pulmonary circulation refers to the circulation of blood between the heart and the lungs, in order to oxygenate the blood. The systematic circulation refers to the circulation of the blood between the heart and the rest of the body, delivering oxygen and nutrients. Finally the coronary circulation refers to the circulation of blood through the coronary blood vessels, which supply the heart muscle tissue.

The heart pumps the blood at a rate of approximately 75 *bpm* (beats per minute). Each cardiac cycle lasts 0.8 seconds and consists of atrial systole, that is, contraction, simultaneous atrial diastole, i.e. relaxation, and ventricular systole, and ventricular

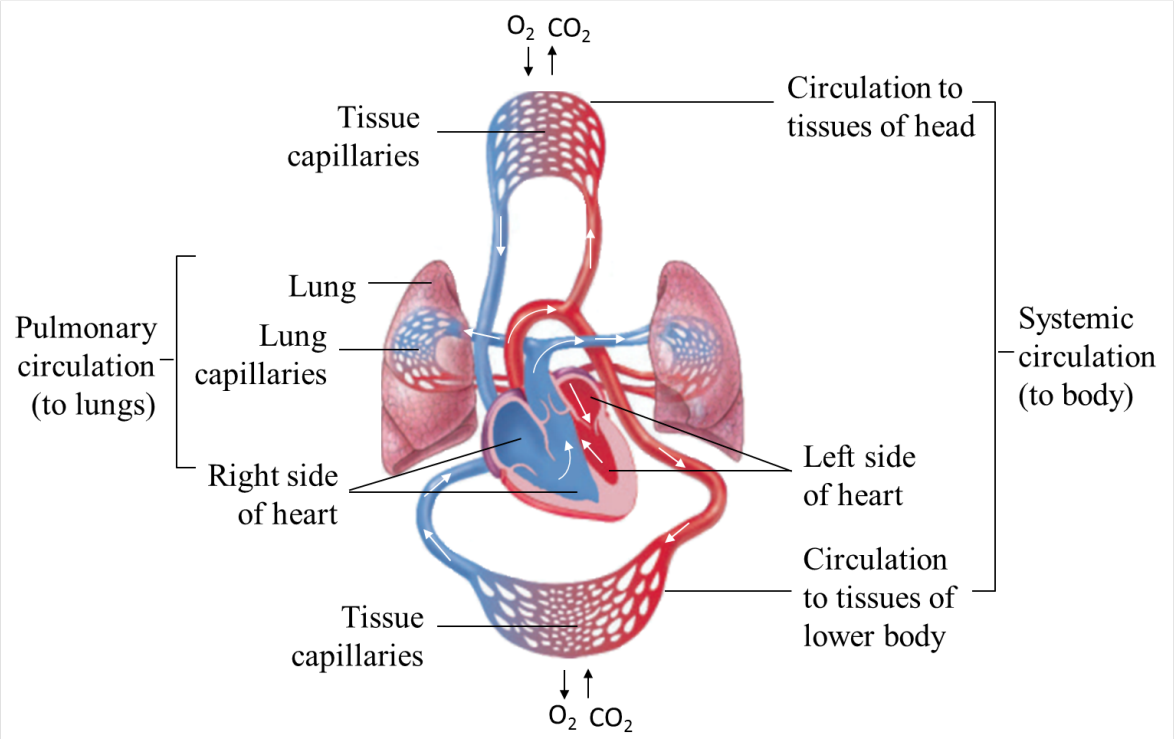

Figure 2.19: Systemic and pulmonary circulation. Deoxygenated blood is represented in the colour blue and oxygenated blood in red. White arrows represent the blood flow. Image adapted[27].

diastole. In more detail (see also Fig. 2.19), blood from the systemic circulation enters the right atrium via the superior and inferior vena cava. The blood is then passed through the tricuspid valve to the right ventricle. Contraction of the right ventricle closes the tricuspid valve and opens the pulmonary semilunar valve. This allows the blood to flow into the pulmonary arteries, and eventually to the lungs, where gas exchange occurs. Then blood returns to the left atrium through the pulmonary veins, and is passed through the mitral valve to the left ventricle. Again, contraction of the ventricle causes the mitral valve to close and the aortic semilunar valve to open. This allows the blood to enter the aorta and be distributed to the body tissues.

2.2.2 Myocardial Perfusion Imaging

Coronary heart disease (CHD) is one of the main causes of death in England with more than 65 thousand deaths in 2010[28]. In Europe, approximately 1.95 million people die every year of CHD[29].

CHD occurs when coronary arteries fail to supply adequate circulation to the cardiac muscle and surrounding tissue, leading to angina or myocardial infarction[30]. This happens because plaque, which is a substance composed of fat, cholesterol, calcium and other contents of blood, builds up inside the coronary arteries (Fig. 2.20) and, over time, it hardens and narrows, or even blocks, the blood flow in coronary arteries[31].

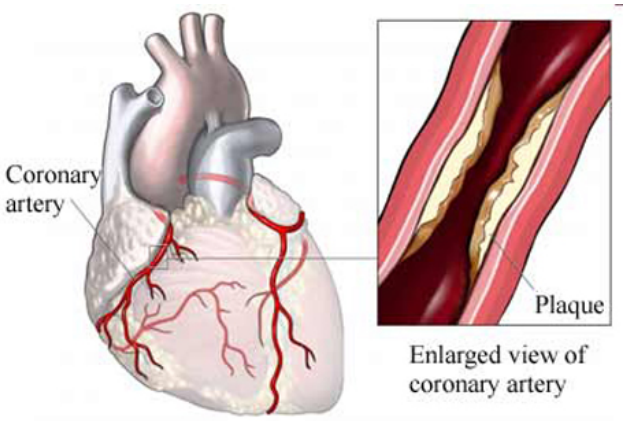

Figure 2.20: Causes of Coronary Heart Disease. The images displays the heart and an enlarged view of a coronary artery with plaque. Image adapted[32].

SPECT myocardial perfusion imaging (MPI) is widely accepted as a non-invasive technique to assess cardiac physiological state[23]. In an MPI SPECT study two sets of images are acquired: one after a stress test, in which the patient perform exercise on a treadmill or stationary bike, or takes some medication that induces stress, and another in a rest state[33]. These two sets of images provide useful information in the assessment of coronary flow, abnormal heart tissue and left ventricular function.

The most common radioisotopes used in cardiac imaging are ^{99m}Tc and ^{201}Tl. In each scan, the patient receives a dose of 24 to 36 mCi in the case of ^{99m}Tc-based perfusion agents, or a dose of 2.5 to 3.5 mCi when using ^{201}Tl, considering an average 70-kg patient[34]. Data acquisition can be performed with a dual-head SPECT system aimed at the patient torso (Fig. 2.21-a). The two detector heads are positioned in an orthogonal configuration, i.e. separated by 90^o, and the patient is placed in a supine position. Each detector stops 32 or 64 times in a 180^o orbit, and although the maximum practical scan time is 30 minutes, usually a 12- or 15- minute scan is performed. Furthermore, the most commonly employed collimation is the parallel-hole, LEGP for ^{201}Tl and LEHR for ^{99m}Tc, and regarding the energy window, 140 keV is applied for ^{99m}Tc and 70 keV for ^{201}Tl[34].

Projection data is often filtered before the reconstruction process, using a low-pass filter such as the Hanning or the Butterworth filter, to reduce noise[34]. Then reconstruction is performed with the FBP or an iterative algorithm. After this, tomographic images of the heart are analysed.

The raw data can be displayed in the cine mode (Fig. 2.21-d). Some types of artefacts are easier to detect in sinograms than in the reconstructed images[34]. But physicians essentially analysed the reconstructed images of the heart.

In order to compare stress and rest images of a patient's heart, and also to compare images between subjects, reconstructed images are reoriented into the left ventricle frame

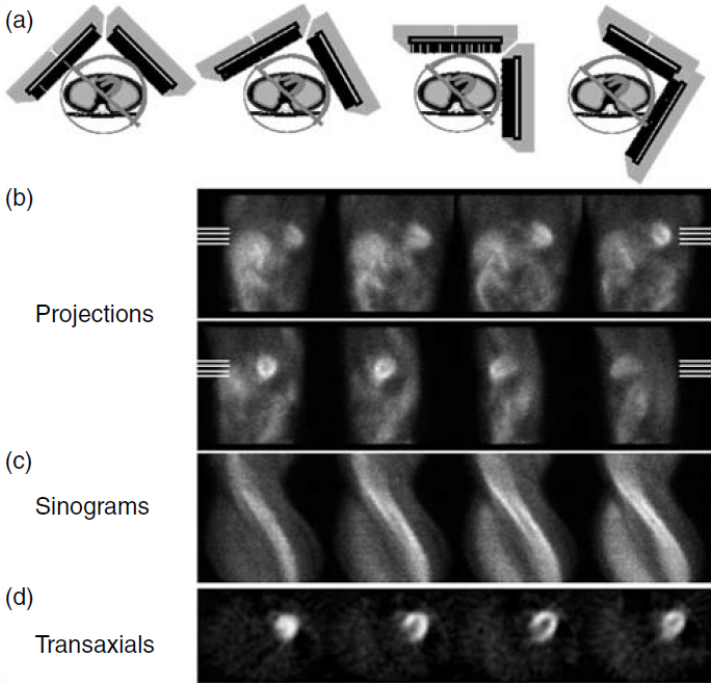

Figure 2.21: Cardiac SPECT data. a) corresponds to a schematic of the camera positions over 180^o, b) shows the localization of the acquired projections in the human torso, c) shows the corresponding sinograms and d) the reconstructed images in the transaxial view[5].

of reference, instead of the body's referential. Three views are defined perpendicular to each other: the short axis (SA), the vertical long axis (VLA), and the horizontal long axis (HLA) (Fig. 2.22). SA images cut through the left ventricle from the apex to the base, HLA images cut through the left ventricle from the posterior wall to the anterior wall, and VLA images cut the left ventricle from the septal wall to the lateral wall (Fig. 2.22).

Regarding the analysis and quantification, there are a number of procedures that are usually followed. In general, cardiac images are normalized to the maximal pixel in the ventricle[34], so that different protocols and scans of different patients can be compared. Also, radial plots and polar plots can be determined, which give additional information about myocardial function[35,36]. Using these plots, parametric images can be generated to show the combined results for the rest and stress scan, for example, blackout, severity and reversibility maps[34]. Commonly the reporting relies not only on the physician interpretation of the cardiac image, plot or map, but also on the comparison of such representation with a database of normal subjects.

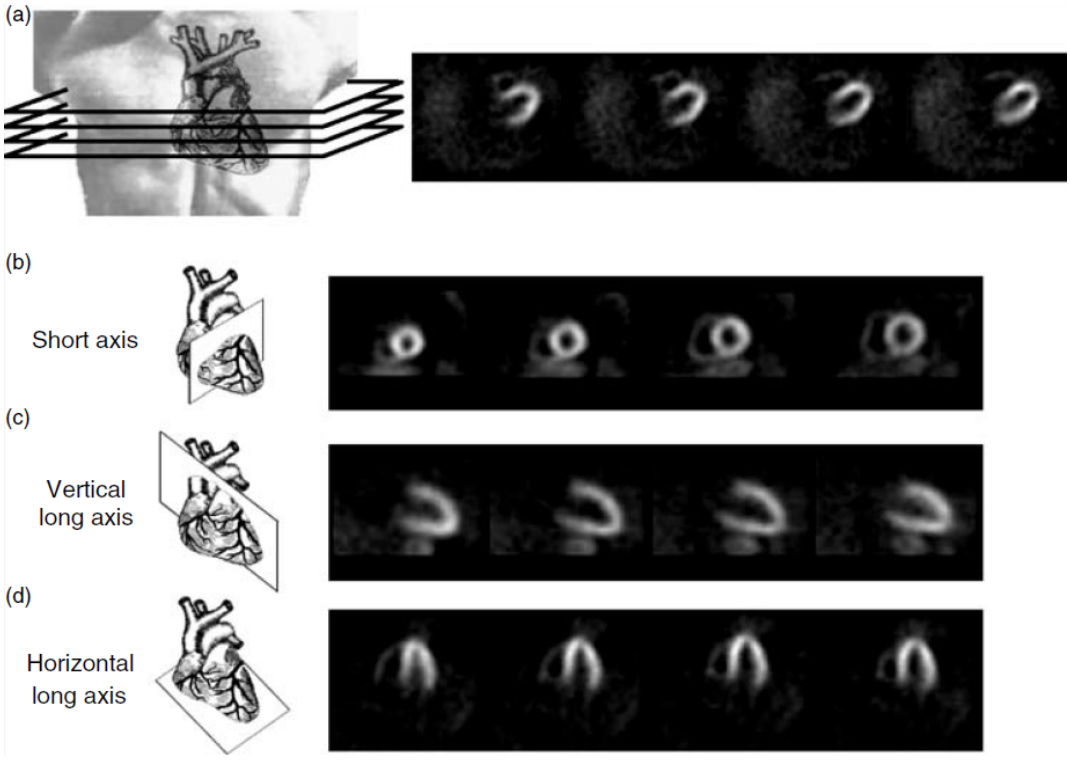

Figure 2.22: Standard heart orientation for the display of cardiac SPECT studies: SA, HLA and VLA[5].

2.3 Respiratory Motion of the Heart and SPECT Artefacts

2.3.1 Respiratory System

The respiratory system is crucial for the gas exchange, which is the caption of oxygen and release of carbon dioxide. Moreover, it is responsible for the regulation of blood pH by changing blood carbon dioxide levels, voice production due to air movement past the vocal cords, olfaction as it takes airborne molecules into the nasal cavity, and protection against pathological organisms by preventing their entry and removing them from respiratory surfaces.

The main elements of the respiratory tract are the nasal cavity, the pharynx, the larynx, the trachea, the bronchi and lungs (Fig. 2.23). This is where the air flows and, ultimately, gas exchange occurs. Additionally, the diaphragm and the muscles of the thoracic and abdominal walls are responsible for the respiratory movement, which creates the necessary pressure changes for the airflow.

Respiration is an involuntary action which combines successively inspiration and expiration movements: inspiration is the inflow of air and expiration is the outflow. The muscles of the inspiration are the diaphragm, the external intercostals, pectoralis

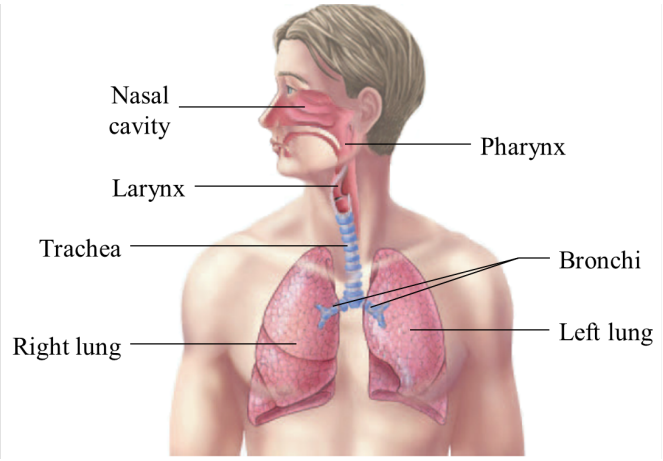

Figure 2.23: Respiratory system. The main elements of the respiratory tract displayed in a coronal cut of head and thorax: nasal cavity, pharynx, larynx, trachea, bronchi and lungs. Image adapted [37].

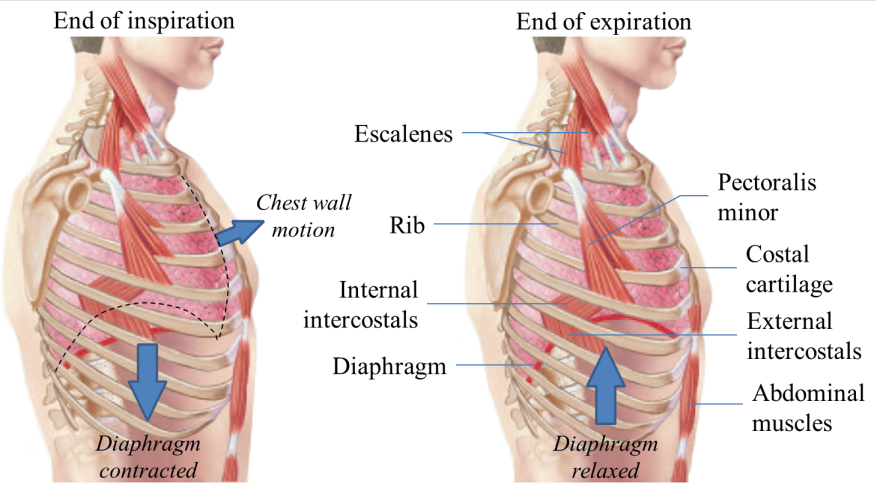

Figure 2.24: Effect of inspiration and expiration muscles on thoracic cavity. On the left, a) shows the muscles at the end of inspiration and, on the right, b) shows the muscles at the end of expiration. The thoracic cavity has different volumes on both images. Image adapted [37].

minor and scalenes. On the other hand, the muscles involved in the expiration are the abdominal muscles and the internal intercostals.

During quiet inspiration, the diaphragm contracts and the abdominal muscles relax, allowing the re-positioning of the abdominal organs as the central tendon moves downwards, typically 10 to 20 mm [38], and the diaphragm flattens (Fig. 2.24-a). Due to the contraction of the diaphragm, external intercostals, pectoralis minor and scalenes, the lower ribs are elevated and consequently the costal cartilages allow lateral rib movement. All these changes induce not only lateral expansion of the thoracic cavity and consequently the lungs, but also an increase in the anterior-posterior and superior-inferior axes of the thoracic cavity, resulting in the flow of air into the respiratory tract. When the diaphragm and external intercostals relax, passive expiration occurs (Fig. 2.24-b). The volume of the thoracic cavity decreases passively due to the elastic

properties of the thorax and lungs, and the air flows out of the respiratory tract. In addition, internal intercostals and abdominal muscles may also contract to help pushing abdominal organs and the diaphragm to their pre-inhalation position, during an active exhalation.

Intuitively, the diaphragm is a key factor in the respiration process. It is a dome-shaped muscle that lies approximately in the transverse plane, separating the thoracic cavity from the abdominal region (Fig. 2.25). It is directly attached to the heart and lungs in the superior surface and to the liver and stomach in the inferior surface. Therefore it has a number of apertures to permit the passage of structures between the thorax and abdomen, such as the aortic artery, the esophagus, the inferior vena cava, among others. The base of the diaphragm attaches to the inner circumference of the inferior thoracic cavity, i.e. sternum, ribs and lumbar vertebrae. The central portion of the diaphragm is composed of connective tissue and is called the central tendon.

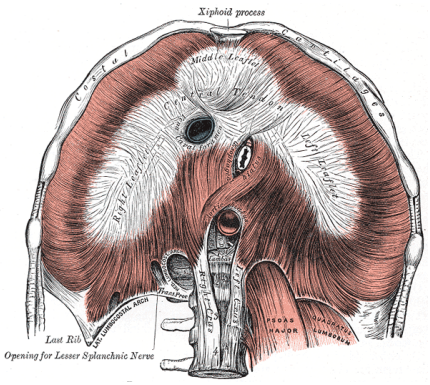

Figure 2.25: Diagram of the anatomy of the diaphragm. The image is an inferior view of the diaphragm. Some characteristics and surrounding organs are labelled. Image adapted [39].

The respiratory cycle is given by the motion of the thoracic cavity and lungs, and usually has a period of 5 seconds. It has approximately the form of a sine wave but with a constant period after each wave (Fig. 2.26-a). In normal breathing, lung volume increases approximately 20%, whereas in deep inhalation it can increase up to 4 times that of normal breathing [38], therefore changing the magnitude of the breathing pattern. Furthermore breathing pattern can vary in period, baseline, regularity between different imaging sessions and between patients [38]. In fact, the breathing pattern (Fig. 2.26) and consequently diaphragm and chest wall motions depend on factors such as posture, which can be supine or upright, breathing type, that is using the chest or abdomen, depth of breathing, that refers to normal, deep or shallow breathing, gender and health status. As a result, motion of internal organs is also affected, specially the heart and abdominal organs. For the abdominal organs, motion is predominantly in the superior-inferior direction, with minimal displacement in the anterior-posterior and lateral directions: less than 2 mm [41].

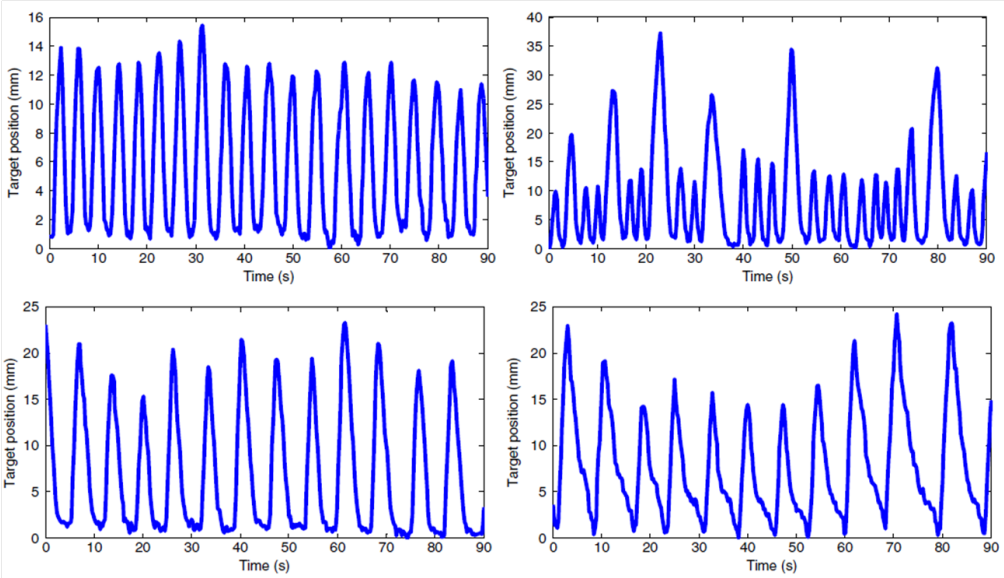

Figure 2.26: Different respiratory patterns. Position of a target in a patient's lung for different respiratory patterns: a) is normal breathing, b) is irregular breathing, c) is extended end-of-exhale, and d) is forced exhale. The y-axis is in *mm* and the x-axis in seconds. Image adapted [40].

2.3.2 Respiratory Motion of the Heart

As explained in the previous section, the heart is positioned in the thorax superior to the diaphragm. Therefore, when the diaphragm moves due to respiration, the heart is one of the internal organs that is most affected. This movement is called the respiratory motion of the heart, and has been the focus of many studies [42–45]. During inhalation, the heart is translated downwards in the IS direction. In 1999, Danias *et al.* evaluated the relationship between the IS motion of the left main coronary artery and the dome of the right hemidiaphragm during free breathing [42]. The acquired MR images showed that the respiratory displacement of the left main coronary artery is consistent with that of the dome of the right hemidiaphragm, although there is intra- and inter-subject variable correlation [42].

In addition, the heart is not only affected by the diaphragm motion, but also by the motion of the chest wall. The relation of the heart with the chest wall makes the former translate anteriorly in the AP direction during inhalation. Nevertheless this motion is much smaller than that induced by the diaphragm [45], because the degree of motion of the chest wall and the interaction between the chest wall and the heart is small.

Although the primary component of the respiratory motion of the heart is in the IS direction, the heart also suffers translation in the AP (described previously) and LR directions and rotations in those three directions [44,45], as studied by Keegan *et al.* (2002) and Shechter *et al.* (2004). Keegan *et al.* (2002) measured the displacement of the right coronary artery origin in the SI, AP and LR directions as a function of diaphragm motion, using breath-hold 3D MR acquisitions [44]. Their results showed

that there is inter-subject variability in the motion of the right coronary artery on those three directions[44]. Similarly, Shechter *et al.* (2004) quantified the respiratory motion of the heart by tracking the coronary arteries displacement in a free-breathing cine-angiogram[45]. They measured a mean translation of the heart of $4.9mm$, $1.3mm$ and $0.4mm$ in the SI, PA and LR directions, respectively, as well as a mean rotation of 1.5^o, 1.2^o and 0.7^o in the LR, PA and IS directions, respectively[45].

Regarding the nature of the respiratory motion of the heart, it is approximately rigid-body, with little deformation. In 2002, McLeish *et al.* studied the nature of the motion of the heart during respiration, measuring the translation, rotation and deformation of the walls of the heart chambers and along the right coronary arteries in MR images[46]. Their analysis showed that the heart moves as a rigid-body, predominantly in the IS direction. Furthermore translation in the two orthogonal directions and rotations were also observed, as well as some deformation[46]. The extent of this non-rigid deformation was subject-dependent, and affected mainly the left ventricle at the apex and the right atrium and associated coronary arteries[46].

Since the motion during exhalation is different to that of inhalation, there are some hysteresis effects, such as the delay in the heart motion in relation to the motion of the diaphragm[43]. In order to investigate the correlation between the displacement of the heart and that of the diaphragm during free breathing, Nehrke *et al.* (2001) used multi-navigator technology and MR imaging on their measurements[43]. They observed a good correlation between heart and diaphragm motion, but the motions presented a certain delay[43]. When analysed, the hysteretic loops had different paths for inhalation and exhalation, and were strongly subject-dependent[43].

2.3.3 Effects of Respiratory Motion during Cardiac SPECT

The motion of internal organs is a critical factor for the quality of thorax and abdominal imaging. Generally motion of the imaged object results in the downgrading of image quality[47–49], as the blur increases and the contrast decreases. Therefore small structures or defects will be difficult to detect. Moreover some artefacts, which are difficult to distinguish from pathological variations, may also be introduced in the image leading to clinical misinterpretation[50]. Motion is also a problem in radiotherapy planning, where dose distribution is restricted to the tumour in order to spare healthy tissue. So work in this field has also made great contributions in the study of motion effects in imaging. However, for the purpose of this thesis, only the effects of respiratory motion during cardiac SPECT will be addressed.

In a cardiac SPECT scan, respiratory motion, as well as myocardial contraction and patient motion, will change the position of the heart in relation to that of the detectors. Consequently the acquired projections will be blurred or will not match, contributing

to a poor image resolution and a misleading distribution of the radiopharmaceutical. Also, it is important to note that due to the length of the scan, typically 12 to 15 minutes, motion effects in the acquired data is unavoidable. Pretorius *et al.* (1999) studied the changes on apparent localization of perfusion agents due to several factors[51], including respiratory motion. They found that simulated SPECT images incorporating respiratory motion had some effects on the localization of perfusion agents, mainly on the inferior and anterior wall of the myocardium, as well as on the lateral wall for the case of deep breathing, but had no impact on the apex[51]. Furthermore Bitarafan-Rajabi *et al.* (2009) studied the effects of respiratory motion on simulated ECG-gated SPECT data[52]. They demonstrated that myocardial perfusion is lower for the basal-inferior, mid-inferior, apical-inferior, basal-septal and mid-septal segments of the myocardium and depends on the amplitude of the respiratory motion[52].

Another problem introduced by respiratory motion in myocardial SPECT is the misalignment and mismatch between transmission and emission data. When applying attenuation correction algorithms to the emission data, if either transmission data or emission data, or both data are corrupted with motion, mismatches are likely to occur, leading to the propagation of errors and ultimately resulting in over or under correction.

The level of activity present in the liver may also affect myocardial SPECT images due to respiratory motion. Since the liver is immediately below the diaphragm, during the respiratory cycle, the relative positions of the liver and heart will vary, with part of the liver occupying the position of the inferior wall of the heart at the end of exhalation[53]. Bruyant *et al.* (2004) identified this phenomenon when investigating the effects of attenuation correction using simulated transmission cardiac SPECT imaging corrupted with respiratory motion[53]. Their results showed that the respiratory motion introduced an apparent low tracer uptake in the inferior wall of the myocardium[53]. In addition, they observed that the activity in the inferior wall of the myocardium also varied with the liver's activity, mainly because during motion the liver is raised and part of it occupies the place where the myocardium's inferior wall was[53]. Furthermore, Pitman *et al.* (2005) examined the effects of sub-diaphragmatic activity, diaphragmatic respiratory motion and attenuation on the inferior wall, in ^{99m}Tc myocardial perfusion SPECT[54]. Physical phantom measurements showed that the position and concentration of sub-diaphragmatic activity in relation to the myocardium determine the hot or cold nature and severity of the inferior wall artefact[54].

On the other hand, it has been suggested that, similarly to ECG-gated SPECT, respiratory-gated SPECT might improve the quantification of the radionuclide distribution. Pitman *et al.* (2002) evaluated the effect of diaphragmatic respiratory motion on the inferior wall cold artefact in myocardial SPECT and whether attenuation correction corrected for this artefact[55]. Their experiments on a physical phantom showed that

simulated diaphragmatic respiratory motion contributes to a relative reduction in apparent count density on the inferior and anterior wall, when compared to the lateral wall and septum[55]. Moreover, as the amplitude of respiratory motion increases, the more marked is the artefact, and depending on the respiratory pattern, its symmetry will change[55]. Regarding the attenuation correction process, it corrected the attenuation artefact, but was not able to correct for the diaphragmatic respiratory artefact[55]. This can be explained by the non-attenuation nature of the respiratory artefact. Therefore, Pitman *et al.* (2002) recommended the use of respiratory gate in myocardial SPECT[55].

In order to diminish the inferior wall artefact, Cho *et al.* (1999) proposed a respiratory gated SPECT system based on impedance plethysmography and evaluated it with clinical data from healthy male subjects[56]. They found that respiratory gating yielded improved inferior wall activity[56]. The process of respiratory gating consists in acquiring the SPECT image only during a period of the respiratory cycle in which the extent of motion of the heart and diaphragm is reduced, effectively reducing the amount of blur caused by respiratory motion. However the number of detected counts within each gate or fame is smaller when compared to a full acquisition, leading to an increase in noise. Therefore there is a trade-off between respiratory motion artefact reduction and increased image noise. Segars *et al.* (2002) proved the effectiveness of respiratory gating in SPECT simulations using the 4D NURBS-based cardiac-torso (NCAT) phantom[57–59], and more recently[60], demonstrated that optimization of the gating scheme is needed to further improve SPECT quantification. This optimization is based on the amount of respiratory motion of the heart during each gate, the number of gates performed and the placement of the gates within the respiratory cycle[60].

In addition, one important step in respiratory gating is motion estimation. Different methods are used to track indirectly the motion of the heart and diaphragm. Usually they involve the analysis of signals from pressure or resistor belts wrapped around the patient's chest or abdomen[61], the tracking of infra-red markers attached to the patient[62,63], or the monitoring of airflow using pressure sensors or thermometers. The respiratory gating scheme for the SPECT acquisition is then based on motion estimation.

In summary, respiratory motion compromises cardiac SPECT image quality, affecting lesion detectability, and leading to wrong diagnoses. The extent of image distortion varies from patient to patient and within each patient, resulting in changes for example from stress to rest test of the same patient. Therefore motion prevention and motion estimation are required to correct for motion-corrupted acquired SPECT data, and to obtain quantitatively accurate myocardial SPECT images.

2.4 Simulation and Analysis Tools

A review on selected simulation and analysis tools, which were fundamental for the development of this thesis work, is given in this section.

Simulation of different imaging systems or system configurations allows a better characterization and understanding of the system's operation and limitations, providing a means for the study of specific issues whose results can lead to the improvement of clinical protocols. For the purpose of this thesis, only D-SPECT data modelling and cardiac imaging analysis tools are addressed, namely the NCAT phantom, the D-SPECT *Simulator*, the reconstruction software and the bull's eye plots.

2.4.1 NCAT Phantom

Computerized phantoms have had a huge impact in medical imaging research, improving the evaluation and development of imaging instrumentation, data acquisition techniques, reconstruction processes and image processing[64]. In order to accurately model the anatomy and physiology of the human body, these phantoms aim to combine the realism of patient-based voxelised phantoms with the flexibility of geometry-based phantoms[65].

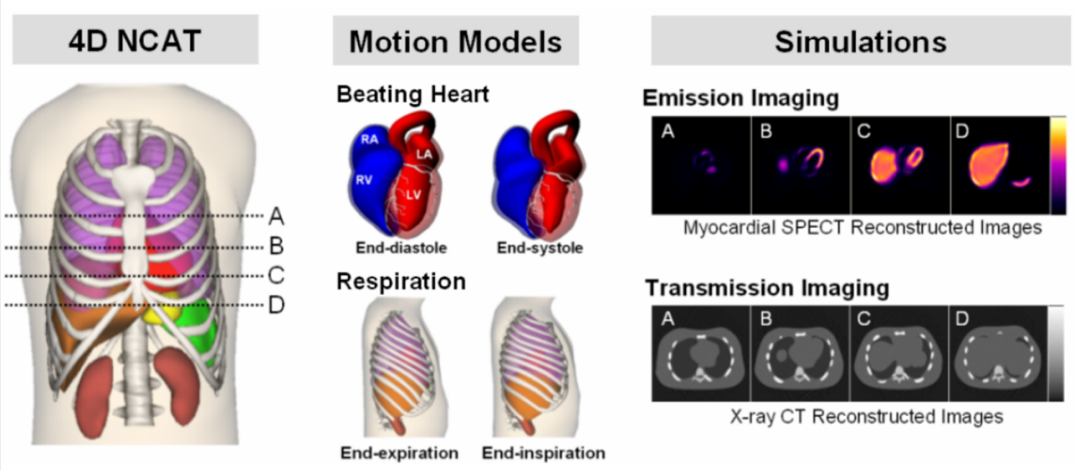

Figure 2.27: 4D-NCAT phantom. On the left, an anterior view of the NCAT phantom is shown. The central panel presents the motion models that can be included in the phantom: beating heart and respiration. On the right, SPECT and CT simulated images are shown for the four slices highlighted in the phantom[66].

The 4D NURBS-based Cardiac-Torso (NCAT) phantom (Fig. 2.27)[66] is a visible human phantom generated by NCAT 2.0. This software simulates emission and transmission data from a human torso. Organ shapes are based on the 3D Visible Human CT dataset, which includes 512 × 512 axial CT scans of the human torso with 1-mm slice intervals and a pixel width of 0.898 mm[65]. The program includes options to introduce

anatomical variations in organs and structures, generate perfusion defects, as well as to model myocardial contraction and respiratory motion.

The main program of the NCAT software is `dncat_bin`, which can only be executed from the command line of a computer giving the following instruction:

```
dncat_bin parameter_file output_name
```

This instruction refers to the three main components in the creation of a phantom. `parameter_file` is the file in which parameters that characterize the phantom to generate are defined, such as the voxel size, motion, variations in anatomy, radionuclide uptake ratios for the activity of the specific organs and photon energy for defining attenuation coefficients. After running the `dncat_bin`, the output will be a series of raw binary phantom files with base-name `output_name` and 32-bit float data format in little endian byte order. In the case of a static phantom, two output files are generated, one with the information about the activity distribution in the torso and whose name ends with `_act`, and another file that includes the attenuation coefficients and whose name ends with `_atn`. In the case of a dynamic phantom, the output will also be activity and attenuation files, but instead of generating only two files, the program will generate $n+n$ files, which correspond to activity and attenuation files of n simulated time frames. In addition, a `_log` file is generated, which contains information about anatomical variations in each simulated time frame, such as lung volume or heart displacement, to name a few.

2.4.2 D-SPECT Simulator

The D-SPECT *Simulator* is a MATLAB (Mathworks, Natick, MA, USA) graphical user interface developed in-house at UCL to simulate and reconstruct projection data obtained by different configurations of SPECT systems. This simulation tool has been fully validated.

The main interface of the *Simulator* is called `Model_Interface` (Fig. A.1 of the Appendix A). It is divided into four main parts, the system configuration, which comprises the camera and source set up, the projection simulation, the reconstruction and the display. As the reconstruction field of the *Simulator* was not used in the work presented in this thesis, no further considerations will be given to this. The other parts of the interface are described in detail in the next paragraphs.

In the `Camera` field, the user can either load an existent camera file by choosing a camera from the list and clicking on the button `Quick Load Camera` or set up a new one by clicking `Set Up Camera`. When this button is pressed, the user can either select a D-SPECT camera, or another type of camera. However, only the interface for the D-SPECT system is operational. So, this sub-interface called `D_SPECT` (Fig. A.2 of the Appendix A)

allows the user to configure a new imaging scan. Basically, using the defined parameters, it calculates the motion pattern of the detectors for data acquisition. The first step to create a new camera is to either choose a collimator from the `Collimator Selection` list, or specify a new parallel-hole collimator by filling in the correspondent fields. Then, by clicking on the `Create and Display Camera` button, an image will be displayed with the position of the detectors. The next step is to load a source of activity, such as a human phantom, by clicking on the `Add Source` button. The displayed image will be updated with the image of the phantom. There are also options for manually defining ROIs and FOVs by clicking on the `Select ROI` and `Select FOV` buttons, respectively. Then the user needs to press `Calculate Scan Pattern` to create a new motion pattern for the detectors. Note that when a ROI is defined in the image, the user must select which algorithm should be used to calculate the new motion pattern. There are three different algorithms, the detector centre approximation, the detector leading edge and the detector trailing edge. The difference between them is in the definition of when to start and stop the region-centric acquisition. Given that each detector rotates during the scan, a leading and a trailing edge of each detector can be defined. In the detector centre approximation, angles of the detectors are calculated taking into account that the region-centric acquisition starts when the centre of the detector reaches the defined ROI, and stops when the centre of the detector leaves the ROI (Fig. 2.28-a). On the other hand, using the detector leading (or trailing) edge algorithm, the angles are calculated taking into account that the region-centric acquisition starts when the leading edge (or trailing edge) of the detector reaches the defined ROI, and stops when the leading edge (or trailing edge) of the detector leaves the ROI (Fig. 2.28-b and Fig. 2.28-c). Two other parameters are important to calculate the scanning pattern: the total number of rotational detector positions and the scan proportion on the ROI. The former refers to the total number of angles per detector during the scan, and the latter corresponds to the fraction of time that the detectors spend scanning the ROI, typically a number between 0 and 1. For example, if it is 0, detectors will scan the whole FOV but not the ROI; if it is 0.5, it means that during half the time of the scan, detectors will be scanning just the ROI, and in the remaining time they will be scanning the region outside the ROI; if it is 1, detectors will only scan the ROI, which is the same as defining a FOV equal to the ROI. Finally, the calculated scan pattern can be viewed as an animation in the `D_SPECT` interface, and the corresponding camera file can be saved by clicking on the `Save and Return Camera` button. After this, the user returns to the main interface to select a source of activity, i.e. a phantom, for the simulation. By pressing the `Quick Load Source` button, the selected source of activity from the provided list is loaded and displayed on the left side of the interface. This plot includes a visualization of different views of the phantom: axial, coronal and sagittal. There

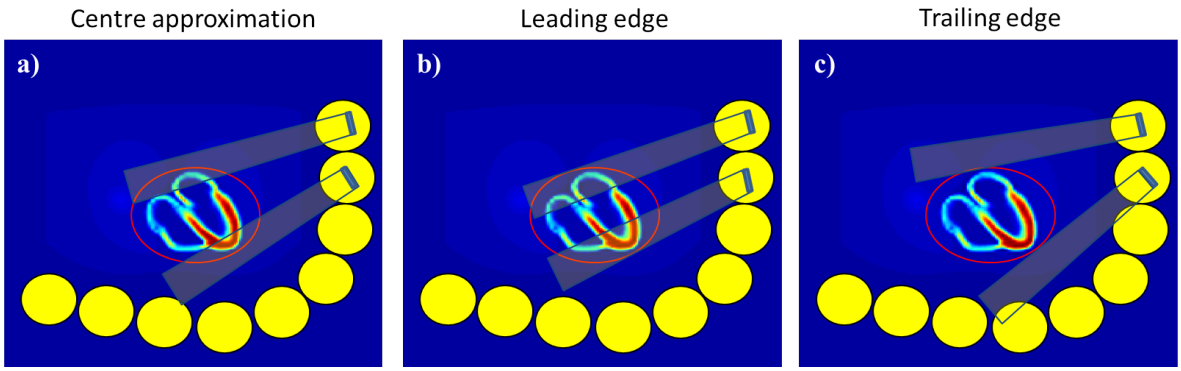

Figure 2.28: Schematics of the algorithm to calculate the scan pattern. In the figure, **a)** corresponds to the centre approximation, **b)** corresponds to the leading edge algorithm, and **c)** to the trailing edge algorithm.

is also the possibility to set up a new source by pressing the `Set Up Source` button. A sub-interface called `SOURCE_SET_UP` (Fig. A.3 of the Appendix A) will open with options to load an existing source of activity or just a source or attenuation matrix, and change its centre position and voxel size. These changes can be saved by clicking on the `Save and Return Source` button.

Regarding the projection data modelling, the user has to define some parameters in the `Projections` field of the main interface, such as: group angles and the models for noise, resolution and attenuation. Regarding a Poisson-distributed noise modelling, projections may be modelled taking into account the scan time in seconds and the activity of the administered radiopharmaceutical in MBq, or the total number of detected photon counts. If no noise model is selected, the user will get a relative activity image with smooth projections, i.e. not contaminated with noise. To reduce the time of the simulation, the user may enable the group angles routine, reducing the number of angular positions of the detectors. Concerning the depth-dependent resolution, this parameter is modelled using a blurring kernel applied slice by slice and a summing algorithm based on the work of Zeng *et al.* (1998). This model does not include a term for the intrinsic resolution of the detector itself, taking the value of the detector pixel size as the intrinsic resolution. Additionally, the model is only applicable for parallel-hole collimators. Moreover, the attenuation model is based on studies of Bai *et al.* (1998) and it requires an attenuation map of the source of activity expressed in per millimetres, with linear attenuation coefficients for 140-keV photons emitted by ^{99m}Tc. However, this model does not account for scatter or for temporal changes in the source of activity during the acquisition. As a result, only projections acquired from static phantoms can be simulated. Furthermore, all the detectors rotate in the same direction, as opposed to what happens in the real system, in which even-numbered detectors rotate clockwise and odd-numbered detectors rotate counter clockwise. Note that this last issue is not a

problem because simulations do not take into account time, so the order of the acquired projection data does not matter.

After setting up all these parameters, projections are calculated pressing the `Model Projections` button. The output of this process can be saved in a simple `.mat` structure by pressing `SAVE(handles)`. However, in order to use this information in the D-SPECT reconstruction system, simulated data have to be saved in a compatible format - `.csv` files. This is accomplished by pressing the button `SAVE(D-SPECT)`.

At last, the display section of the main interface enables the visualization of the camera geometry, the source of activity, the projection data including the correspondent sinograms, and the reconstructed data.

2.4.3 Reconstruction Software

The reconstruction software presented in this section was developed by Spectrum Dynamics, Caesarea, Israel. The main interface (Fig. B.1 of Appendix B) includes the parameters of the reconstruction process, which can be modified, to a certain extent, by the user.

Given the projection data located in `Study Path`, the program will run the OSEM-based reconstruction algorithm to reconstruct the acquired images, which will be saved in the path defined by `Result Path`. Reconstruction parameters that can be changed are the number of pre-model iterations of the OSEM algorithm, as well as the number of post-model iterations. If the number of post-model iterations is zero, this means that the reconstruction is done without a fit to the model of the left ventricle. Regarding the inter-iteration and post filters, the user may select if they are applied or not. If applied, the software allows the adjustment of parameters such as the smoothing frequency and factor. Gated reconstruction and left ventricle parameters are out of the scope of this project, therefore they will not be analysed. All these parameters can also be altered or defined in the file `reconstructionParameters.ini`. Once all the parameters are adjusted, reconstruction will begin after pressing the button `Next`. On the other hand, this program can also be called from the command prompt using the following instruction:

```
pathTo_reconstruction.exe CompareVersion pathTo_input_projections_folder
pathTo_output_results_folder pathTo_reconstructionParameters.ini
```

Note that this instruction specifies the paths for the reconstruction executable - `reconstruction.exe` -, the input and output folders, and for the parameters file - `reconstructionParameters.ini`.

When all pre-model iterations are completed, a sub-interface will open (Fig. B.2 of the Appendix B). This interface displays the reconstructed left ventricle in the VLA,

HLA and SA views, and also the ROI that was used for the reconstruction process. An automatic reorientation of the left ventricle is done, but the user may change it using the AB-segment lines. Also, the ROI in the sagittal and transaxial views may be enlarged or reduced to better conform to the shape of the left ventricle. Then, by pressing the `Next` button, the reconstruction will proceed to the post-model iterations, or save the reconstructed data if the user did not previously select post-model iterations. Resultant reconstructed images at each iteration are returned in a `.est` format.

2.4.4 Bull's Eye Plots

Bull's eye plots are 2D displays of a 3D distribution of the radiotracer activity in the left ventricle. These plots offer a standard method for viewing and compare images of the left ventricle from different patients, or from the same patient but for images acquired at different times or in rest/stress studies[67].

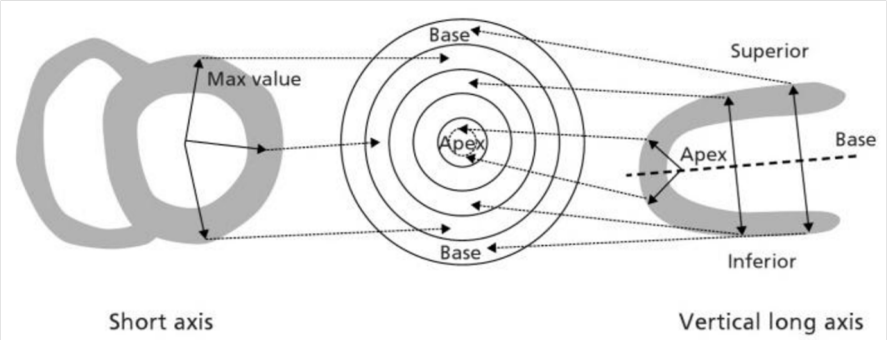

Figure 2.29: Relationship between bull's eye and myocardial regions. Arrows indicate the regions of the myocardium that were sampled to generate the bull's eye. Image adapted[1].

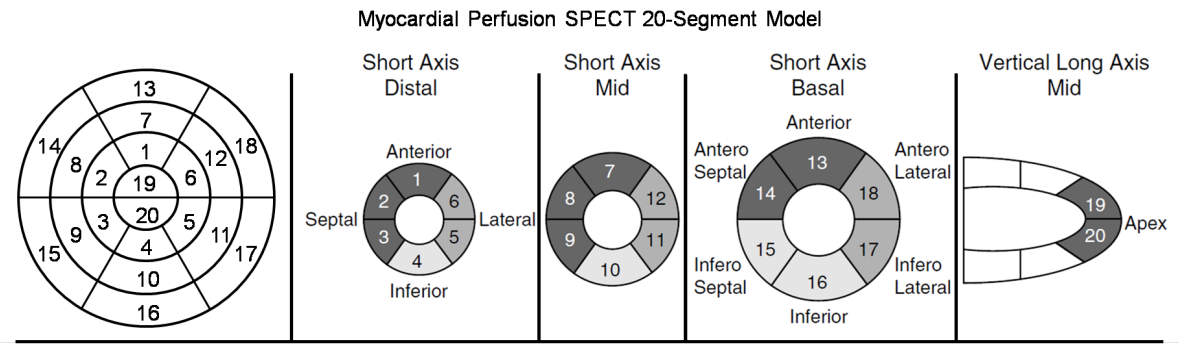

Figure 2.30: 20-segment model of a bull's eye. The image shows how segments are numbered, and the corresponding regions of the ventricle. Image adapted[68].

In order to generate a bull's eye plot, the left ventricle has to be fitted to a sort of cylinder with one end corresponding to a half-sphere. Therefore data from the basal and mid-ventricular walls of the left ventricle are sampled with cylindrical coordinates, and data from the apical region of the ventricle are sampled with spherical coordinates[67],

generating a cylindrical colour-coded image. This sort of cylinder is then divided into four short-axis slices, i.e. perpendicular to the height of the cylinder, each corresponding to a circular ring of the bull's eye plot. The innermost ring corresponds to the apex of the left ventricle and the outermost ring corresponds to the basal region of the ventricle[69](Fig. 2.29). In the case of the 20-segment model, each ring of the bull's eye plot is then divided into six segments, except for the innermost ring which is only divided into two segments[68] (Fig. 2.30). Furthermore, the superior and inferior parts of the bull's eye correspond to the anterior and inferior region of the ventricle, respectively, and the left and right parts of the bull's eye correspond to the septal and lateral regions of the ventricle, respectively. Finally, a myocardial perfusion number is assigned to each segment. This value is calculated as the mean activity value for that region, normalized to the maximum value of activity, providing good support for a quantitative analysis[1]. For a ventricle with the same thickness within the muscle, a uniform bull's eye is expected. Artefacts or defects will appear in the form of hot or cold spots.

In spite of being useful to detect and characterize myocardial perfusion defects, bull's eye maps distort the relative size and shape of the various regions of the myocardium, as they fit every heart to the cylindrical-spherical model, and they do not take into account the motion of the heart during the image acquisition[70,71].

Chapter 3

Developed Software

The D-SPECT *Simulator* is a software tool, developed in-house, that allows the simulation of D-SPECT projection data (Section 2.4.2). However this simulation tool is not able to simulate scans that account for temporal changes. For example, it does not account for activity changes during the time of the scan, neither for position changes due to respiratory or patient motion. In addition, it does not simulate scatter, so the fact that all detectors rotate in the same direction during the simulated acquisition is not a problem. However, in fact, that is not what happens in the real camera, in which even-numbered detectors rotate clockwise and odd-numbered detectors rotate counter clockwise to prevent shielding effects. Moreover, the *Simulator* is an interface-based software, consequently all the acquisition parameters need to be defined in the interface before each simulation starts. As a result, it is more likely that errors are included in the simulation, if every time a simulation is performed, parameters need to be settled in the interface. So it would be advantageous to have the possibility to set the parameters only once for several simulations. Therefore, in order to study the acquisition geometry of the D-SPECT and the effects of respiratory motion, some modifications to the *Simulator* needed to be performed.

Additionally, as previously described (Section 2.2.2), in cardiac SPECT imaging the sectional views of the heart are displayed in a different orientation than the usual for tomographic images. Instead of using the human body planes (Fig. 3.1-a), which are the coronal plane, sagittal plane and transaxial plane, cardiac SPECT images are displayed in the heart's own axes (Fig. 3.1-b): Horizontal Long Axis (HLA), Vertical Long Axis (VLA) and Short Axis (SA). Having a standard way of displaying these images, the comparison between images from different studies and patients is easier.

Furthermore, for the purpose of image analysis and interpretation, bull's eye plots are usually generated and a quantitative assessment is performed. In a bull's eye plot, the myocardium is displayed in a circular plot in which each segment corresponds to a specific region of the myocardium, facilitating the detection of perfusion abnormalities,

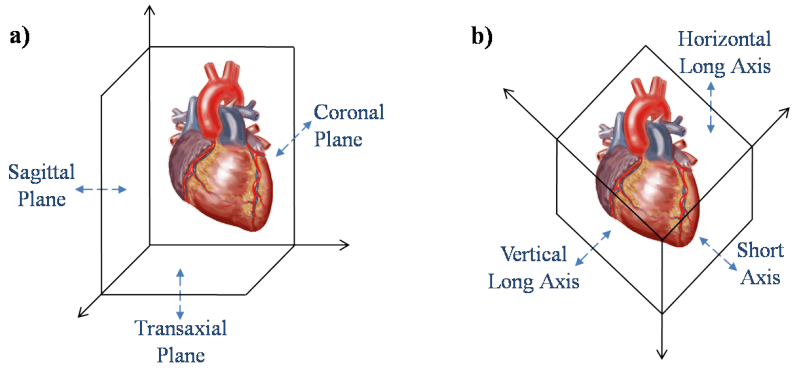

Figure 3.1: Representation of different axes in relation to the heart. On the left hand side, **a**) shows the human body axes: coronal, sagittal and transaxial. On the right hand side, **b**) shows the myocardium's axes: HLA, VLA and SA.

as described in Section 2.4.4.

Commercially available re-orientation and analysis software have limited usage. Some pre-defined parameters are not always adequate for a certain simulation, and their modification may be difficult or restricted. Also, there is no access to re-oriented data sets, just the image itself, and the analysis is restricted to implemented tools. Therefore the development of open-analysis software is an important step to know exactly which processing is being performed, and to have the autonomy to implement different types of metrics.

In this chapter, modifications to the D-SPECT *Simulator* are described, a re-orientation algorithm is presented, and a methodology for the selection and analysis of different regions of the myocardium is shown. All these tools were developed using MATLAB as the computing language.

3.1 D-SPECT Simulator Modifications

The first adjustment to the *Simulator* was to change it to script-base, instead of running an interface to obtain projection data.

The script receives as an input all the data that would be otherwise defined by the user directly in the interface, and estimates projection data with the MATLAB functions previously developed for the interface. The difference between the script and the interface is that one of the input variables contains several sources of activity, each one corresponding to a different simulation. As a result, when the script is executed instead of obtaining projection data from one simulation, several projection data are obtained. In addition, the acquisition parameters need only to be defined once, reducing possible sources of error.

The command line to run the script is the following:

```
task(binFile, cam2open, saveFoldName, attModel, nphotons);
```

`task` is the name of the developed function. It receives as an input the variables `binFile`, `cam2open`, `saveFoldName`, `attModel` and `nphotons`. `binFile` is a *structure* array of the type `binFile.N`, where `N`$= i, ii, ..., n$. It corresponds to `N` sources of activity. For each source, seven fields need to be defined in the *structure*: `binFile.N.size` is the matrix length on each dimension, `binFile.N.path` is a *string* with the general path for the NCAT phantom folder, `binFile.N.savepath` is a *string* with the general path for the created `.mat` file at the end of the simulation, `binFile.N.data` is a *string* with the name of the phantom's activity file, `binFile.N.att` is a *string* with the name of the phantom's attenuation file, `binFile.N.Cpos` is the position of the source's centre, and `binFile.N.sourceVox` is the voxel size on each dimension. Regarding the remaining input variables, `cam2open` is a *string* with the name of the camera, and `saveFoldName` is a *string* with the name of the folder for the resulting projection data. `attModel` is a binary array, where 1 and 0 refer to the inclusion or exclusion of attenuation modelling, respectively, and `nphotons` is a *string* with the number of photons to simulate. After running the script, nine `.csv` files are generated per simulation, that is, per source of activity, corresponding to estimated projection data from each detector of the D-SPECT. In addition, the sources of activity created during the simulation are also saved as a `.mat` file (standard MATLAB file format).

The second modification regards time-dependent projections. As previously mentioned, the *Simulator* does not account for time changes; consequently, to study the effects of respiratory motion during the acquisition, adjustments had to be made to the program.

In this case, for each time point, the source of activity is different, because the position of the heart in relation to detectors changes during breathing. This is simulated by the NCAT program, which creates a series of phantoms to give as an input to the *Simulator*. There is also the problem that, at each time point, each detector is acquiring from different parts of the heart, due to the D-SPECT scanning geometry. Hence the timings of the acquisition and the respiratory motion must be sorted out. In addition, in this case the direction in which each detector rotates during the simulation is important.

As a result, the first step was to modify the camera *structure* that the program uses, such that even-numbered detectors rotate clockwise, and odd-numbered detectors rotate counter clockwise.

Then a script was created to estimate all projections for a certain respiratory pattern. In other words, for each time point of the respiratory cycle, this script estimates projection data according to a previous function developed for the D-SPECT *Simulator*. The command line to run the script is the following:

```
create_allPROJ4oneCAM(study_name, noise_model, att_model, res_model, ...
                  ...angle_group, angle, cam2open);
```

The input variables are `study_name`, which is a *string* with the name of the folder for the simulation results, `angle`, which is a *string* with the value to group each angular position of the detector - usually one degree -, and `cam2open` is a *string* with the name of the camera to use in the simulation. `noise_model`, `att_model`, and `res_model` are binary variables that indicate whether noise, attenuation and resolution are modelled (1), or not (0). `angle_group` is also a binary variable that indicates whether projections are calculated with grouped angles (1) or not (0); for example, they can be calculated at each degree, instead of each tenth of a degree. In the end, thirty-two `.mat` files are generated, which corresponds to each time point of the respiratory cycle, that is, each phantom simulated by the NCAT program.

Another function called `scan_pattern` was implemented to sort and match projections according to the scan and respiratory pattern. The command line to execute the function is:

```
scan_pattern(study_name, allDataFolder, noise_model, att_model,   ...
          ...res_model, angle_group, angle, cam2open, start_time, ...
          ...fs, scan_time, nb_frames)
```

It receives as an input variables already described, such as `study_name`, `noise_model`, `att_model`, `res_model`, `angle_group`, `angle`, and `cam2open`. Other input variables are `allDataFolder`, which is a *string* with the name of the folder of projection data, `start_time` is the duration of the respiratory cycle in which the acquisition starts, in seconds, `fs` is the detector's sampling frequency in seconds, `scan_time` is the duration of the simulated scan in minutes, and `nb_frames` is the angular sampling of the simulated scan pattern. In addition, when the script is running, the user is asked to introduce a number for the variable `pointi`, which is the point of the respiratory cycle in which the simulated acquisition starts. This variable takes an integer number from 1 to 32. For example, if `pointi` is 1, the acquisition starts when the phantom is in the position of fully exhalation, if `pointi` is 8, the acquisition starts when the phantom is in the position of mid-inhalation, if `pointi` is 16, the acquisition starts when the phantom is in the position of full inhalation, and so on. Additionally, the script asks for a number for the variable `nphantoms`. This variable refers to the number of phantoms - sources of activity - that occur during each angular position of one detector. Let 0.48 seconds be the sampling time of detectors, and that the NCAT program simulates a new phantom each 0.16 seconds, then `nphantoms` is 3 ($3 \times 0.16 = 0.48$). So the script takes the values of `nphantoms` and `nphantoms` to sort and match projection data and, because projections are the integral of the photon counts over time, a new simulated projection is estimated as the average of `nphantoms` projections (Fig. 3.2). Note that there are only 32 projections corresponding to the 32 simulated phantoms, so projections obtained

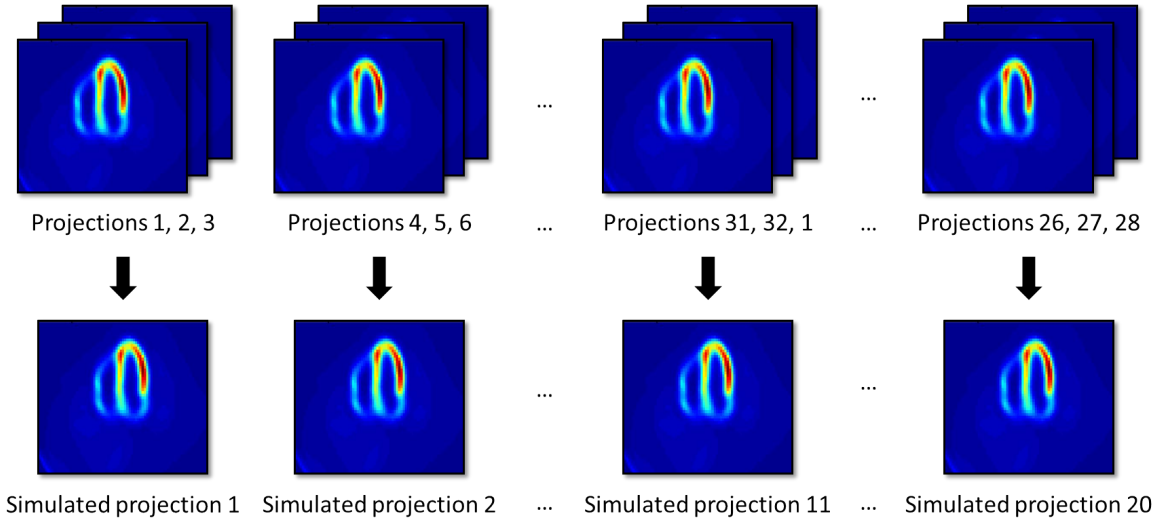

Figure 3.2: Procedure to obtain simulated projections with respiratory motion. From a set of projections, new simulated projections are estimated for each angle of acquisition. This example shows a schematic representation of a simulation acquired with an angular sampling of 20 angles per detector, 0.48 seconds per angle, and 9.6 seconds of scanning time. Each time frame of one respiratory cycle is projected. The 32 projections are then divided in groups of three consecutive projections. These projections are then averaged to obtain one simulated projection. Note that one respiratory cycle last for 5 seconds, therefore time frames have to be repeated to reach the total scanning time.

for one respiratory cycle are successively repeated until the end of the scan to estimate the new projections. When this process is over, which occurs when the `scan_time` is reached, a set of new simulated projections are created. This constitutes one simulation with a defined scan and respiratory pattern.

3.2 Orientation Tool

The aim of this re-orientation tool is to apply a transformation to the reconstructed D-SPECT image, in order to view it in the heart's own axes instead of in the human body's axes. The main steps of the process of re-orientation of the myocardium are shown in Fig. 3.3.

After the reconstruction, D-SPECT images are returned as `.est` files (D-SPECT file format); so the first step of the code is to open the 3D image, provided the path for the file, and then save it as a `.mat` variable. For that, the MATLAB functions `fopen` and `fread` are used to open the `.est` file and to read the detected counts and the size of the image matrix, respectively. Since the `fread` function returns a vector, it is then reshaped into a 3D matrix with the corrected dimensions, using the extracted information about the image size.

The following step consists in saving stacks of 2D matrices correspondent to three orthogonal views, such as the coronal, sagittal and transaxial view, in three different variables. Then a rotation of 36°is applied to the matrix corresponding to the transaxial

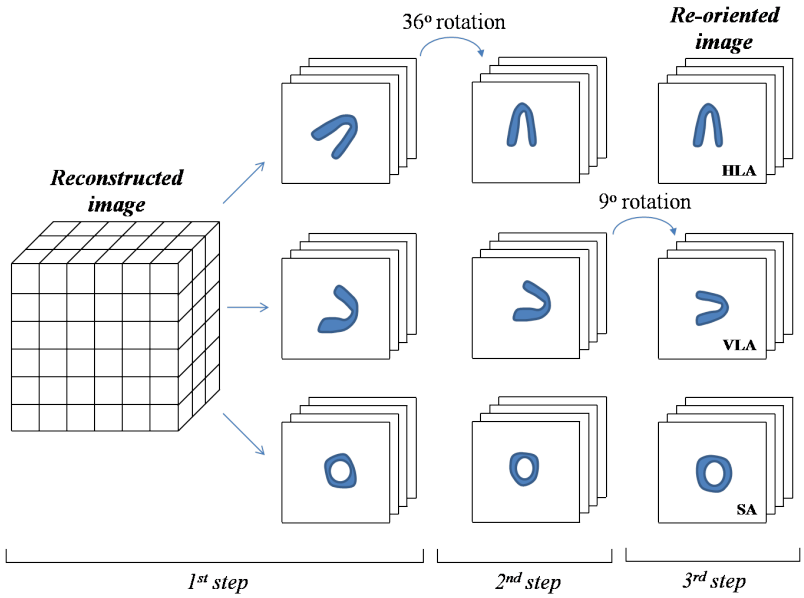

Figure 3.3: Diagram of the re-orientation process. The first step corresponds to view the reconstructed image on the three human body axes. The second step corresponds to the rotation of the image having the image more similar to the HLA view as the reference image, and the third step is another rotation having the image more similar to the VLA view as the reference image. Each step (column) shows the stack of 2D images on three orthogonal views. The last column corresponds to the three standard views of the myocardium: HLA, VLA, and SA. Note that the images of the myocardium are only a representation, and are not to scale.

view, which is the most similar to the HLA view. The rotation is performed using the MATLAB function `imrotate`, with a bicubic interpolation, being the output image a cropped image. The rotated image is cropped to have the same size as the initial input image. The selection of the rotation angle was based on visual assessment of the resultant myocardium's image: the HLA view should show the myocardium with the apex in a superior position in relation to the base, and the septal and lateral walls should be in a vertical position. Therefore, it shows the myocardium in a view similar to the transaxial plane, as if we were looking at the patient from the top.

After the 36°-rotation, the apex of the myocardium is coincident with the long axis of the heart, instead of being rotated to the left, which is the anatomical position. However, the three orthogonal views do not correspond to the heart's own axes yet, as shown in Fig. 3.4-b. This misalignment is due to the anatomical position of the heart, in which the myocardium's apex is tilted in the anterior direction. Therefore a new rotation needs to be performed to have the images of the heart on its own axes.

A second rotation is then executed with the same code and parameters described for the first rotation, but using an angle of rotation of 9°and having the image more similar to the VLA view as the reference image. Again the angle was chosen by visual assessment of the resultant VLA view of the myocardium. In this view, the apex of the myocardium should be on the right hand side and the base on the opposite side,

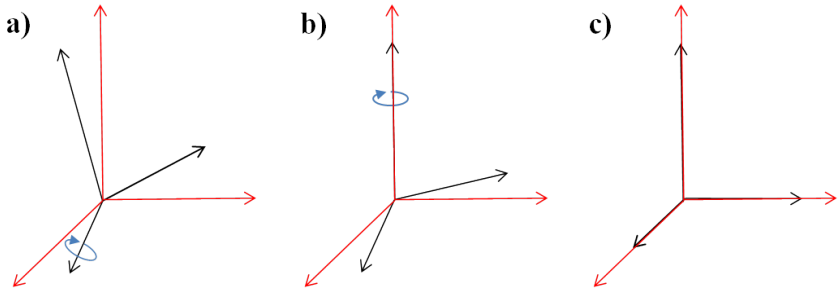

Figure 3.4: Position of the axes at three different stages of the orientation code. The red axes correspond to the aimed axes in order to show the images on the heart's own axes, and the black axes correspond to the axes of the image. After the first rotation (a), the heart is not yet aligned (b). Therefore a second rotation, having the plane highlighted by grey as a reference, needs to be performed to achieve (c).

and the anterior and inferior walls should be positioned horizontally. Hence this view represents the myocardium as if it was seen approximately from a vertical left-hand-side plane of the patient.

By re-positioning the heart according to the VLA and HLA views of the myocardium, the remaining orthogonal view, SA, is forcedly aligned with the heart's axes. In this view, the myocardium has a shape of a ring, in which its superior and inferior parts correspond to the anterior and inferior walls of the myocardium, respectively, and the left and right hand sides correspond to the septal and lateral walls, respectively. Thus these images of the myocardium can be seen as cuts of the heart perpendicular to its long axis, which is along the septum, from an anterior point of view. Hence after all this process, the three displayed views of the myocardium correspond to the VLA, HLA and SA views. However, it is important to note that these rotation angles (36°and 9°) are appropriate only for the current phantom.

Finally this orientation tool displays the re-oriented images in three different windows, each one showing twenty slices of the myocardium on each view, or in only one window,

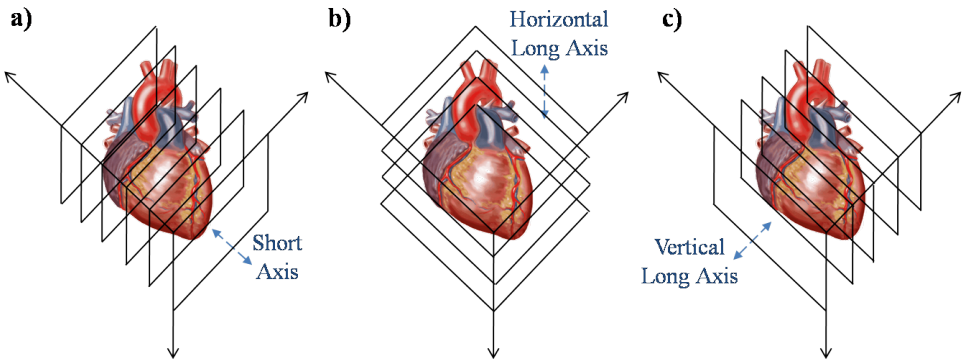

Figure 3.5: Schematics of the slices for each view of the heart. Slices are represented for the three views of the heart: SA (a), HLA (b) and VLA (c).

with three iterative displays of the twenty slices, corresponding to the three views, VLA, HLA and SA. Regarding the order the slices are displayed on each view, in the case of the SA view, slices are shown from apex to base (Fig. 3.5-a), in the HLA view, slices are shown from posterior to anterior wall (Fig. 3.5-b), and in the VLA view, slices are shown from the septal to lateral wall (Fig. 3.5-c). In order to accomplish these specifications, the analysis of the body and liver contour was used as a guideline. It is important to note that the oriented images are not shown with the same dimensions on purpose, otherwise the heart would be deformed and not to scale, since the reconstructed 3D image does not have cubic dimensions.

3.3 Region-analysis Tool

The region-analysis tool consists in a program that applies different metrics to certain regions of the heart.

First it re-orients the heart using the orientation function described in Section 3.2. Then an intensity-based mask is applied to select twelve regions of the myocardium as presented in Fig. 3.6. In order to do so, a threshold of half of the maximum activity is applied to the image, then the MATLAB function `bwconncomp` is used to select only the myocardium from the resulting binary image. Because this function computes connected components from an image, the myocardium will be the largest detected component.

Regarding the region selection, the boundaries of each region were manually selected based on visual assessment of a reference myocardium, which was not distorted and

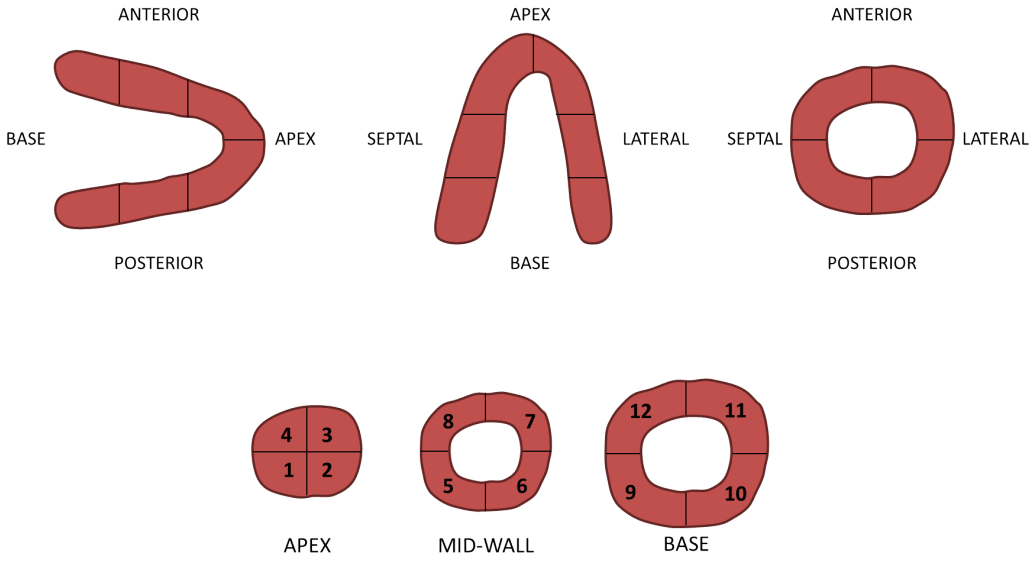

Figure 3.6: Schematics of the myocardial regions analysed by the region-analysis tool. The myocardium selected by means of an intensity-based mask is divided in 12 regions. On the top, the myocardium is displayed in the three standard views, VLA, HLA, and SA, from left to right, respectively. On the bottom, the myocardium is displayed similarly to bull's eye plots.

did not contain any artefacts. So these limits are applied to the image, and a label is assigned to each region. Tab. 3.1 indicates which label is assigned to which region of the myocardium.

The final step of the program is to apply different metrics to each selected region. At the moment, it calculates the mean activity of the voxels in a certain region, and its standard deviation, but the function can be easily updated to apply other measures.

In conclusion, this program analyses the myocardium in a similar way that bull's eye plots do. The advantage is that each analysed region is rigid, instead of being dependent of the analysed heart. As a result, it facilitates the comparison between regions of different simulated hearts, because they are selected in the same way.

Table 3.1: Correspondence between ventricular location and region-analysis label.

Location	Ventricular wall	Region number
Postero-septal	Apical	1
Postero-lateral	Apical	2
Antero-lateral	Apical	3
Antero-septal	Apical	4
Postero-septal	Mid-ventricular	5
Postero-lateral	Mid-ventricular	6
Antero-lateral	Mid-ventricular	7
Antero-septal	Mid-ventricular	8
Postero-septal	Basal	9
Postero-lateral	Basal	10
Antero-lateral	Basal	11
Antero-septal	Basal	12

Chapter 4

Geometry Considerations of the D-SPECT System

4.1 Motivation and Objectives

The D-SPECT system is a novel SPECT camera designed specifically for cardiac imaging. In addition, it has an unconventional scanning geometry, and detector design when compared to a standard SPECT system: it has nine detectors, and each one rotates independently about their own axis, allowing for the selection of different scanning patterns, such as the open sweep (Fig. 4.1-a) or a region-only acquisition (Fig. 4.1-b). The open sweep is a full scan of the whole FOV, whereas the region-only acquisition refers to a scan that is focused on a previously selected ROI. The clinical scan (Fig. 4.1-c) is, however, a combination of both the open sweep and the region-only acquisition. Detectors will scan the whole FOV, but they will spend more time scanning the selected ROI. In other words, there is a non-uniform sampling of the FOV, because the angular sampling is more frequent in the ROI and sparser in the remaining FOV. Hence, there may be some problems or unknown effects in the reconstructed images, in certain clinical situations, due to this novel acquisition geometry.

Furthermore, one important aspect in medical imaging is the positioning of the patient. The heart, which is the object being scanned in this case, should be positioned as close as possible to detectors, and its distance in regards to detectors should be maintained approximately constant during the scan. However this distance will change for scans of different patients, because patients differ anatomically from each other. For example, the heart of patients with bigger or fatter bodies will be placed further from the detectors in comparison with thinner patients. Additionally, there may be some intra-subject variability in the positioning of the patient for different scans.

If the distance between the heart and detectors is changed, another important issue will be attenuation. Given the different sizes and shapes of patients, greater attenuation

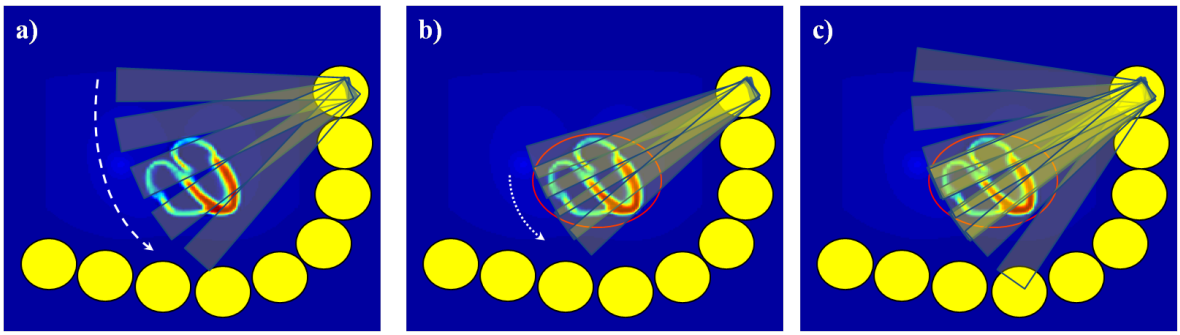

Figure 4.1: Schematic representation of the D-SPECT scanning patterns. Note that only the operation of one detector is shown. a) corresponds to the open sweep scan, b) corresponds to the region-only acquisition, and c) corresponds to the clinical scan (region-centric scan).

effects are expected for larger patients, where photons need to travel a higher distance to get to detectors, thus having more probability of being attenuated. In theory, this problem could be tackled applying attenuation correction algorithms to acquired images. However, it is not possible to acquire transmission and emission scans simultaneously with the D-SPECT system, as occurs with SPECT/CT systems, for example. Hence a separate system such as the CT scan is needed to obtain attenuation information for the same FOV, which can then be used to correct for attenuation after co-registration with the acquired SPECT image. As a result, artefacts can be introduced in the image due to mismatches between attenuation maps and acquired images.

All these issues combined with the novel acquisition geometry may pose some problems when trying to reconstruct the acquired data. Ultimately they can lead to artefacts in the reconstructed images, deteriorating the quality of those images, and the resulting diagnosis. Therefore, the aim of this study is to evaluate the D-SPECT system, regarding the investigation of geometry parameters that can affect D-SPECT reconstructed images, such as the position of the heart in the FOV, and the lack of attenuation correction. These issues have been the focus of several research works in the context of standard SPECT systems, however they have not yet been addressed for the D-SPECT system.

4.2 Methods

The methodology used in the investigation of D-SPECT's acquisition geometry, and the effects of attenuation in the final reconstructed images, is summarised in Fig. 4.2. First, a phantom of the human torso is created using the NCAT software. Then the phantom is given as input to the D-SPECT *Simulator* to estimate projection data. Different phantom positions are simulated, as well as the inclusion and exclusion of attenuation. Projection data are then reconstructed with the clinical reconstruction process, which is based on the OSEM algorithm, and co-registered against a template

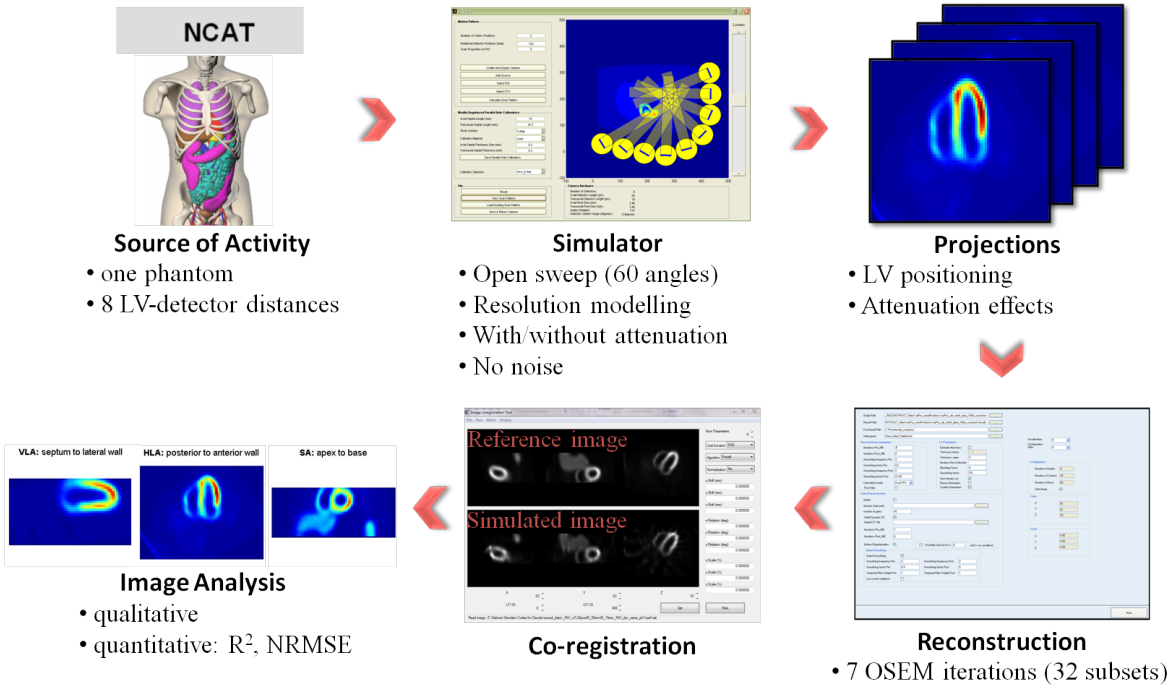

Figure 4.2: Methodology of the first study. This diagram represents the steps performed to investigate the effects of acquisition geometry and attenuation in the reconstructed D-SPECT images.

cardiac image in order to obtain the simulated image. The template image was defined as the myocardial image simulated in the closest position to detectors, and without attenuation modelling, because it should be the simulated image with less artefacts. Finally, simulated images are analysed qualitatively and quantitatively.

In the following sections, each step of the methodology is described in detail.

4.2.1 Generating the Phantoms

In this experiment, the torso of a human phantom was used as the source of activity. Activity and attenuation maps were generated using the NCAT program, which was set up to create a static phantom.

No motion was simulated, including respiratory motion and cardiac contraction, in order to exclude potential sources of image degradation, and to evaluate only the effects of position and attenuation in the reconstructed images.

The resulting files were then converted to MATLAB *structures*, so that they could be used in the D-SPECT *Simulator* as the source of activity of the simulation.

4.2.2 Performing the Simulation

All simulations were performed using the scripts referred in Section 3.1. Camera options were defined for an open sweep scan, with 120 angles per detector. As a result, detectors will scan the whole FOV with 60 angular positions, then the gantry rotates 9°, and the scan is repeated. D-SPECT default collimation options were selected, as well as

the grouping angles property, to accelerate the estimation of projection data. Noise was not modelled, but resolution was. Regarding the attenuation modelling, it depended on the simulation. All these parameters were saved in a MATLAB structure, and given as input to the script, so that projection data could be obtained consecutively for all simulations.

In order to study the effects of the position of the heart in relation to detectors, eight positions of the heart in the FOV were simulated. The first simulated position was the one in which the heart was as close to detectors as physically possible. Other positions were simulated consecutively moving further away the whole phantom along a line dividing the FOV in two similar regions. The last simulation was the extreme case in which the heart is almost outside the FOV. For each position, the distance between the left ventricle (LV) and detectors was calculated as the Euclidean distance between a reference point in the phantom's image and the centre of the fifth detector (Fig. 4.3), which is the closest detector. For future reference, this distance will be called LV-detector distance. The simulated distances were 148, 172, 198, 228, 250, 274, 299 and 323 mm.

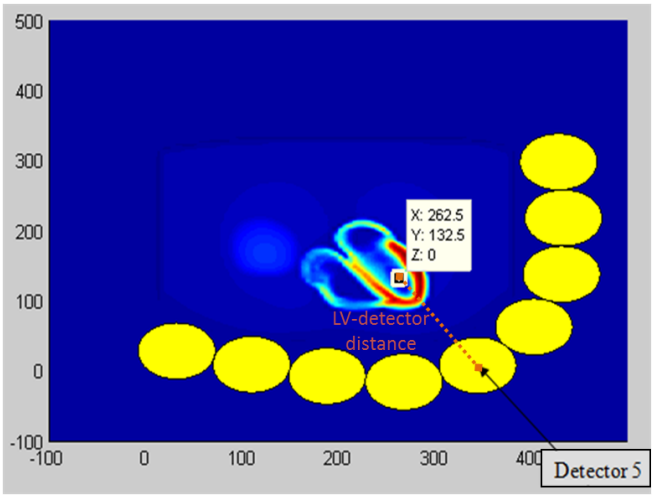

Figure 4.3: LV-detector distance. Schematics of the phantom's reference point used to compute the LV-detector distance, which is displayed in a pink dashed line.

Regarding the effects of attenuation in the reconstructed images, the previously described simulations were repeated, but including attenuation modelling in the simulation of projection data. Therefore, for each LV-detector distance, two myocardial images were obtained, one with attenuation modelling and another one without. Note that when attenuation is not included in the simulation process, the reconstructed image can be interpreted as an attenuation corrected image. That is, the resultant image is an ideally corrected image, because there are no attenuation effects in the reconstructed image. In comparison with an actual attenuation corrected image, the results would not be the same, because the attenuation correction algorithm would not eliminate all

attenuation effects - there is always an error in the reconstructed image. But from this point of view, comparing both simulations may be useful to infer whether attenuation correction is needed for D-SPECT images.

In conclusion, a total of 16 simulations were performed to obtain 8 projection images with attenuation modelling, and 8 projection images without attenuation modelling. Each simulation provided a 4D matrix with dimensions [16 × 64 × 120 × 9], corresponding to the size of each detector (16 by 64), the angular sampling (120) and the number of detectors (9), which was then saved into 9 `.csv` files.

4.2.3 Image Reconstruction

Projection data were reconstructed using the reconstruction software provided by Spectrum Dynamics, Caesarea, Israel. The parameters of the reconstruction process were defined in the `reconstructionParameters.ini` file: 7 OSEM iterations and no post-reconstruction iterations or filtering.

After running the software, each reconstructed image is automatically displayed in the user interface. Each reconstructed image was then manually re-oriented to be in the heart's own axis, and saved in a `.est` file.

Finally all reconstructed images were co-registered with a template image, using an IDL-based co-registration software. In the interface, parameters of the registration were set to a rigid registration with 6 degrees of freedom, and a Powell cost function. The template image for the co-registration was defined as the myocardial image simulated without attenuation modelling, in the closest position to the detectors, which is expected to be the simulated image with less artefacts.

4.2.4 Image Evaluation

In order to evaluate the effects of heart positioning in the FOV, and the effects of attenuation, a qualitative analysis of the reconstructed images of the heart was performed. These myocardial images were visualised and analysed using the QPS software (Cedars-Sinai Medical Centre, Los Angeles, CA, USA).

Using the same software, 20-segment bull's eye plots (Fig. 4.4) were obtained for each simulation. Therefore a value ranging from 0 to 100 of relative activity was assigned to each segment of the bull's eye plot.

In order to compare the relative activity of one segment in relation to other segments of the bull's eye plot, or in relation to the same segment, but from a different simulation, the values of relative activity were plotted as a function of the segment number for all simulations.

In addition, the coefficient of variation (COV), defined as the ratio of the standard deviation to the mean, was calculated and plotted as a function of LV-detector distance

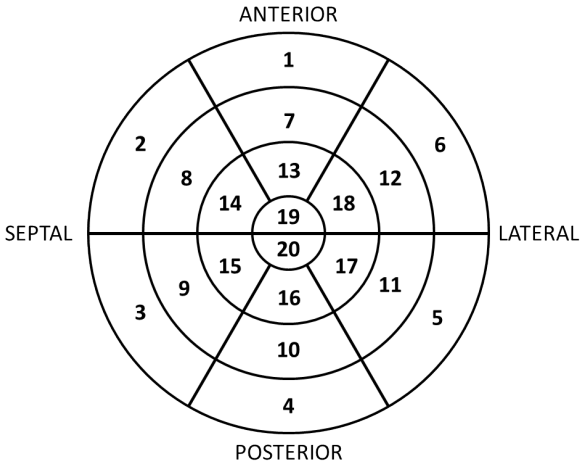

Figure 4.4: 20-segment bull's eye plot. Each segment corresponds to a specific region of the myocardium. The outer ring corresponds the basal wall and the inner ring to the apex.

for both simulations, with and without attenuation modelling.

Moreover box plots of the bull's eye segments' distribution were computed for each simulated LV-detector distance. The smallest and largest observations, represented by the whiskers of the box plot, were set to the minimum and maximum values of the segments, respectively, so that no outliers were considered. These box plots were then placed in two graphs as a function of LV-detector distance, one for simulations with attenuation, and another for simulations without attenuation modelling.

4.3 Results and Discussion

Fig. 4.5 shows the reconstructed D-SPECT images of the myocardium for all the simulated positions of the phantom in the FOV. In this case, attenuation modelling is included in the simulation. For the simulated LV-detector distances of 148 mm, 172 mm, 198 mm, and 228 mm, the reconstructed image of the myocardium presents a reasonable distribution of the radiotracer activity, with a slight decrease in the uptake in the region of the lateral wall. As the LV-detector distance further increases, the radiotracer uptake in the septal, lateral and basal regions decreases, resulting in a non-uniform distribution of the activity within the myocardium. One common characteristic of all these reconstructed images is that, in the region of the apex, there is a lack of activity. This is an effect due to the thickness of the myocardium in the phantom, which in that region is thinner than the remaining muscle.

In Fig. 4.6, reconstructed D-SPECT images of the myocardium are displayed for all simulations performed without attenuation modelling. These images present a better distribution of the radiotracer activity within the myocardium. Regions of low uptake in simulations with attenuation modelling have higher activity in these images. The shape of the myocardium is more well-defined, with uniform ventricular walls. However,

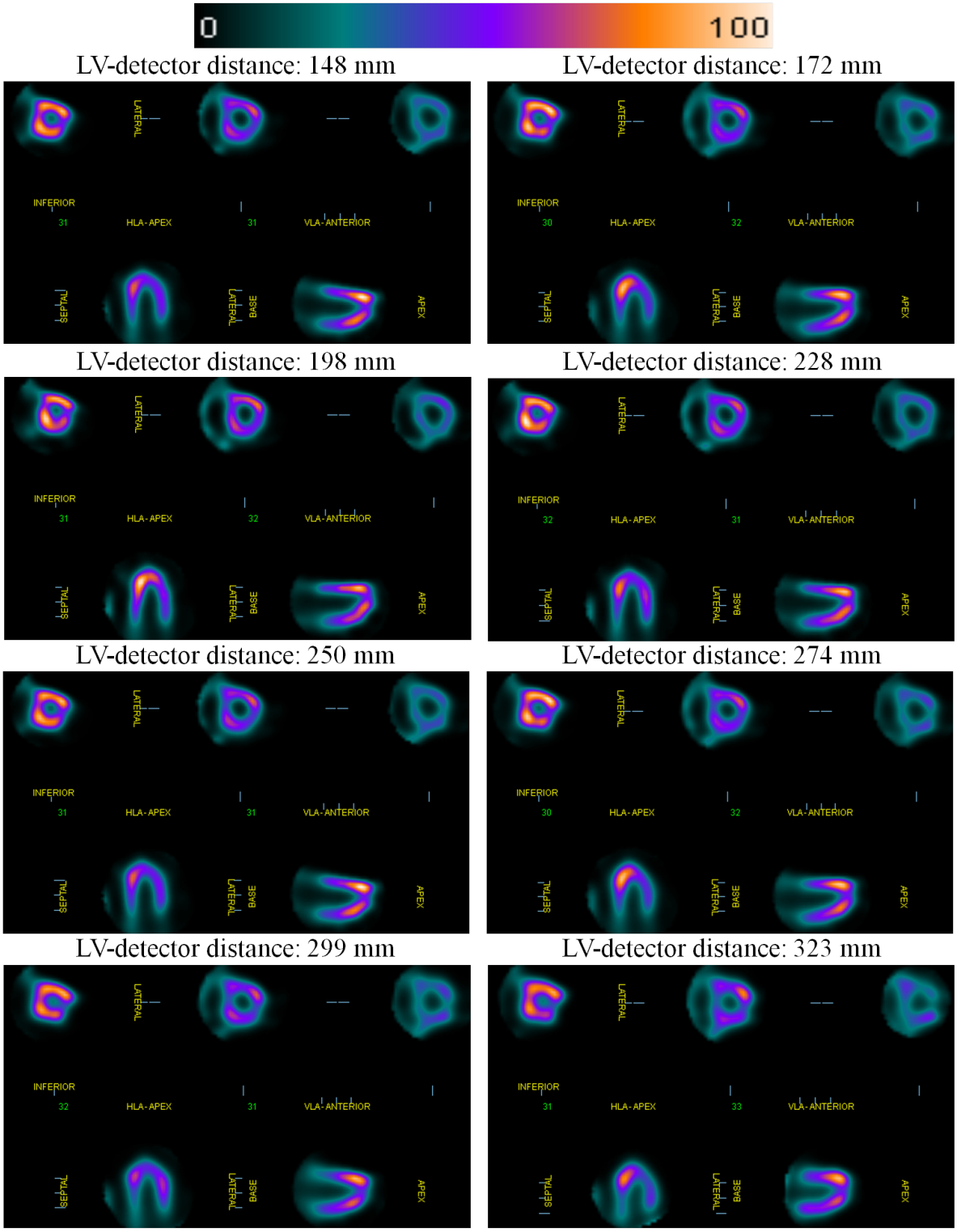

Figure 4.5: D-SPECT images simulated with attenuation modelling. From top to bottom and from left to right, the simulated LV-detector distance ranges from 148 *mm* to 323 *mm*. All images were extracted from the QPS program. On the top of the figure, the colour scale is shown.

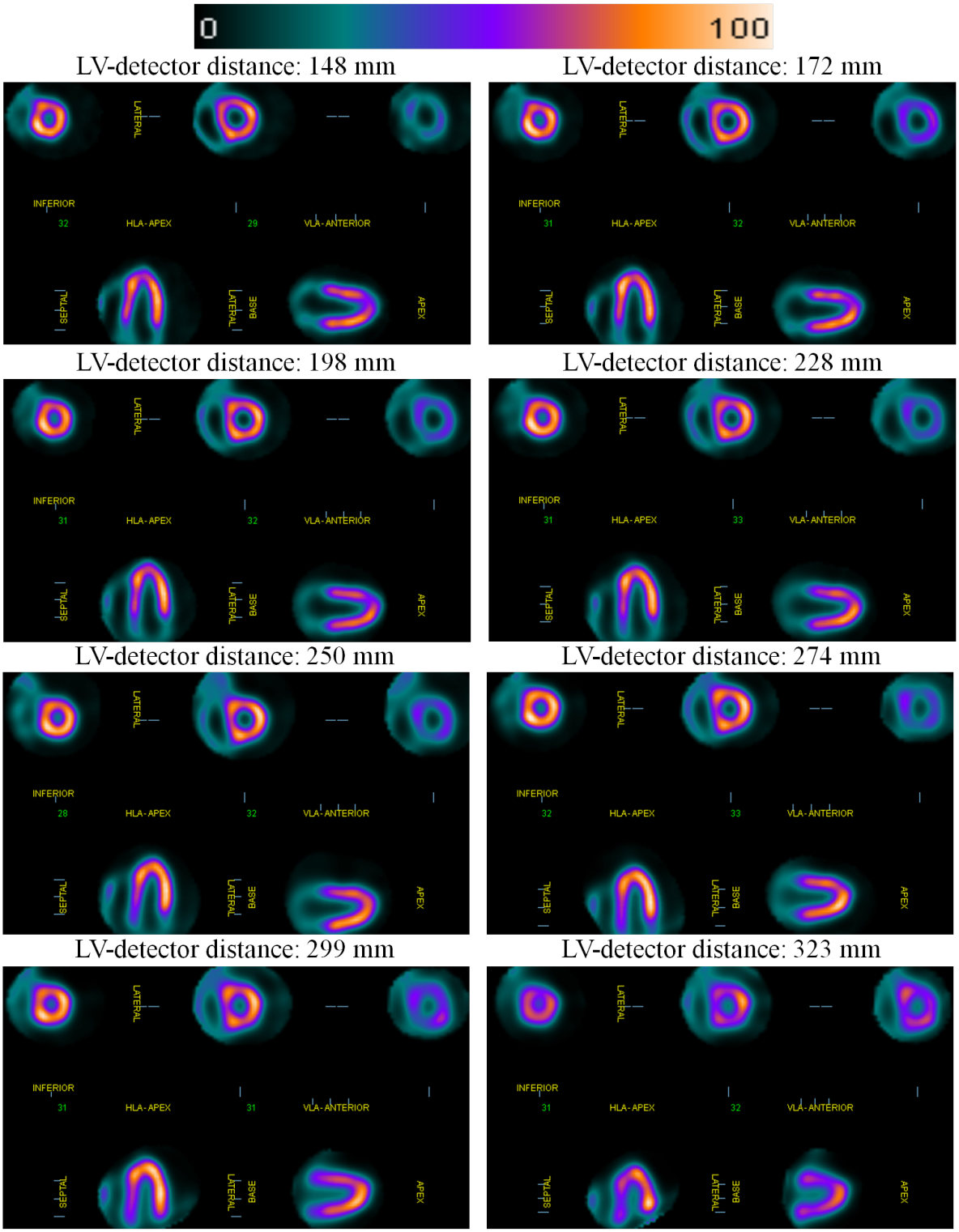

Figure 4.6: D-SPECT images simulated without attenuation modelling. From top to bottom and from left to right, the simulated LV-detector distance ranges from 148 *mm* to 323 *mm*. All images were extracted from the QPS program. On the top of the figure, the colour scale is shown.

as the LV-detector distance increases, particularly for distances higher than 228 mm, the septal wall starts to fade away in the reconstructed image. In addition, the shape of the myocardium becomes irregular, with the inclusion of some hot spots. In the last simulated position of the phantom, which corresponds to an LV-detector distance of 323 mm, the myocardium is totally distorted and the image presents an irregular distribution of activity.

The bull's eye plots obtained from the corresponding images of Fig. 4.5 and Fig. 4.6 are shown in Fig. 4.7 and Fig. 4.8, respectively. The first corresponds to simulations with attenuation modelling, and the latter corresponds to simulations without attenuation modelling. All bull's eye plots are displayed using the 20-segment model introduced in Section 2.4.4. For all simulations, there is a low activity in the outer ring of the bull's eye plots, highlighted by the greenish colour in segments 1 to 6. This effect may be due to a lower perfusion of the radiotracer in the basal region of the myocardium, or to the fact that the model of the heart defined in the QPS program has a greater length of the heart's long axis when compared to the heart of the phantom used in the simulations, resulting in the absence of perfusion in that region. This phenomenon of lower activity in the outer ring of the bull's eye plot is more evident in Fig. 4.8, because the distribution of the radiotracer activity is more uniform for simulations without attenuation modelling, as opposed to the acquired images for simulations with attenuation modelling (Fig. 4.7). In other words, there is a higher variability in the colour of the bull's eye plots in Fig. 4.7, which reflects the sparse distribution of activity within the myocardium. Despite having a more uniform distribution of activity, images in Fig. 4.8 also present some hot spots. These same regions in bull's eye plots of Fig. 4.7 show a good level of activity, but the remaining are of the bull's eye presents very low activity, contributing for the irregular uptake observed. Finally, for LV-detector distances of 299 mm and 323 mm, the corresponding bull's eye plots present high variability, with hot and cold regions. As previously pointed out when describing Fig. 4.5 and Fig. 4.6, all simulations show a cold spot in the centre of the bull's eye plots, which corresponds to segments 19 and 20. This is an effect of the thinner wall of the myocardium in the region of the apex.

The results for the quantitative analysis of the simulations are shown and discussed subsequently. They rely on the analysis of the bull's eye segments. Note that only bull's eye segments 7 to 20 were selected for this evaluation, because the basal region of the myocardium has low, or practically no activity. Therefore the inclusion of bull's eye segments 1 to 6 would not add relevant information to the analysis.

For each simulation performed with attenuation modelling, Fig. 4.9 shows the graph of bull's eye segments versus the segment value, which is proportional to the activity in that region of the myocardium. The relative activity values assigned to each segment

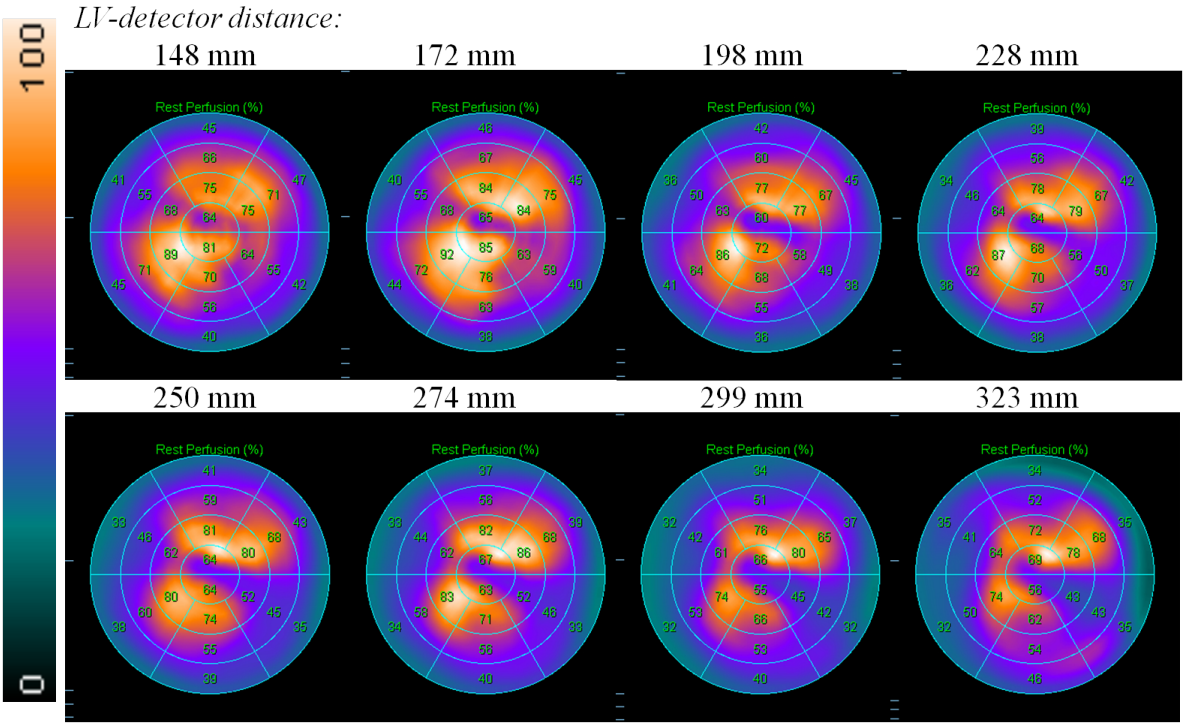

Figure 4.7: Bull's eye plots for simulations with attenuation modelling. From top to bottom and from left to right, the simulated LV-detector distance ranges from 148 *mm* to 323 *mm*. All images were extracted from the QPS program. On the left, the colour scale is shown.

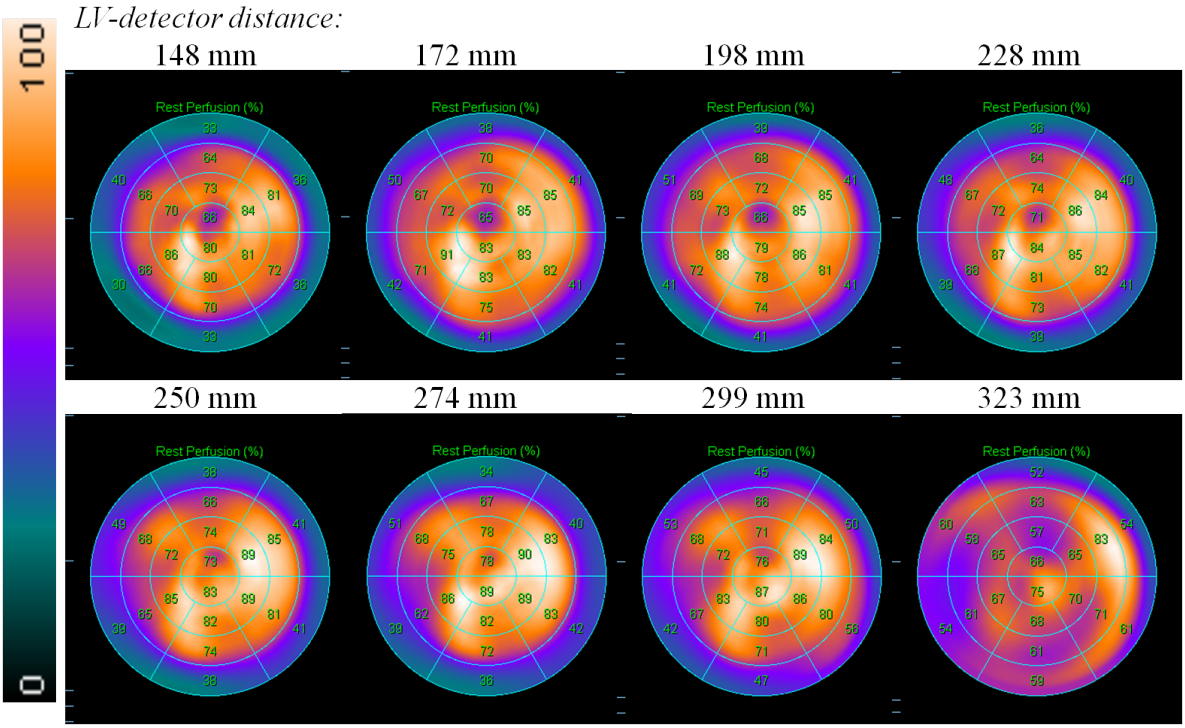

Figure 4.8: Bull's eye plots for simulations without attenuation modelling. From top to bottom and from left to right, the simulated LV-detector distance ranges from 148 *mm* to 323 *mm*. All images were extracted from the QPS program. On the left, the colour scale is shown.

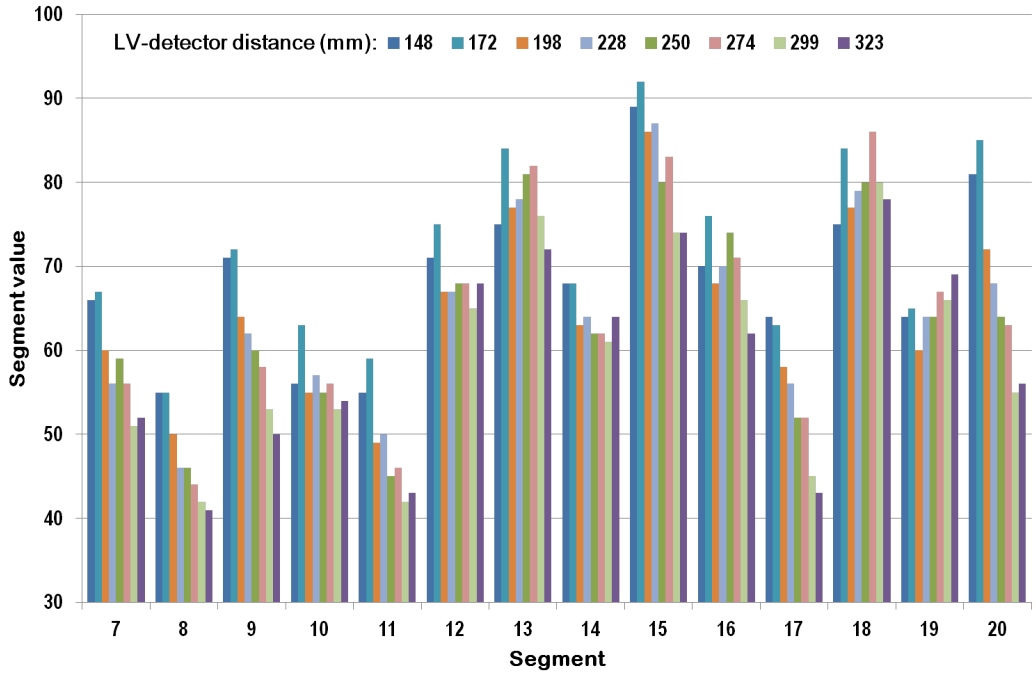

Figure 4.9: Graph of bull's eye segments versus the segment value for simulations with attenuation modelling. The eight colours represent each simulation, which corresponds to a different simulated LV-detector distance.

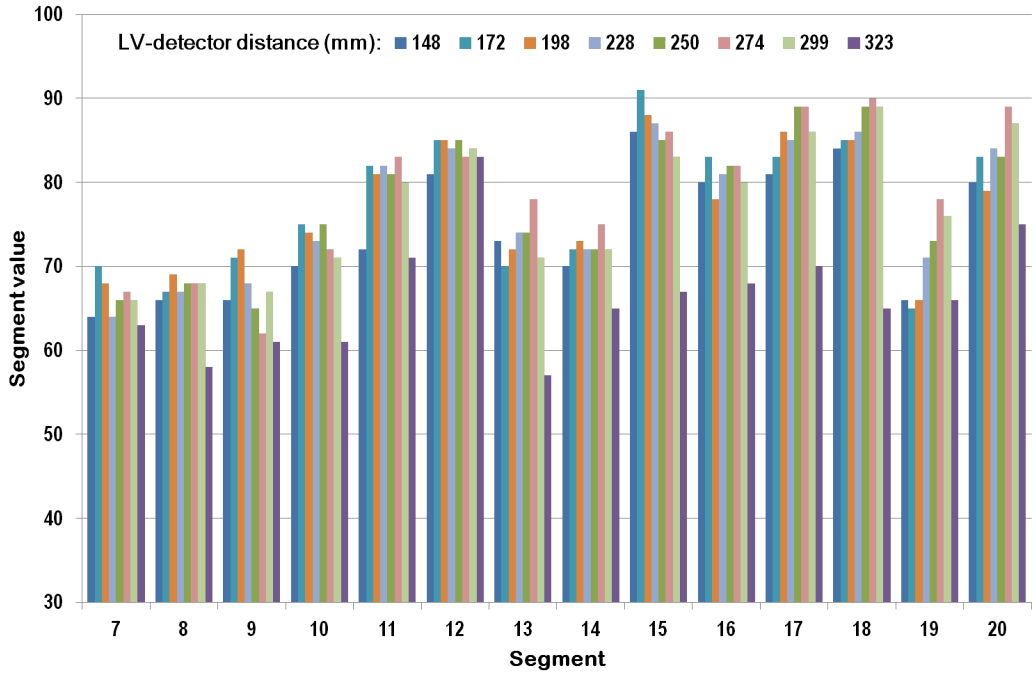

Figure 4.10: Graph of bull's eye segments versus the segment value for simulations without attenuation modelling. The eight colours represent each simulation, which corresponds to a different simulated LV-detector distance.

range from approximately 45 to 85, and they show high variability. Simulations for LV-detector distances of 148 *mm* and 172 *mm* present the highest measured relative activity in most bull's eye segments. The most affected segments, those presenting a lower level of activity, are segments 7 to 11, and 17. These segments correspond to the mid-septal region of the myocardium. In general, it seems that the graphs show a trend: with an increasing LV-detector distance, the activity for each bull's eye segment decreases.

Furthermore, Fig. 4.10 shows the graph of bull's eye segments versus the segment value for each simulation performed without attenuation modelling. Each segment has relative activity values ranging from approximately 65 to 85, reflecting a recovery in the estimated activity. However, such conclusions are not valid for the simulation with the furthest LV-detector distance - 323 *mm*-, in which the activity for each bull's eye segment is lower than that observed for all the remaining simulations. As opposed to what was observed in Fig. 4.9, with distance, there is not a significant difference in the values of relative activity, except for the case of the distance of 323 *mm*, as already mentioned. In addition, although in a smaller extent when compared to results presented in Fig. 4.9, variability between bull's eye segments is still present. In this case, the most affected segments are segments 7 to 10, 13, 14, and 19, which correspond to the mid-septal and antero-apical regions.

The results of the analysis with the COV values is summarised in Fig. 4.11. The scatter plot displays COV values as a function of LV-detector distance. Simulations performed with attenuation modelling are represented in light blue diamonds, and simulations performed without attenuation modelling are represented in dark blue squares. With attenuation, the COV of bull's eye segments increases from 0.14 to 0.21, considering LV-detector distances up to 274 *mm*. Then it remains approximately constant for the three furthest simulated LV-detector distances. On the other hand, without attenuation, the COV remains close to 0.10 independent of the LV-detector distance.

Box plots for the bull's eye segments distribution as a function of distance are shown in Fig. 4.12 and Fig. 4.13, for simulations with and without attenuation modelling, respectively. As illustrated by the red line, in the presence of attenuation, the median relative activity for each simulation decreases with distance, even though the whole phantom is displaced, and not only the heart. Without attenuation, the median relative activity is approximately constant, with small variations. However, for the simulation with an LV-detector distance of 323 *mm*, there is a drop in the median relative activity due to the low activity and distortion present in the reconstructed myocardium.

In conclusion, these results show that the reconstructed cardiac images are affected by both LV-detector distance and attenuation. Reconstructed images degrade with

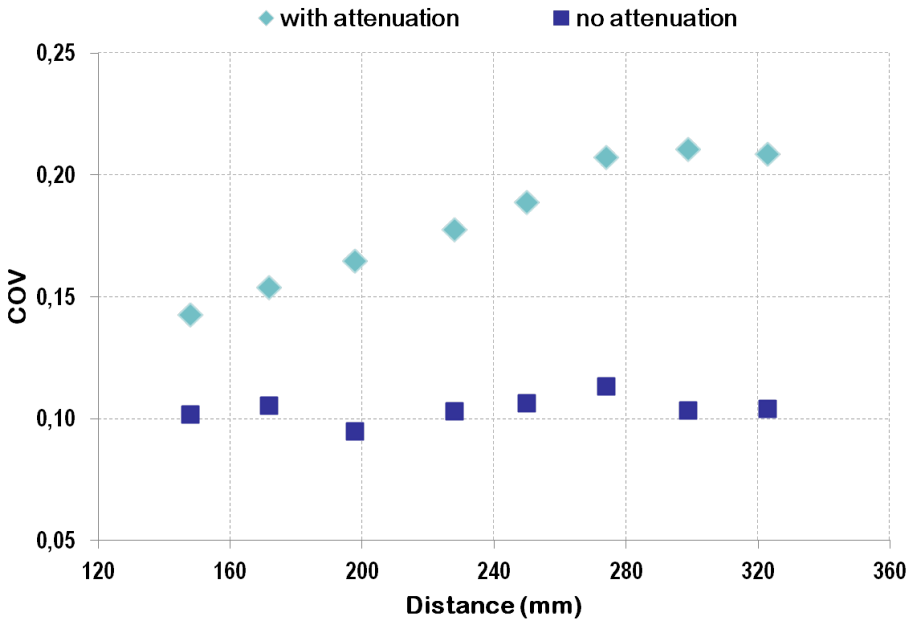

Figure 4.11: Scatter plot of LV-detector distance versus COV values. Light blue diamonds correspond to COV values for simulations with attenuation modelling and dark blue squares correspond to COV values for simulations without attenuation modelling.

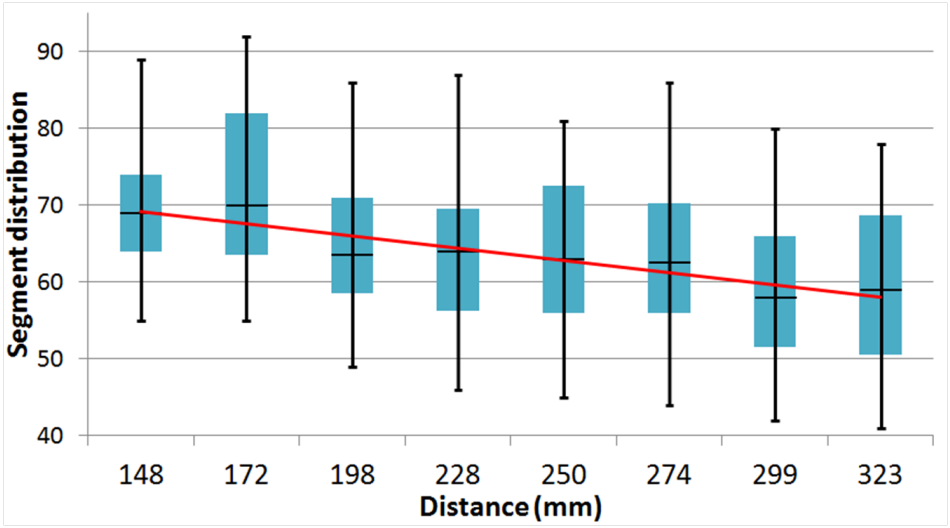

Figure 4.12: Box plot graph for simulations with attenuation modelling. Each box plot corresponds to the bull's eye segment distribution for one particular LV-detector distance. The red line highlights the trend of all medians.

greater LV-detector distances, specially when the heart is almost outside the FOV. The most affected myocardial region is the septal wall. In addition, cardiac images improve for simulations without attenuation modelling. As previously explained, these type of simulations can be considered similar to attenuation corrected images. Therefore these results point out the importance of performing attenuation correction.

It is important to emphasize the limitations of this study. Neither noise nor scatter

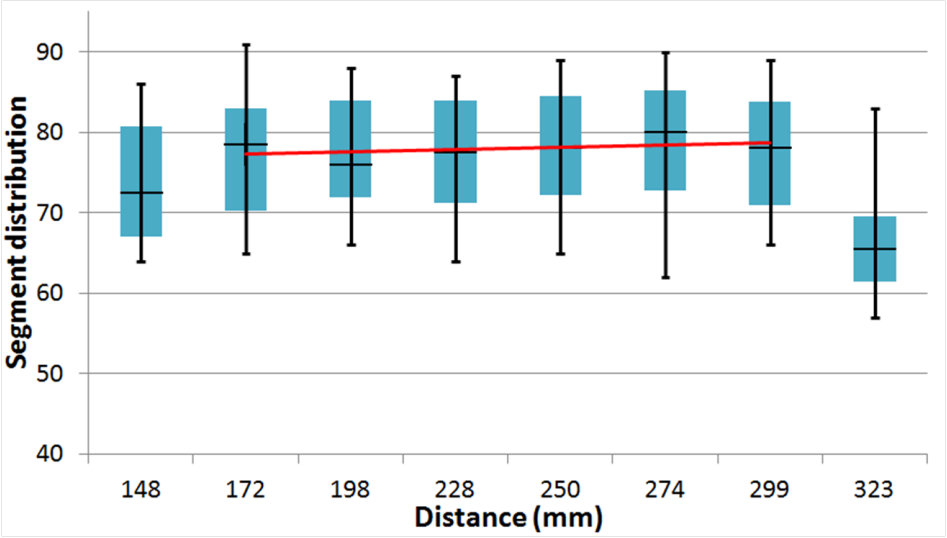

Figure 4.13: Box plot graph for simulations without attenuation modelling. Each box plot corresponds to the bull's eye segment distribution for one particular LV-detector distance. The red line highlights the trend of all medians, except for the first and last simulations, which are not taken into account.

were modelled in the performed simulations. These issues would contribute to a poorer image quality, but they could also affect differently the reconstructed D-SPECT image, depending on the simulated parameters. Therefore, simulations were carried out noise-free and scatter-free to ensure that the effects observed in the corresponding reconstructed images were due to the LV-detector distance and attenuation.

Another issue is related to the displacement of the phantom. In order to simulate different LV-detector distances, the whole phantom was displaced in the FOV, instead of moving only the phantom's heart. The latter would be possible to simulate, changing the size of the phantom's torso to resemble a bigger or fatter patient. However, in this case it would be expected that the amount of attenuation in the patient would be greater than in the actual simulations. Despite being an interesting study, this set up was not simulated. Provided that the whole phantom was displaced, it simulates a mispositioning of the patient in relation to detectors, a situation that may occur clinically.

At last, the fact that all quantitative analyses were based on bull's eye segments can bias the results. Nevertheless, only bull's eye segments 7 to 20 were taken into account for the analysis, eliminating one possible source of error. In addition, the results seem consistent to what was expected. Moreover, the information obtained by a qualitative analysis of the reconstructed images is also in agreement with the quantitative results.

4.4 Conclusion

The D-SPECT is a new system, with a novel scanning geometry. Due to the fact that each detector can rotate independently, and a region-centric acquisition can be performed, issues related to the geometry of the acquisition may affect the reconstructed images. Effects of attenuation are also problematic for the quality of the acquired image. Therefore the aim of this study was to investigate whether parameters such as LV-detector distance and attenuation affected myocardial reconstructed images.

The obtained results demonstrate that the uniformity and shape of the reconstructed myocardium are affected by the LV-detector distance and attenuation.

With attenuation, activity decreases with distance, specially for distances in which the myocardium is almost outside the FOV.

Whereas without attenuation, the distribution of activity within the reconstructed myocardium improves, but it drops for large LV-detector distances. These results suggest that not only LV-detector distance, but also attenuation is an issue that must be taken into account in order to obtain good-quality cardiac images.

These findings show the importance of attenuation correction algorithms in order to correct for attenuation artefacts that may interfere with clinical diagnosis.

Chapter 5

Effects of Respiratory Motion on D-SPECT Images

5.1 Motivation and Objectives

The effects of respiratory motion in acquired myocardial images have been the focus of different studies in the field of SPECT imaging, as addressed previously in Section 2.3.3.

Considering a static myocardium, in other words a myocardium that does not contract or move due to breathing during the SPECT acquisition, the reconstructed image obtained with a standard scanning protocol will present a good estimation of the tracer activity, with a uniform distribution within the myocardium. In some cases, in which the apex of the left ventricle is thinner than the myocardial walls, the tracer uptake in that region is lower, due to the thickness of the myocardium on that region. On the other hand, when accounting for respiratory motion of the heart during the acquisition, the myocardial walls will be blurred and thicker in comparison to images of the heart in which no respiratory motion is present. This effect is due to the periodic motion of the heart as a result of breathing, that constantly changes the position of the heart in the FOV.

In the D-SPECT camera, although it is a cardiac-dedicated camera, there are additional problems in the reconstructed images of the heart. For example, the novel camera geometry and the fact that at each angle of the scanning pattern, each detector only acquires photons from part of the myocardium, as opposed to standard SPECT cameras (Fig. 5.1). Standard systems acquire photons from the whole heart, independent of the position of the detector.

As respiratory motion of the heart is unavoidable during the scan, acquired projections will be blurred or will not match. Blurring occurs because the periodic motion of the heart creates uncertainty in the position of the heart being imaged. Therefore the

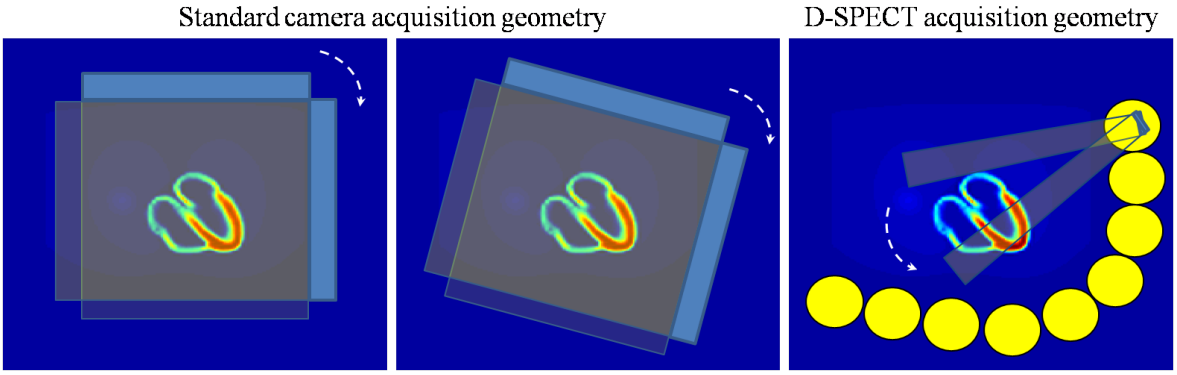

Figure 5.1: Scanning geometry. Schematic representation of two positions of the camera for a standard SPECT system (two leftmost images) and two positions of one D-SPECT detector (rightmost image), with the corresponding scanned area of the heart emphasized by the light yellow colour. The heart is displayed in a transaxial view.

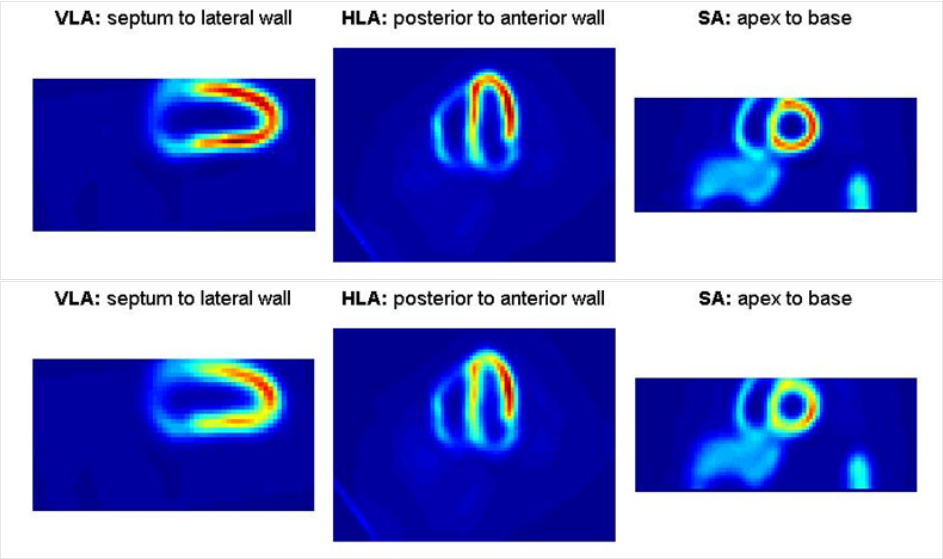

Figure 5.2: Respiratory-induced blur on cardiac images. Both top and bottom images are slices of reconstructed SPECT images, displayed on the three axes of the heart. The image on the top corresponds to the heart of a static phantom, and the bottom image corresponds to the same heart but with the effects of respiratory motion.

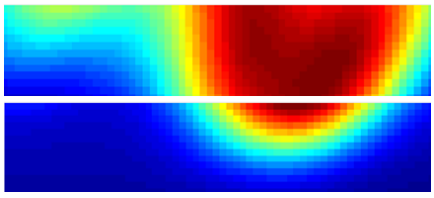

Figure 5.3: D-SPECT projections. Both images correspond to projections acquired from the heart, obtained with one detector at two consecutive angles.

position of the heart in the acquired image will be similar to an average of the range of positions taken by the heart during the scanning time. Consequently myocardial walls will appear thicker than they truly are (Fig. 5.2).

In addition, since one detector only scans part of the myocardium at one angle of acquisition, when the detector rotates to scan the next angle, the heart may not be in the same position, leading to inconsistencies in the acquired data (Fig. 5.3), as well as artefacts in the corresponding reconstructed images.

When included in the reconstructed image, artefacts can be interpreted as perfusion defects. In addition, poor image quality due to blurring may also affect the detection of small lesions. As a result, these issues have great impact on the accuracy of the diagnosis. Therefore, artefacts can compromise cardiac assessment, because physicians rely on the analysis of the reconstructed image for the diagnosis.

The aim of this study is to examine the effects of respiratory motion on D-SPECT's reconstructed images of the heart. Therefore different parameters were assessed, such as the phase shift between the timings of the acquisition process and the respiratory cycle, the number of acquired angles per detector in a scan, the total scanning time, and the pattern of the respiratory cycle. As the D-SPECT system is a relatively new SPECT scanner, only available in a few countries worldwide, these problems have not been addressed yet.

5.2 Methods

The methodology used in the investigation of the effects of respiratory motion in D-SPECT reconstructed images can be summarised as follows (Fig. 5.4). First, a set of human torso phantoms are created using the 4D NCAT software, which takes into account the respiratory motion of the heart. Then each created phantom is given as input to the D-SPECT *Simulator* to estimate projection data. In this process, different scanning parameters are selected and modified to study different issues. Projection data are then reconstructed with the clinical reconstruction process, which makes use of the OSEM algorithm. The resulting images are co-registered against a reference cardiac image in order to obtain the simulated images. The reference image is an average of all simulated heart positions during one respiratory cycle, which corresponds to an image acquired for a long time. Finally, simulated images are analysed qualitatively and quantitatively.

In the following sections, each step of the methodology is described in detail.

5.2.1 Generating the Phantoms

In order to include motion of the myocardium due to breathing, a torso phantom was simulated using the 4D NCAT program, which accounts for a fourth dimension -

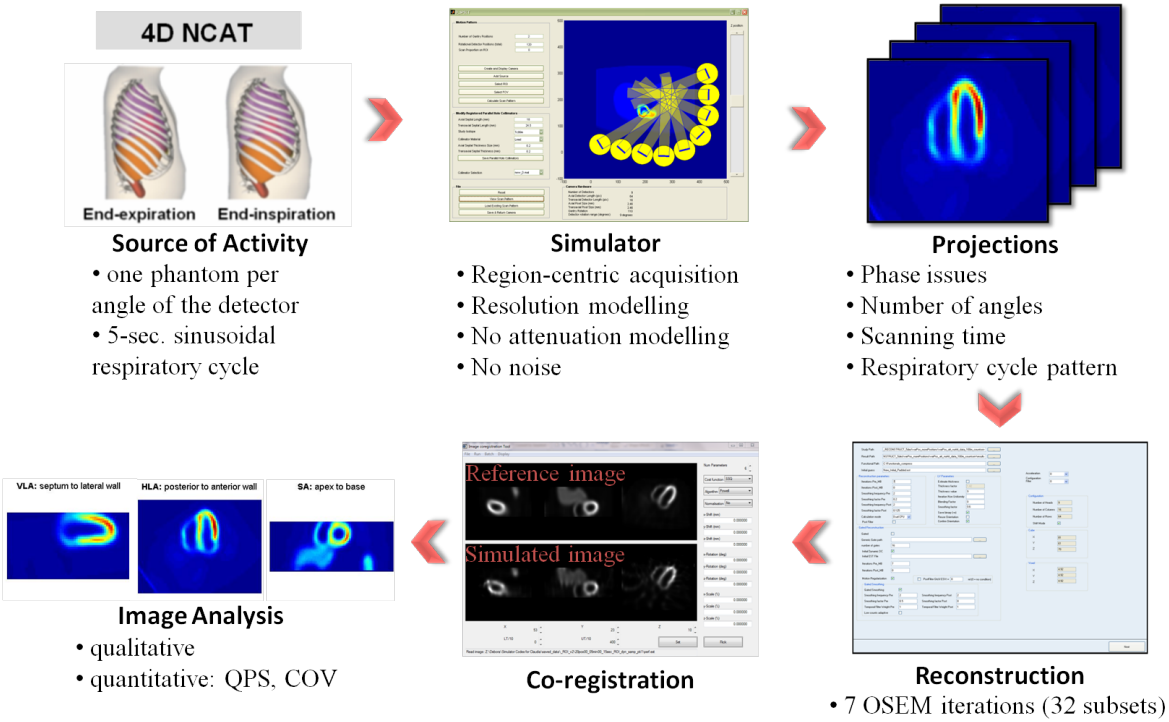

Figure 5.4: Methodology of the second study. This diagram represents the steps performed to investigate the effects of respiratory motion in the reconstructed D-SPECT images.

time - besides the three standard dimensions related to the dimensions of the phantom.

In the input parameter file of the 4D NCAT, instructions were given to save the activity file, which will be the source of activity in the D-SPECT *Simulator*, and the file with the corresponding attenuation coefficients, at each time frame of the total simulation time. The total number of output time frames was set to 32 due to constraints in the NCAT program, which crashes for a higher number of time frames. As a result, at the end of one simulation, i.e. one respiratory cycle, 32 phantoms are generated. Each phantom corresponds to a different position of the heart due to breathing.

The variable that accounts for motion of the heart was set to *respiratory motion only*, thus excluding the contraction of the myocardium from the simulation. Therefore, only the effects of respiratory motion are analysed. Regarding the parameters of the respiratory motion, the respiratory cycle period was set to 5 seconds, starting at full exhalation of the torso. The maximum displacement of the diaphragm was set to 2 *cm* and the maximum anterior-posterior expansion of the chest wall was set to 1.2 *cm*. All these parameters are in agreement with a normal tidal breathing.

Since the number of output time frames is 32, and the simulation of one respiratory cycle lasts for 5 seconds, the time per frame is 0.156 seconds, which corresponds to the minimum possible time sampling in a simulation. In other words, for this simulated respiratory cycle, 0.156 seconds is the minimum time that one detector can spend per angle of detector during the acquisition. As a result, it is impossible to simulate faster

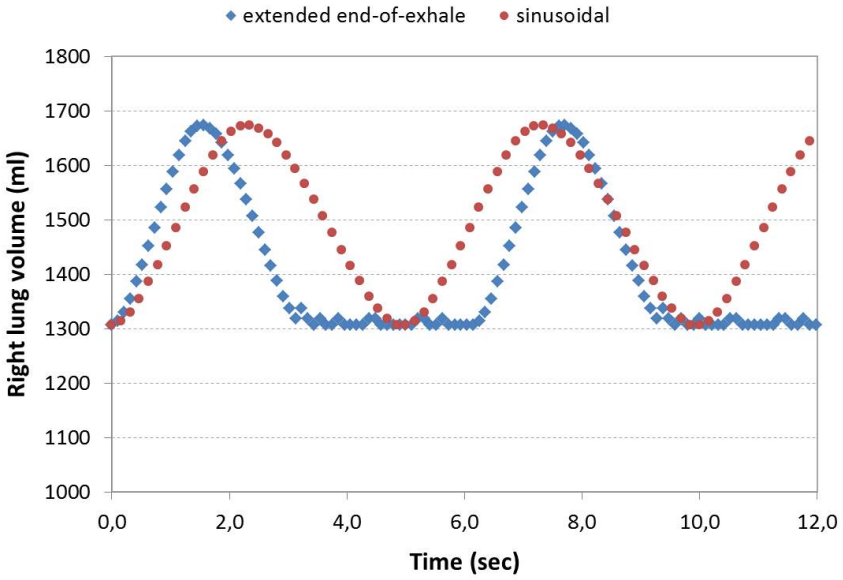

Figure 5.5: Graph of the simulated breathing patterns. The horizontal axis on the graph shows the time in seconds, and the vertical axis shows the right lung volume in *ml*. Each point in the graph corresponds to a simulated time frame. The sinusoidal respiratory cycle is represented in red circles and the extended end-of-exhale breathing pattern is represented in blue diamonds.

acquisitions due to restrictions in the maximum output frames.

As shown in Fig. 5.5 in red, the respiratory cycle simulated by the 4D NCAT program has a sinusoidal breathing pattern. Therefore, a more realistic breathing pattern was created to study its effects on the reconstructed images. The created respiratory cycle resembles an extended end-of-exhale breathing pattern, and it is shown in blue in Fig. 5.5.

In order to use the created phantoms in the D-SPECT *Simulator* as the source of activity, the binary files obtained with the 4D NCAT software were converted to MATLAB structures. Then, according to the required simulation, the 32 phantoms were repeated over time so that the total breathing time equals the scan time.

5.2.2 Performing the Simulation

The next step in the simulation process consists in the acquisition of projection data. This is performed using the D-SPECT *Simulator* developed at UCL, which was described in detail on Section 2.4.2.

In the `Set Up Camera` interface, the D-SPECT camera was selected, with the default collimation parameters. In all simulations, a ROI delineating the region of the heart was selected (Fig. 5.6) and the scan proportion on the ROI was set to 0.6, which is in agreement with the standard acquisition scan. Moreover, the scan pattern was computed with the detector leading edge algorithm, and the number of gantry positions was set to 2, corresponding to the fact that a D-SPECT acquisition consists of two scans with

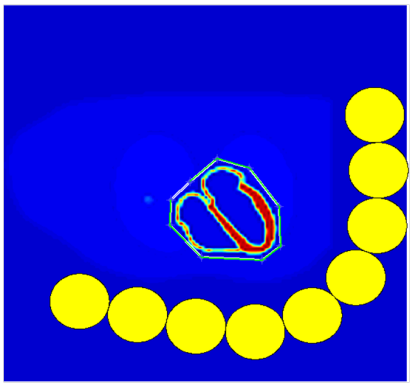

Figure 5.6: Selection of a ROI. This is the ROI used to calculate the motion pattern of the D-SPECT detectors in this study.

a 9°-rotation in between. Simulations were performed with resolution modelling and angles grouped to 1 degree, in order to estimate projections more quickly, but noise and attenuation were not modelled to eliminate sources of image degradation apart from respiratory motion. All these parameters were saved in a `handles` variable to perform the simulation with the newly developed scripts (Section 3.1), instead of the standard code implemented for the D-SPECT *Simulator*, which can only reproduce a static acquisition.

Parameters such as the phase shift between the acquisition process and the respiratory cycle, the number of acquired angles in a scan, the total scanning time and the pattern of the respiratory cycle were modified according to the performed study. Regarding the phase study, three different phase shifts were simulated. In relation to the beginning of the acquisition, one corresponds to mid-exhalation (phase shift **a**), one to full-exhalation (phase shift **c**), and one midway between the two (phase shift **b**). They will be referred to as phase shift **a**, **b**, and **c**, from here on. In addition to the phase shifts, different temporal samplings were also simulated. For the remaining simulations, the heart is in the position of full-exhalation when the acquisition begins. Concerning the angular sampling study, three different numbers of acquired angles per detector were simulated. Simulations were also performed with short acquisition times, and longer scan times.

Table 5.1: Simulated parameters of the phase study. The check-mark symbol ✓ indicates the performed simulations.

		angular sampling (# angles/detector)			
		20			200
	time sampling (sec)	2.0	2.5	3.0	2.5
phase shift	**a**	✓	✓	✓	✓
	b	✓	✓	✓	✓
	c	✓	✓	✓	✓

Table 5.2: Simulated parameters for three studies. The check-mark symbol ✓ indicates the performed simulations for the breathing pattern, scan time, and angular sampling study.

		breathing pattern		angular sampling (# angles/detector)		
		sinusoidal	extended end-of-exhale	20	40	120
scan time (sec)	3	✓	✓	✓		
	6	✓	✓	✓		
	12	✓	✓	✓		
	24	✓	✓	✓		
	41	✓		✓		
	60	✓		✓	✓	✓
	120	✓		✓		

Furthermore a more realistic respiratory cycle pattern - extended end-of-exhale - was also simulated to study the influence of the breathing pattern on the reconstructed images. Tab. 5.1 and Tab. 5.2 summarise the simulated parameters for all studies.

5.2.3 Image Reconstruction

After having the projection data saved in `.csv` files, the next step is reconstruction of these data to obtain an image. Thus, those files are given as input to the reconstruction software provided by Spectrum Dynamics, Caesarea, Israel. In order to accelerate and automatize this process, several images are reconstructed one after the other, using a batch file. This batch file is generated using a developed MATLAB script. Mainly the `.bat` file has a set of *strings* that indicate the path to the reconstruction executable, to the `.csv` files to be reconstructed and to the parameter file `reconstructionParameters.ini`. In addition, it has an instruction that makes the reconstruction executable run. Using this method, it is less probable that errors may be included from one simulation to another.

The parameters of the reconstruction process are defined in the `reconstruction-Parameters.ini` file. It applies the OSEM algorithm with 7 iterations and no post-reconstruction filter.

The output of the reconstruction software is a `.est` file with the reconstructed image. However, at this stage, the image is not ready for the analysis yet. Because the position of the heart is constantly changing during the acquisition, the reconstructed myocardium will not be in the same position in the image for all studies. Therefore all simulated images need to be co-registered before being analysed.

For the registration step, an IDL-based co-registration code was used. A rigid registration with 6 degrees of freedom was defined in the interface, and a Powell cost-function was selected. For all studies, the simulated image was co-registered with a template image. The template image was defined as the average of the 32 frames in one respiratory cycle. It is important to note that for each acquisition protocol, a different

template image was generated. For example, for an acquisition with 20 angles per detector, projection data obtained with the same angular sampling were averaged to generate the template image, instead of using projection data obtained with for example 60 angles per detector. In contrast, for the same acquisition protocol, a batch file was created to perform the co-registration of all simulated images with the same angular sampling to the template image, using always the same registration parameters.

5.2.4 Image Evaluation

The final step of the methodology regards the evaluation of the reconstructed images. A qualitative assessment was performed, comparing each simulated image against the other simulated images and a reference image. The reference image was defined as the average of the 32 frames in one respiratory cycle.

In addition, each reconstructed myocardium was divided into 12 regions, using the region-analysis tool presented on Section 3.3. Then, for each simulation, the mean activity was calculated in each myocardial region, as well as the standard deviation in that region. These data were then summarised in a column graph of mean activity versus the correspondent region of the myocardium, with error bars corresponding to the standard deviation.

Furthermore statistical measures were calculated for each simulated cardiac image, such as the correlation coefficient R^2 and the normalised root-mean-square error NRMSE, in order to extract further quantitative and discriminatory information. Both measures were calculated with two vectors of mean activities, one obtained from the reference image, and the other obtained from a simulated image. The value of R^2 was obtained with the MATLAB `corr` function, which gives the linear correlation coefficient between two datasets. Additionally, the NRMSE was calculated by the following formula (Eq. 5.1[72]):

$$\text{NRMSE} = \frac{\text{RMSE}}{x_{max} - x_{min}} = \frac{\sqrt{\frac{\sum_{i=1}^{n}(x_{1,i} - x_{2,i})^2}{n}}}{x_{max} - x_{min}} \tag{5.1}$$

where $\theta_1 = [x_{1,1}; x_{1,2}; ...; x_{1,n}]$ is one dataset and $\theta_2 = [x_{2,1}; x_{2,2}; ...; x_{2,n}]$ is the other dataset of mean activity values.

5.3 Results and Discussion

In this section, results of each study are going to be presented and analysed separately in different sub-sections.

5.3.1 Phase study

In Fig. 5.7, the results of the phase study are presented. Analysing these reconstructed images, it is possible to observe that the phase between the respiratory cycle and the acquisition protocol interferes with the quality of the cardiac reconstructed images. In general, these images show non-uniform distribution of activity within the myocardium, and low activity both in the anterior, posterior and septal wall. In addition, there is a small distortion of the myocardium, more pronounced for the simulations performed with phase shift **a**, which is when the acquisition starts with the phantom's heart in the position of mid-exhalation.

Note that for the simulation with a time sampling of 2.5 seconds and phase shift **c**, which is when the acquisition starts with the phantom's heart in the position of full-exhalation, there is a good reconstruction of the myocardium, without artefacts. This effect can be explained by the fact that the time sampling is half the duration of one respiratory cycle, and the phase shift is **c**. Because the variation of the respiratory cycle amplitude is the same in each acquisition interval due to the sinusoidal breathing pattern, and detectors acquire during exactly half the time of the respiratory cycle at each angle, the resulting projections will match perfectly. So the reconstruction of the myocardium is processed as if there was no breathing during the acquisition, and the reconstructed heart is not affected by the respiration. For the simulations with phase shifts **a** and **b**, the variation of the respiratory cycle amplitude is different at each acquisition angle, therefore projections do not match, and artefacts are included in the reconstruction.

Simulations with 2.5 seconds and different phase shifts were also performed with 200 angles of detection, instead of only 20. Fig. 5.8 shows the reconstructed images for those simulations. In the case of an angular sampling of 200, the reconstruction is independent of the phase shift between the respiratory cycle and the acquisition process. As they result in a good reconstruction, it can be concluded that the respiration does not interfere with the reconstruction process for a sufficient large number of acquisition angles, even though the time sampling coincides with half the respiratory cycle.

Furthermore, as the temporal sampling increases, i.e. detectors spend more time acquiring at each angle of acquisition, the errors in the reconstructed images seem to decrease (Fig. 5.7). However more data are needed to support this conclusion.

Column charts of Fig. 5.9, Fig. 5.10, and Fig. 5.11 show the mean activity as a function of myocardial region for simulations with 2 seconds, 2.5 seconds, and 3 seconds of time sampling, respectively. Each coloured column corresponds to a different simulated phase shift between the respiratory cycle and the acquisition: red - **a**, yellow - **b**, and cyan - **c**. The dark blue column corresponds to the reference image, and the error bars

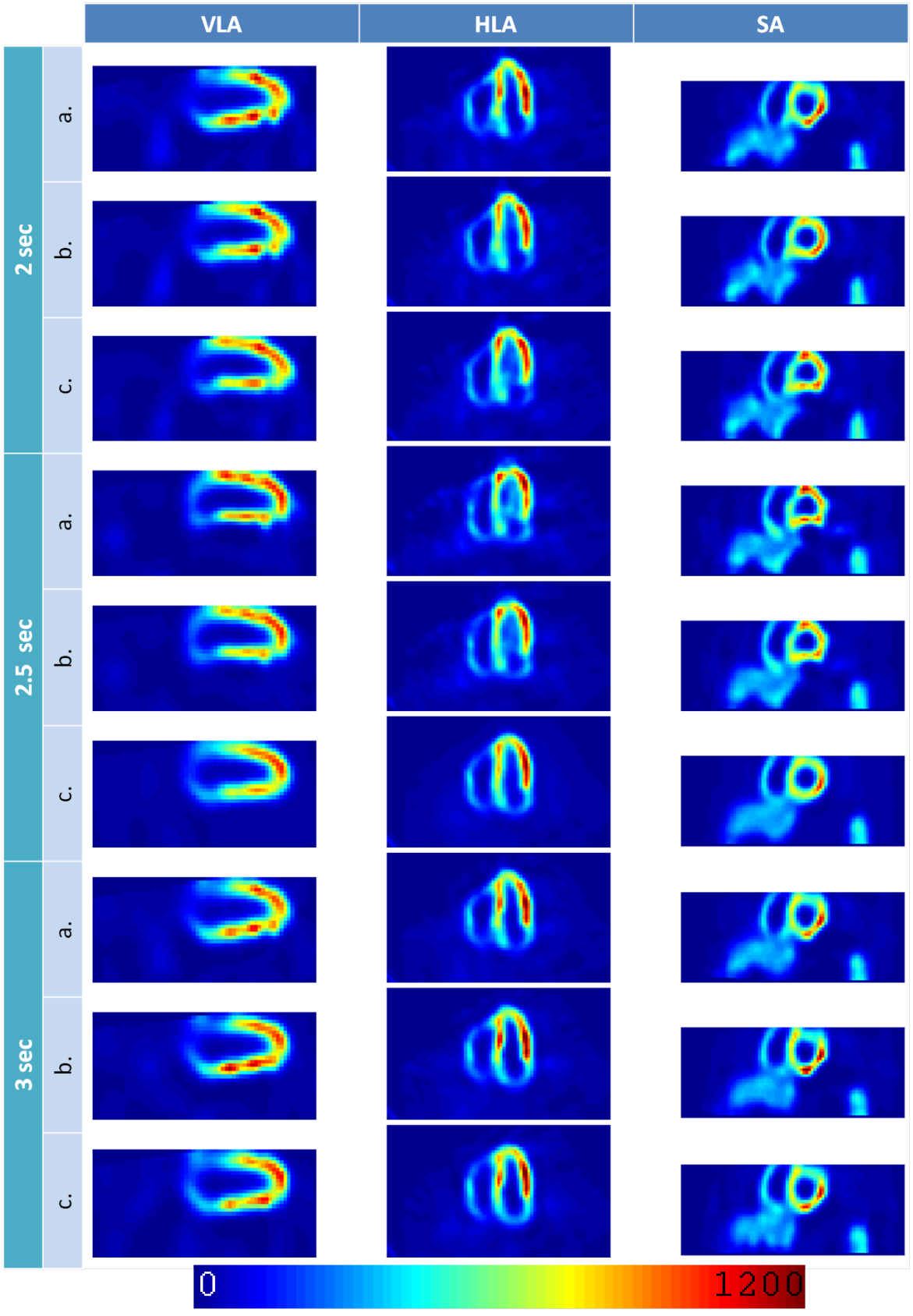

Figure 5.7: Results of the phase study. Myocardial reconstructed images acquired with three different time samplings - 2, 2.5 and 3 seconds per angle of detectors -, and three different phase shifts between the acquisition and the respiratory cycle - **a**, **b** and **c**. On the bottom, the colour scale is shown.

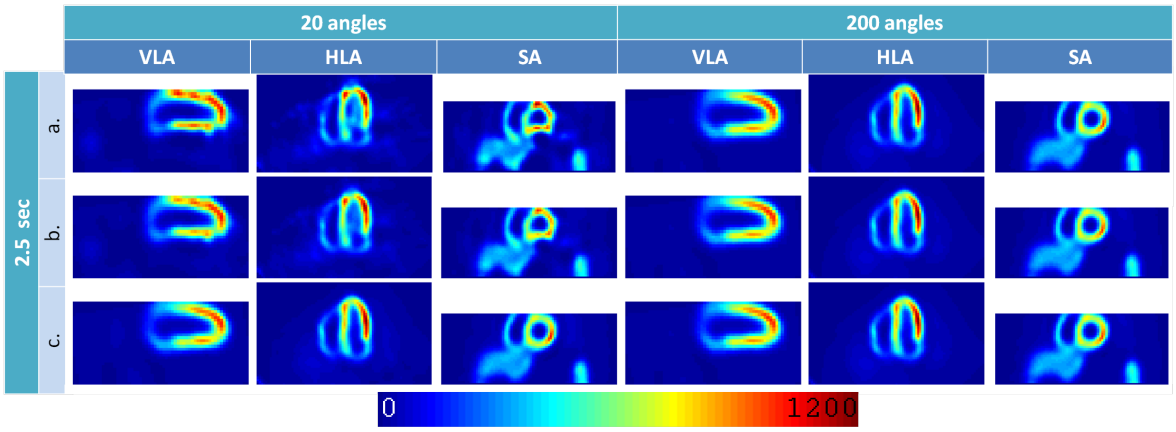

Figure 5.8: Results of the phase study combined with a different angular sampling. Comparison of myocardial reconstructed images acquired with two angular samplings - 20 and 200 angles per acquisition - for simulations with a time sampling of 2.5 seconds per angle and three phase shifts (**a**, **b** and **c**) between the acquisition and the respiratory cycle. On the bottom, the colour scale is shown.

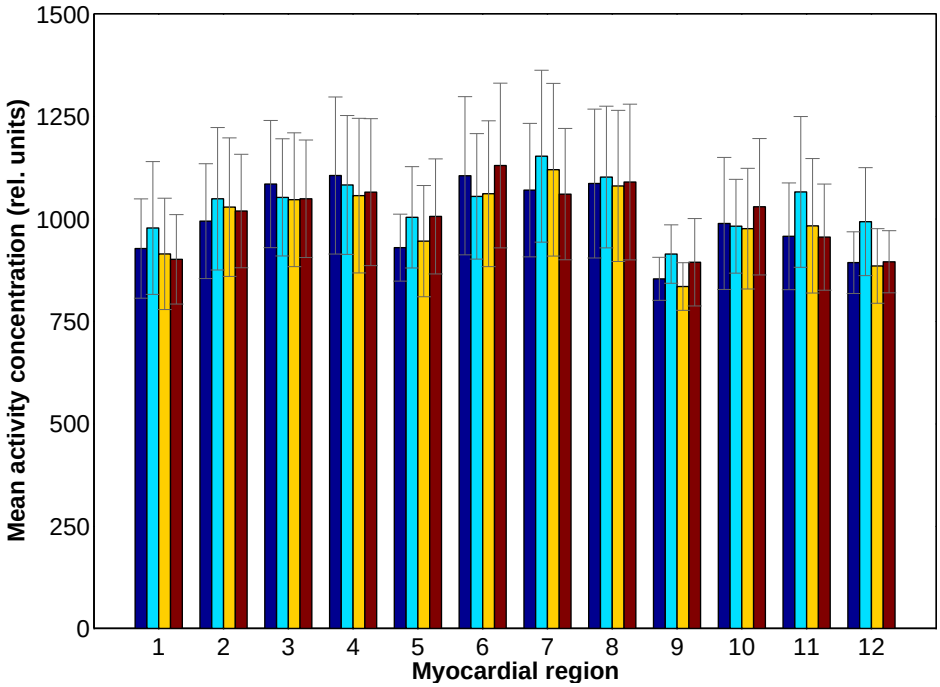

Figure 5.9: Graph of the mean activity for simulations with $2s$ of sampling time. Activity is shown as a function of myocardial region. Each colour represents a simulation with a different phase shift: **a** - red, **b** - yellow, and **c** - cyan. The dark blue bar corresponds to the mean activity of the reference image. The error bars correspond to the standard deviation of the activity in the selected region.

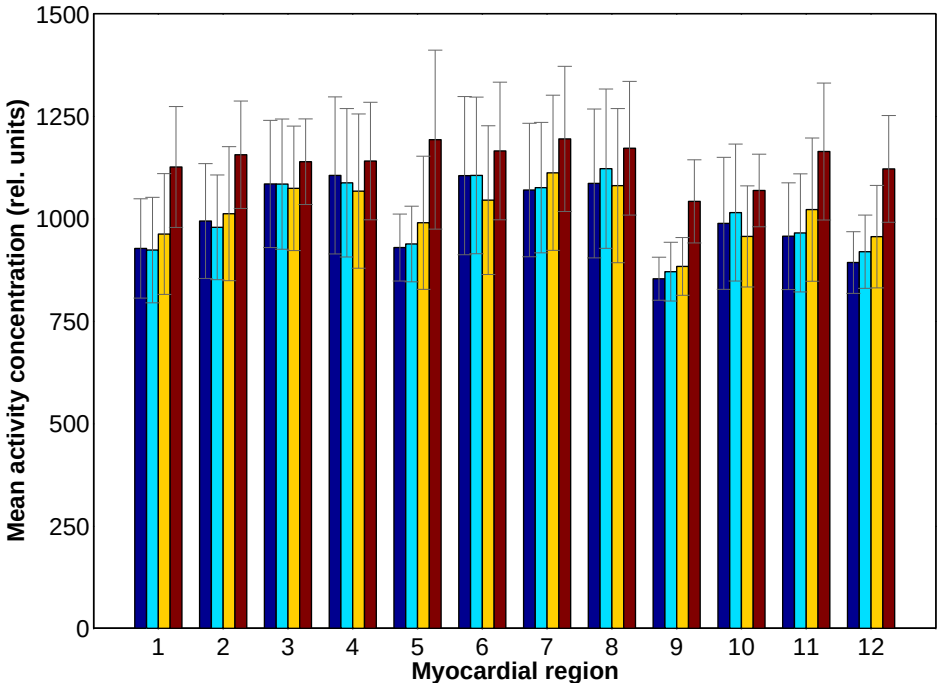

Figure 5.10: Graph of the mean activity for simulations with 2.5s of sampling time. Activity is shown as a function of myocardial region. Each colour represents a simulation with a different phase shift: **a** - red, **b** - yellow, and **c** - cyan. The dark blue bar corresponds to the mean activity of the reference image. The error bars correspond to the standard deviation of the activity in the selected region.

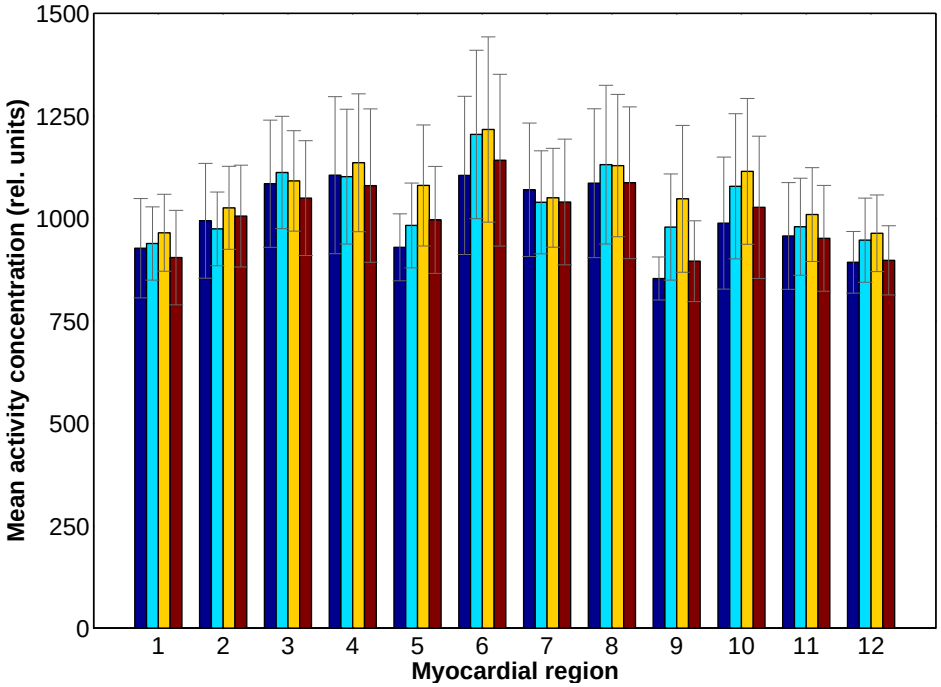

Figure 5.11: Graph of the mean activity for simulations with 3s of sampling time. Activity is shown as a function of myocardial region. Each colour represents a simulation with a different phase shift: **a** - red, **b** - yellow, and **c** - cyan. The dark blue bar corresponds to the mean activity of the reference image. The error bars correspond to the standard deviation of the activity in the selected region.

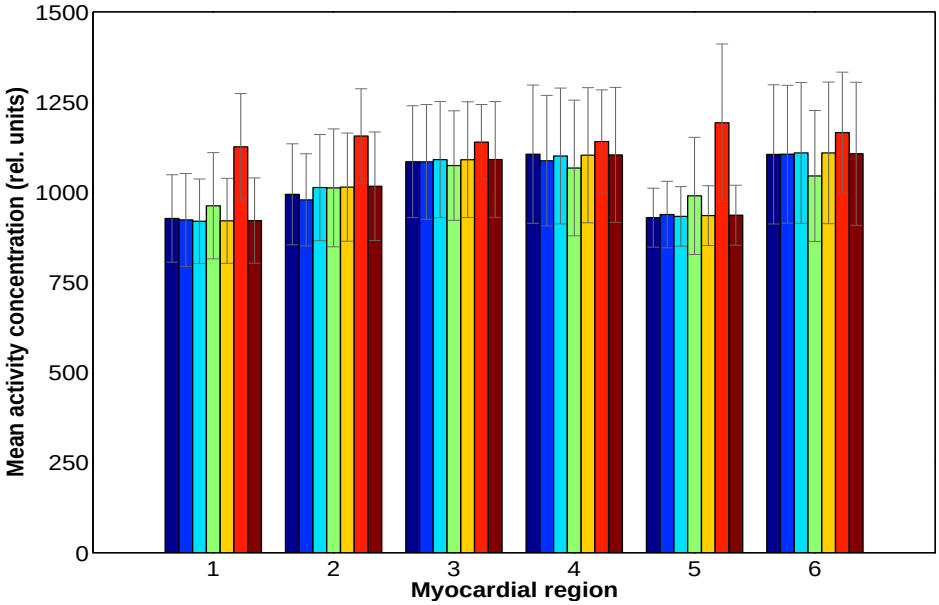

Figure 5.12: Graph of the mean activity for simulations with 2.5s of sampling time and different angular samplings (part 1). Activity is shown as a function of myocardial region. Each colour represents a different simulation. Simulations with 20 angles per detector correspond to blue, green and orange bars, whilst simulations with 200 angles per detector correspond to cyan, yellow and brown bars. Regarding the phase shift: **a** - orange and brown, **b** - green and yellow, and **c** - blue and cyan. The dark blue bar corresponds to the mean activity of the reference image. The error bars correspond to the standard deviation of the activity in each region. Note that only myocardial regions 1 to 6 are shown.

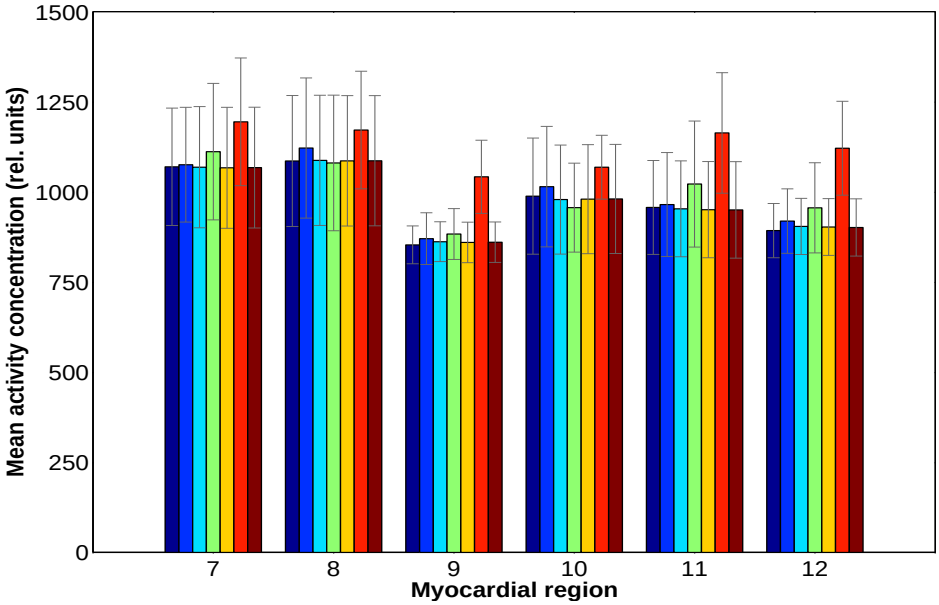

Figure 5.13: Graph of the mean activity for simulations with 2.5s of sampling time and different angular samplings (part 2). Activity is shown as a function of myocardial region. Each colour represents a different simulation. Simulations with 20 angles per detector correspond to blue, green and orange bars, whilst simulations with 200 angles per detector correspond to cyan, yellow and brown bars. Regarding the phase shift: **a** - orange and brown, **b** - green and yellow, and **c** - blue and cyan. The dark blue bar corresponds to the mean activity of the reference image. The error bars correspond to the standard deviation of the activity in each region. Note that only myocardial regions 7 to 12 are shown.

to the standard deviation of the activity in the specified myocardial region.

In relation to the reference image, simulations with 2 seconds of time sampling (Fig. 5.9) show similar mean activity for all myocardial regions. Myocardial regions 5 and 9, which correspond to postero-septal mid-ventricular and basal wall, present slightly lower mean activity when compared to the remaining myocardial regions for all simulations, including the reference image. For simulations with 2.5 seconds of time sampling (Fig. 5.10), the simulation with phase shift **a** presents higher mean activity in relation to the other simulations presented in the graph. Additionally, the mean activity over the twelve regions is more uniform. Note that the simulation with phase shift **c**, which visually presents a good reconstruction (Fig. 5.7), shows mean activity values similar to the reference image. The column chart for simulations with 3 seconds of time sampling (Fig. 5.11) shows results similar to the simulations with 2 seconds of time sampling.

The mean activity in the myocardium for simulations with 2.5 seconds of time sampling and two different angular samplings are shown in Fig. 5.12 and Fig. 5.13. Simulations acquired with 20 angles per detector correspond to blue, green and orange bars, and simulations acquired with 200 angles per detector correspond to cyan, yellow and brown bars. Regarding the simulated phase shift, orange and brown bars correspond to phase shift **a**, green and yellow bars to **b**, and blue and cyan bars to **c**. The dark blue bar corresponds to the reference image, and the error bars to the standard deviation of the activity in the specified myocardial region. This graph indicates that all simulations present similar results, and that for the simulation with an angular sampling of 20 and phase shift **a** there is an over-estimation of the activity. However, the simulation acquired with 200 angles per detector does not present that artefact. Therefore it reinforces the conclusion that for a sufficient large angular sampling, the reconstruction is independent of the phase shift between the respiratory cycle and the acquisition protocol.

Analysing the results presented in Tab. 5.3, in which values of R^2 and NRMSE are shown, it is possible to observe that simulations performed with an angular sampling of 200 angles per detector have the best fit to the reference image - R^2 greater than 0.99 - and the lowest error - NRMSE equal to 3%. In this case, the reconstruction process is independent of the phase shift, whilst for the remaining simulations the results are dependent on the phase shift between acquisition and respiration, and on the time sampling.

Simulations obtained with an angular sampling of 20 angles per detector present a variable fit to the reference image, the value of R^2 ranges from 0.50 to 0.98, and the associated errors are high, as the values of NRMSE range from 7% to 47%. The worst case is that of the simulation obtained with 2.5 seconds per angle and phase shift **a**: the value of R^2 is lower than 0.50, and the value of NRMSE is greater than 45%. This

simulation corresponds to the orange columns in the graph of Fig. 5.12 and Fig. 5.13, which present an over estimation of the mean activity in relation to the reference image. The simulation acquired with phase shift **c** and 2.5 seconds per angle shows good results, with R^2 and NRMSE equal to 0.98 and 7%, respectively, highlighting the issue related to synchronism and sinusoidal respiratory pattern, previously discussed.

Table 5.3: Phase study results. Values of R^2 and NRMSE are shown for each simulation defined by an angular sampling, a time sampling, and a phase shift.

Angular sampling (# angles/detector)	Time sampling (sec/angle)	Phase shift	R^2	NRMSE (%)
20	2.0	a	0.921	12
20	2.0	b	0.936	11
20	2.0	c	0.798	21
20	2.5	a	0.499	47
20	2.5	b	0.889	17
20	2.5	c	0.983	7
20	3.0	a	0.929	11
20	3.0	b	0.712	25
20	3.0	c	0.848	17
200	2.5	a	0.995	3
200	2.5	b	0.996	3
200	2.5	c	0.996	3

5.3.2 Angular sampling study

The reconstructed images of the angular sampling study are shown in Fig. 5.14. These images correspond to simulations obtained with 20, 40 and 120 angles per detector during the acquisition. Based on visual assessment of these images, there is an apparent improvement of the quality of the reconstruction with an increasing number of angles in the detection process. The distribution of activity within the myocardium of the simulation with 120 angles per detector appears to be more uniform and the whole image seems more smooth. Nevertheless it also seems to have a small distortion and lower activity in the posterior wall, according to the VLA view of the myocardium.

The mean activity as a function of myocardial region is shown in the column chart of Fig. 5.15. Each coloured column corresponds to a different acquisition geometry: cyan - 20 angles per detector, yellow - 40 angles per detector, and red - 120 angles per detector. The dark blue column corresponds to the mean activity of the reference image. In general, similar activities are observed in each region of the myocardium, for all simulations. These results suggest that a scan with a smaller number of acquisition angles can be performed without deteriorating the image quality. This is important because it allows the reduction of the scan time.

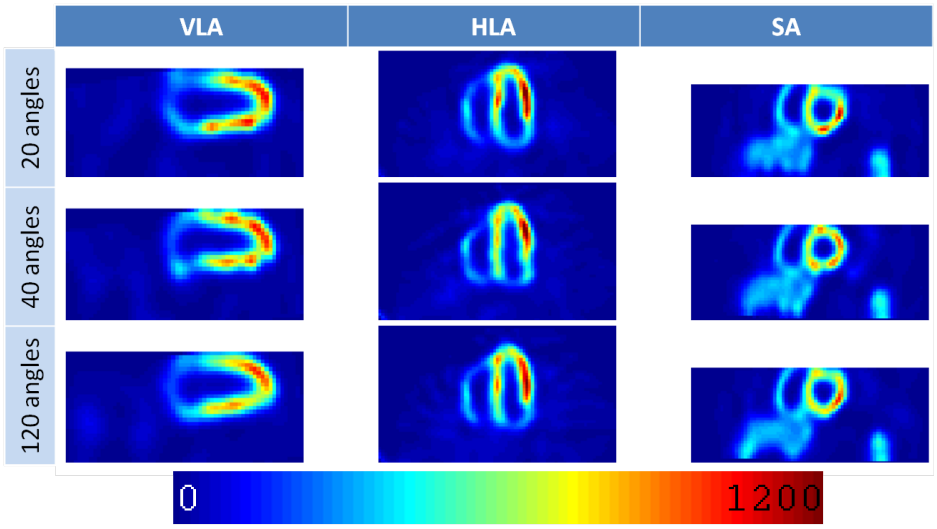

Figure 5.14: Results of the angular sampling study. Myocardial reconstructed images for scans with 20, 40 and 120 angles per detector during the acquisition. On the bottom, the colour scale is shown.

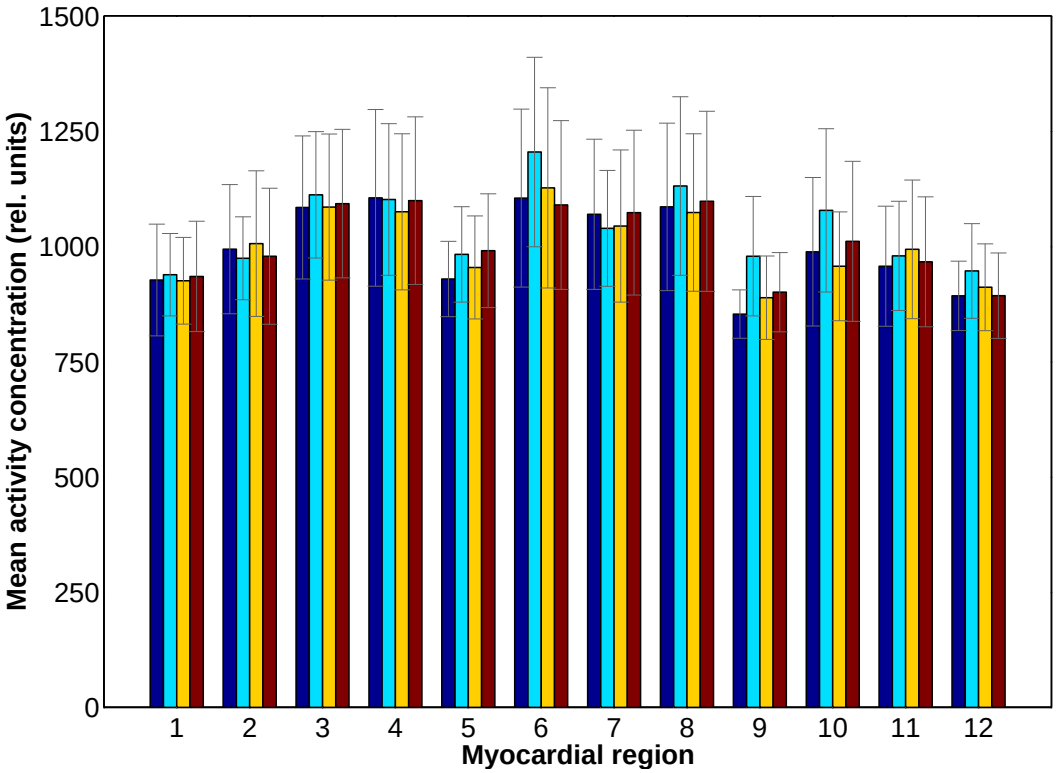

Figure 5.15: Graph of the mean activity for the angular sampling study. Activity is shown as a function of myocardial region. Each coloured bar corresponds to the mean activity of a different simulation: cyan - 20 angles per detector, yellow - 40 angles per detector, and red - 120 angles per detector during the acquisition. The dark blue bar corresponds to the mean activity of the reference image. The error bars correspond to the standard deviation of the activity in the selected region.

The results for the quantitative analysis of the effects of the angular sampling are shown on Tab. 5.4. All simulations present similar results, with a good fit to the reference image - R^2 is greater than 0.9 - and a low error - NRMSE around 10%. Consequently, these results support the conclusion discussed previously.

Table 5.4: Angular sampling study results. Values of R^2 and NRMSE are shown for each simulation defined by an angular sampling.

Angular sampling (# angles/detector)	R^2	NRMSE (%)
20	0.929	11
40	0.965	9
120	0.970	10

5.3.3 Scanning time study

Fig. 5.16 shows reconstructed myocardial images for each simulation of the scanning time study. In the case of shorter-time acquisitions, specially when the scanning time is in the order of magnitude of the duration of one respiratory cycle, reconstructed images present non-uniform activity, distortion of the myocardium's shape, and artefacts in the region outside of the heart boundaries. The most affected regions of the myocardium is the posterior wall and the septum.

As the scan time increases, a gradual improvement of the myocardial activity is observed, as well as a general smoothness of the whole image. Furthermore it is important to highlight that although the quality of the reconstructed myocardium is still very poor with 1-minute scan, a 2-minute scan provides an apparent good reconstruction.

The column chart of Fig. 5.17 and Fig. 5.18 shows the mean activity as a function of myocardial region, for simulations with different scanning times. Each coloured column corresponds to a different simulated time scan: blue - 3 seconds, light blue - 6 seconds, cyan - 12 seconds, yellow - 24 seconds, orange - 41 seconds, red - 1 minute, and brown - 2 minutes. The dark blue bar corresponds to the mean activity of the reference image, and the error bars to the standard deviation of the activity in the specified myocardial region. For each myocardial region, the mean activity shows no significant differences for almost all simulations. However it is important to point out that the simulation with a scanning time of 2 minutes have mean activity values closer to the reference image, when compared to the remaining simulations.

The quantitative analysis results of the scanning time study are presented in Tab. 5.5. According to these results, the simulations with the highest values of NRMSE are the ones obtained with short time acquisitions. Regarding the values of R^2, they are very similar for all simulations, except for the simulation acquired with 41 seconds of scan

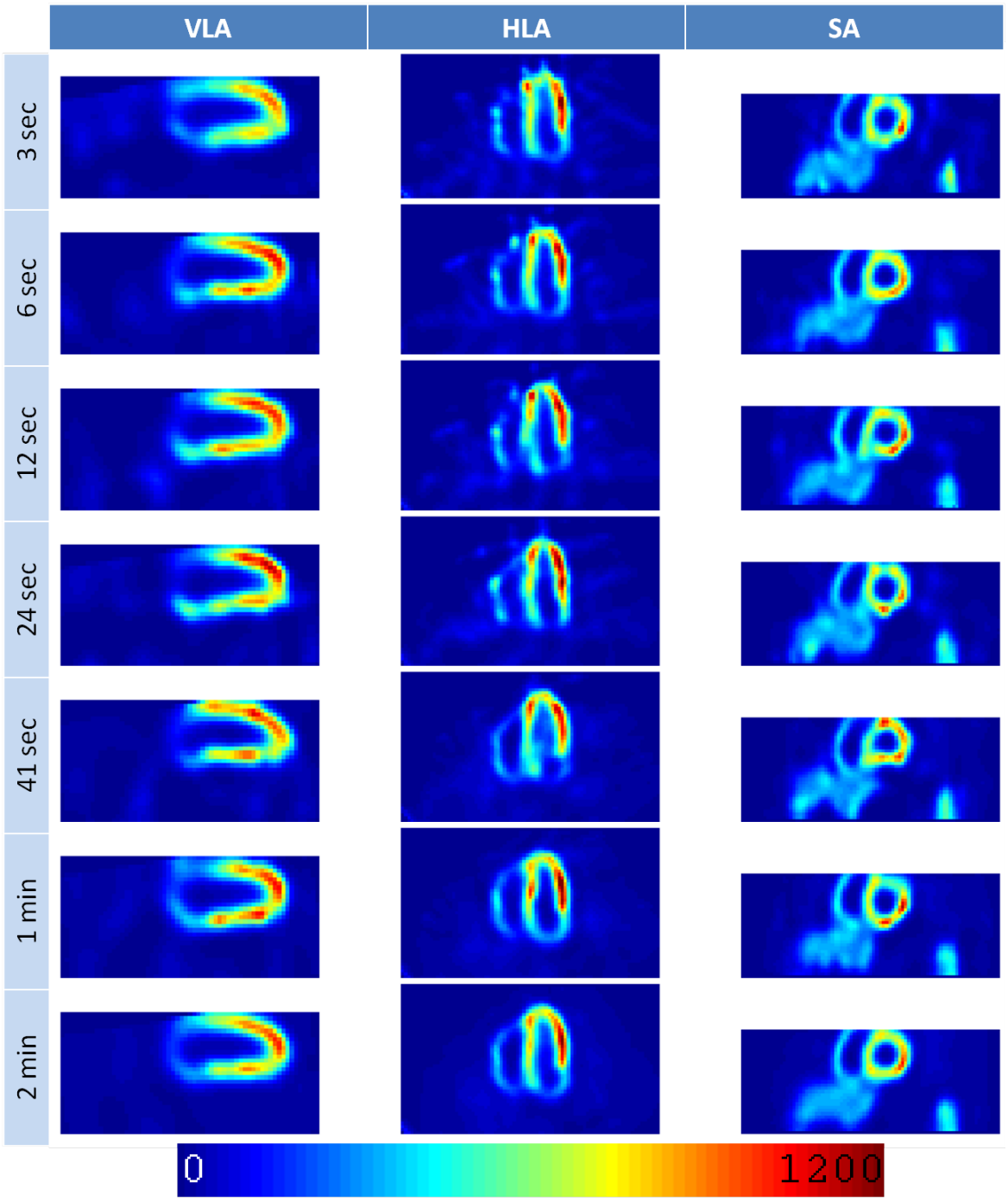

Figure 5.16: Results of the scanning time study. Myocardial reconstructed images simulated with different scanning times: 3, 6, 12, 24 and 41 seconds, and 1 and 2 minutes. On the bottom, the colour scale is shown.

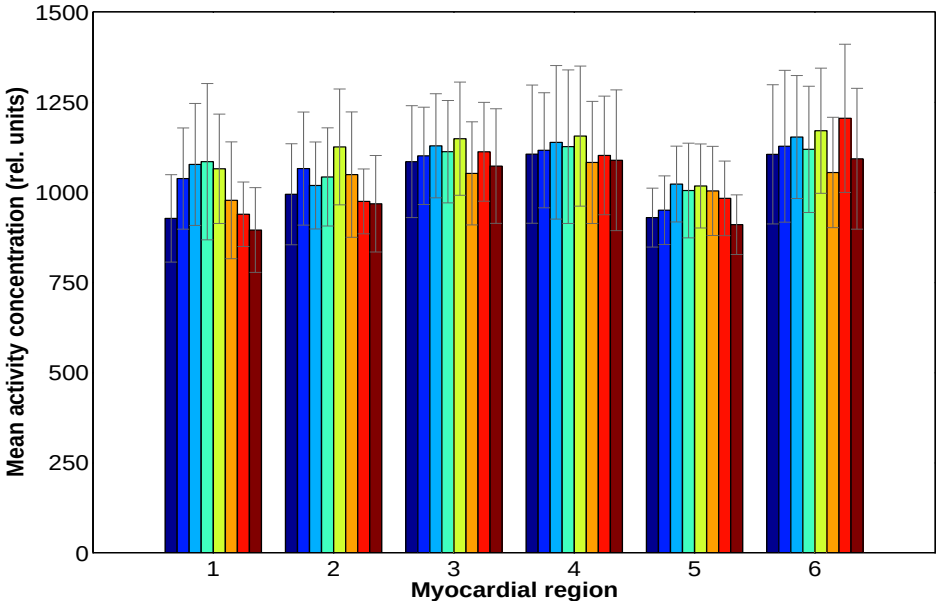

Figure 5.17: Graph of the mean activity for the study of the scanning time (part 1). Activity is shown as a function of myocardial region. Each coloured bar corresponds to a different simulation: blue - 3 seconds, light blue - 6 seconds, cyan - 12 seconds, yellow - 24 seconds, orange - 41 seconds, red - 1 minute, and brown - 2 minutes. The dark blue bar corresponds to the mean activity of the reference image. The error bars correspond to the standard deviation of the activity in the selected region. Note that only myocardial regions 1 to 6 are shown.

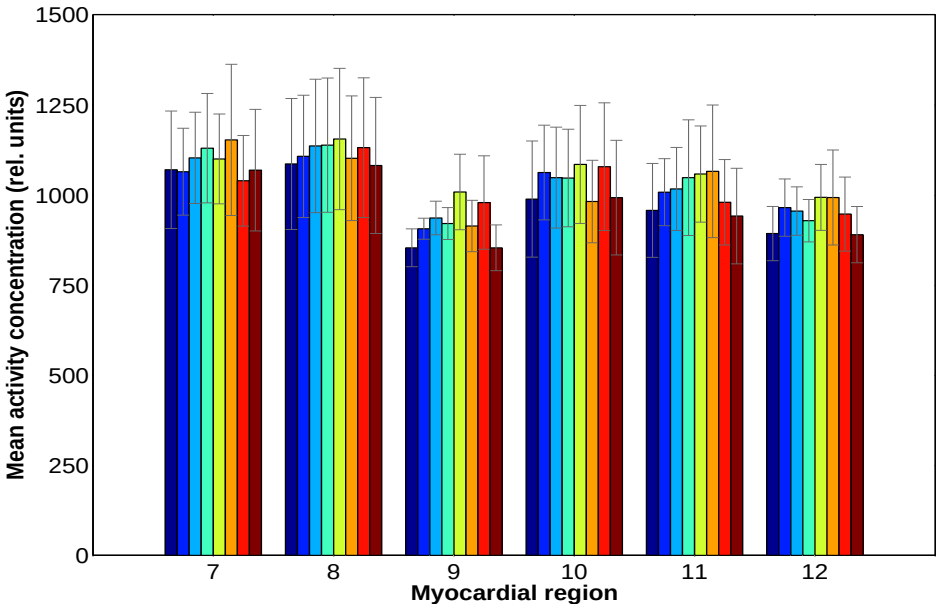

Figure 5.18: Graph of the mean activity for the study of the scanning time (part 2). Activity is shown as a function of myocardial region. Each coloured bar corresponds to a different simulation: blue - 3 seconds, light blue - 6 seconds, cyan - 12 seconds, yellow - 24 seconds, orange - 41 seconds, red - 1 minute, and brown - 2 minutes. The dark blue bar corresponds to the mean activity of the reference image. The error bars correspond to the standard deviation of the activity in the selected region. Note that only myocardial regions 7 to 12 are shown.

time. In general, there are clear differences in many regions for all scans except for the 2-minute one, as observed in the reconstructed images (Fig. 5.16) and the column chart (Fig. 5.17 and Fig. 5.18). One important aspect of these results is that, although the simulation acquired for 1 minute has a poor reconstruction (NRMSE is 11%), the simulation acquired for 2 minutes has a low error (NRMSE is 6%).

Table 5.5: Scanning time study results. Values of R^2 and NRMSE are shown for each simulation defined by a scanning time.

Scanning time (sec)	R^2	NRMSE (%)
3	0.932	20
6	0.929	23
12	0.904	24
24	0.937	31
41	0.798	21
60	0.929	11
120	0.992	6

5.3.4 Respiratory cycle pattern study

The reconstructed images for the study of the effects of the respiratory cycle pattern with short time acquisitions are shown in Fig. 5.19. Four simulations were performed for each type of respiratory cycle: sinusoidal and extended end-of-exhale. The reconstructed images show that a slightly more realistic respiratory cycle pattern - extended end-of-exhale - introduces higher variability in the distribution of activity within the myocardium, and distortion of its shape. Simulations with a sinusoidal breathing pattern present reconstruction artefacts mostly in the septum and posterior wall. In addition, reconstructed images simulated with an extended end-of-exhale breathing pattern show also some perturbations and irregularities on the posterior and lateral walls of the heart.

The column graphs of Fig. 5.20, Fig. 5.21, Fig. 5.22, and Fig. 5.23 show the mean activity as a function of myocardial region for simulations obtained with a 3-second scan, 6-second scan, 12-second scan, and 24-second scan, respectively. The green column corresponds to the simulation performed with a sinusoidal breathing pattern, whilst the red one corresponds to the simulation acquired with an extended end-of-exhale pattern. The dark blue column corresponds to the mean activity of the reference image, and the error bars to the standard deviation of the activity in the specified myocardial region. Simulations performed with scans of 3 seconds (Fig. 5.20) show a more consistent variation of the mean activity within the myocardium in relation to the other simulations. Simulations performed with scans of 24 seconds (Fig. 5.23) present higher mean activity when compared to the reference image. Regarding the breathing pattern, there are

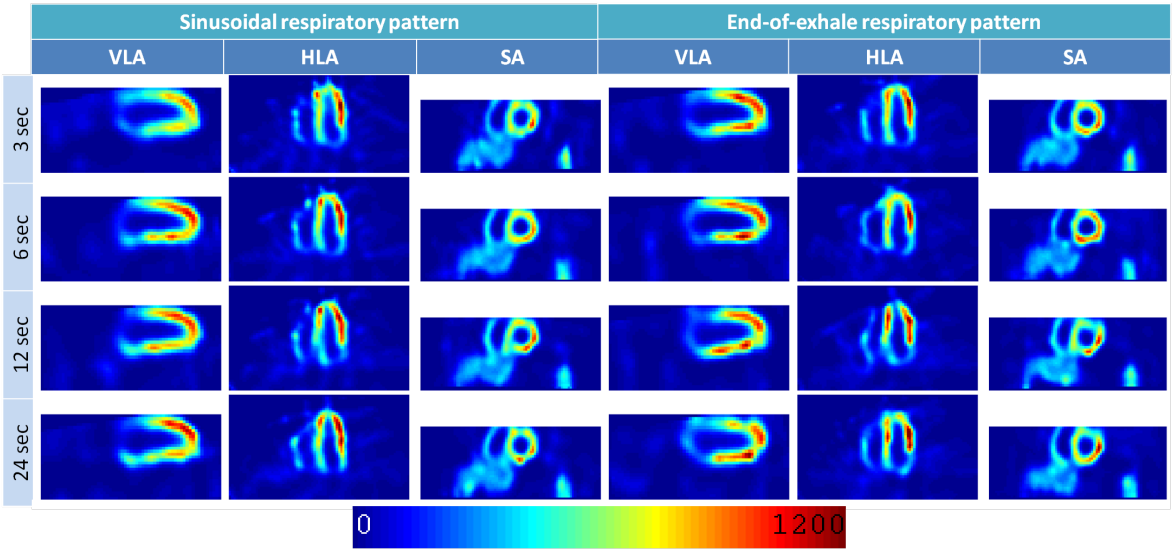

Figure 5.19: Results for the study of the respiratory cycle pattern. Myocardial reconstructed images acquired with four different scanning times - 3, 6, 12 and 24 seconds -, and simulated with a sinusoidal and an extended end-of-exhale breathing pattern. On the bottom, the colour scale is shown.

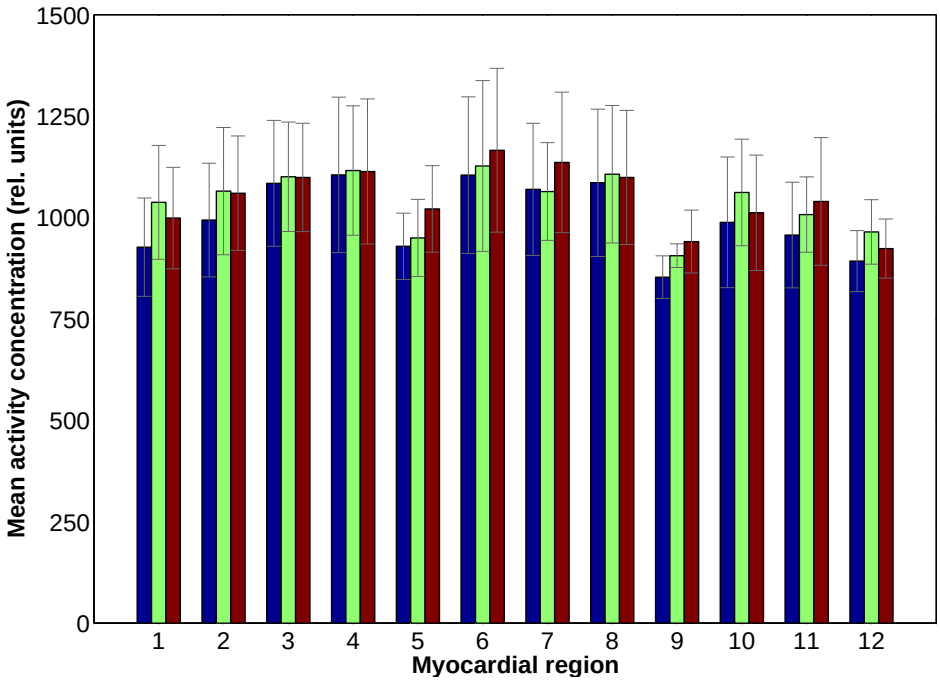

Figure 5.20: Graph of the relative mean activity for simulations with a 3-second scan. The green bar corresponds to the simulation performed with a sinusoidal respiratory pattern, while the red bar corresponds to an extended end-of-exhale pattern. The dark blue bar corresponds to mean activity of the reference image. The error bars correspond to the standard deviation of the activity in each region.

no significant differences between mean activities of these simulations. Therefore it is difficult to draw a conclusion.

The values of R^2 and NRMSE presented on Tab. 5.6 indicate that all simulations have poor results. The values of NRMSE range approximately from 20% and 30%

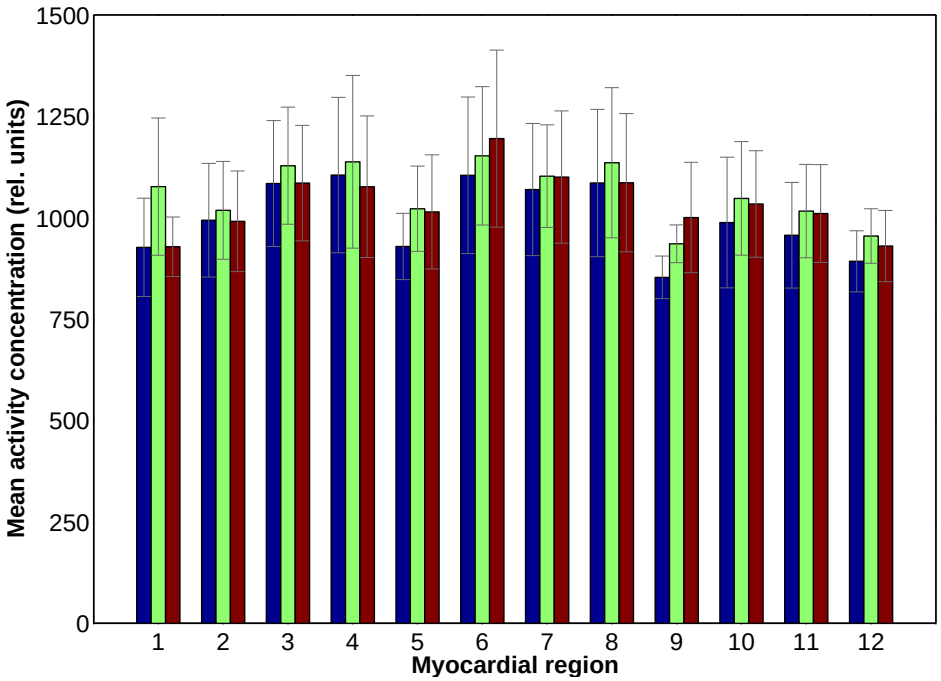

Figure 5.21: Graph of the mean activity for simulations with a 6-second scan. The green bar corresponds to the simulation performed with a sinusoidal respiratory pattern, while the red bar corresponds to an extended end-of-exhale pattern. The dark blue bar corresponds to mean activity of the reference image. The error bars correspond to the standard deviation of the activity in each region.

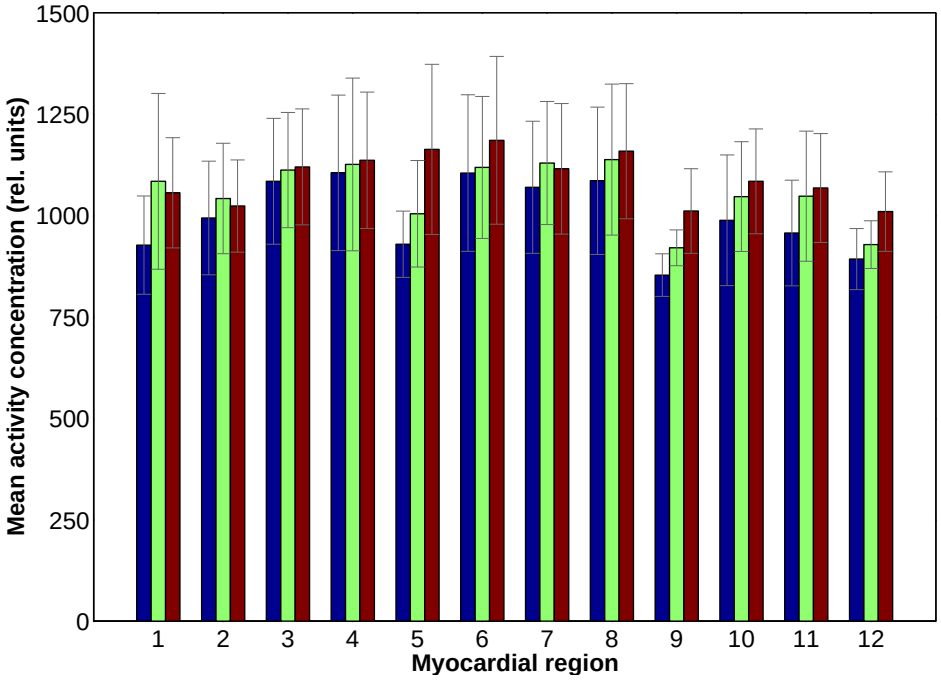

Figure 5.22: Graph of the mean activity for simulations with a 12-second scan. The green bar corresponds to the simulation performed with a sinusoidal respiratory pattern, while the red bar corresponds to an extended end-of-exhale pattern. The dark blue bar corresponds to mean activity of the reference image. The error bars correspond to the standard deviation of the activity in each region.

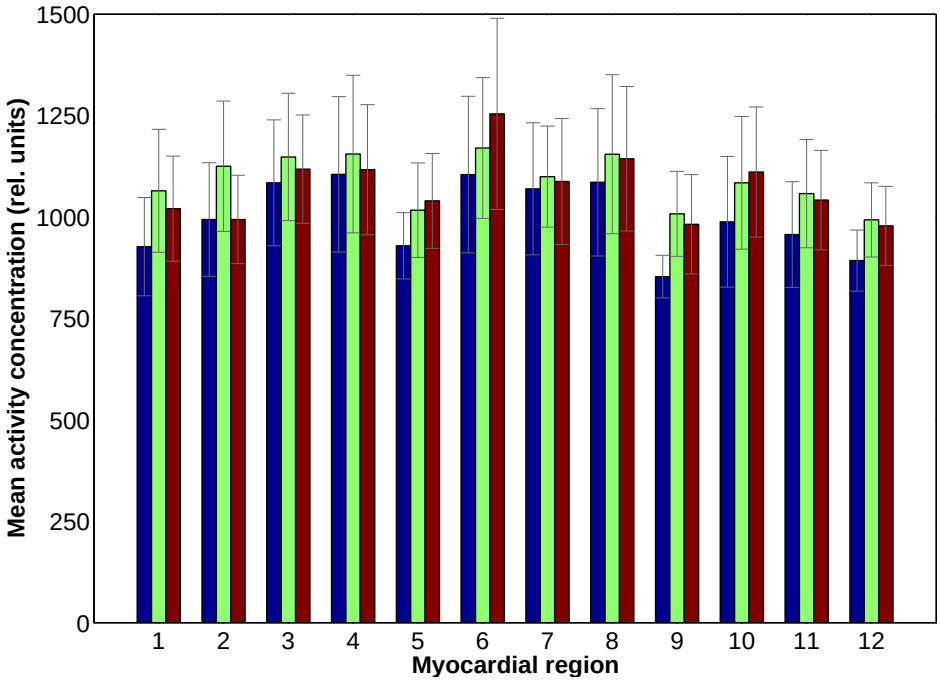

Figure 5.23: Graph of the mean activity for simulations with a 24-second scan. The green bar corresponds to the simulation performed with a sinusoidal respiratory pattern, while the red bar corresponds to an extended end-of-exhale pattern. The dark blue bar corresponds to mean activity of the reference image. The error bars correspond to the standard deviation of the activity in each region.

and they show no significant differences between the two types of breathing pattern. Regarding the values of R^2, a best fit to the reference image is observed for images simulated with a sinusoidal respiratory cycle pattern. The worst simulation is the one obtained with a scanning time of 24 seconds and an extended end-of-exhale respiratory pattern. This conclusion is supported by the respective reconstructed image presented in Fig. 5.19.

Table 5.6: Respiratory cycle pattern study results. Values of R^2 and NRMSE are shown for each simulation defined by a scanning time and a respiratory cycle pattern.

Scanning time (sec)	Respiratory cycle pattern	R^2	NRMSE (%)
3	sinusoidal	0.932	20
3	extended end-of-exhale	0.940	19
6	sinusoidal	0.929	23
6	extended end-of-exhale	0.827	18
12	sinusoidal	0.904	24
12	extended end-of-exhale	0.734	33
24	sinusoidal	0.937	31
24	extended end-of-exhale	0.831	22

5.4 Conclusion

The effects of respiratory motion in myocardial SPECT images are unavoidable due to the duration of the exam. However, as the D-SPECT camera has a different acquisition geometry when compared to a standard SPECT camera, an image can be obtained with a faster scan, or with less number of acquired angles, reducing the acquisition time. Therefore the aim of this study was to investigate critical acquisition parameters and the effects of respiratory motion that could lead to the introduction of artefacts in the reconstructed images.

For acquisition times in the order of minutes, artefacts are introduced in the reconstructed images, but they are not severe. In addition, for a 2-minute scan, the reconstructed image presents good quality. Nevertheless, as the scan time is reduced to the order of seconds, the respiratory cycle contributes for a rapid change of the heart's position in relation to the detectors. As shown in the results, breathing interferes with the reconstruction process for shorter acquisition times, affecting the accuracy and quality of the reconstructed myocardial images. In summary, with longer acquisitions, the myocardial activity is more averaged during the acquisition process, while shorter acquisitions result in reconstructed images with more artefacts and distortion.

Moreover, the phase shift between the acquisition process and the respiratory cycle is also an issue that can lead to artefacts in the reconstructed images. Results showed that acquisitions with a sufficient large number of acquired angles, the phase shift is not an issue. On the other hand, the phase shift compromises the accuracy of the activity estimation with an angular sampling of 20 angles per detector. However, in a perfect scenario in which the respiratory cycle has a sinusoidal pattern, the time sampling is half the duration of the respiratory cycle, and the acquisition starts with the heart in the position of full exhalation, it is possible to improve the distribution of activity within the myocardium. This suggests that a respiratory gating could be applied to improve results.

Regarding the angular sampling parameter, no significant differences were shown for simulated images with three different angular samplings. Consequently this suggests that the time scan can be reduced without quality-loss for the acquired image.

Furthermore, the pattern of the respiratory cycle can also affect the reconstruction process. This is an important parameter because there is inter- and intra-patient variability, for example it varies if the patient is under stress or relaxed. The presented results indicate that a more regular breathing pattern contributes for a better reconstruction, suggesting that breathing training and a relaxed state of the patient could be helpful in order to obtain better myocardial images. However, it would be advantageous to perform a larger number of simulations to confirm this effect.

Chapter 6

Conclusions

6.1 Summary

This dissertation has evaluated a novel cardiac-dedicated SPECT system: the D-SPECT system. It comprises 9 collimated CZT detectors, mounted vertically in a curved configuration that conforms to the left side of the patient torso. Each detector is able to rotate independently, allowing for the selection of different scanning patterns. The fast sampling yields reduced scanning times or radiation exposure.

However, the novel design and acquisition geometry results in limited and patient-specific spatial acquisition. Therefore unexpected time-related effects may occur, deteriorating projection data and consequently reconstructed images of the heart.

The purpose of this study was therefore to investigate critical acquisition parameters of the D-SPECT system, that could lead to artefacts in the reconstructed images. In particular, geometry-related issues and effects of respiratory motion.

6.2 Contribution

The study related to geometry-related issues has found that the uniformity and shape of the reconstructed myocardium are affected by the LV-detector distance and attenuation. With attenuation, activity decreases with distance, specially for distances in which the myocardium is almost outside the FOV. Whereas without attenuation, the distribution of activity within the reconstructed myocardium improves, showing that the effects of attenuation could be solved applying attenuation correction. But for large LV-detector distances, activity drops, showing that the geometry of the acquisition can also affect the reconstructed image.

These findings show the importance of patient positioning, and the development and improvement of attenuation correction algorithms, in order to correct for attenuation artefacts, which may interfere with clinical diagnosis.

However, this study presents some limitations. Neither noise nor scatter were

modelled in the simulations, and these issues would contribute to a poorer image quality. Another issue to bear in mind is that the whole phantom is displaced to simulate different LV-detector distances, instead of displacing only the heart. Therefore the fact that activity decreases with distance when attenuation is present could be due to a different attenuation pattern, since the photons would travel along different paths through the body to reach the detectors.

Regarding the effects of respiratory motion, the results of this second investigation showed that parameters such as the scanning time, the angular sampling, the breathing pattern, and the phase shift between the acquisition and the respiratory cycle affect the reconstructed images of the heart.

One major finding was that the angular sampling can be reduced, without compromising the reconstructed image of the myocardium. However, for short acquisition times, specially those in the order of the duration of the respiratory cycle, more artefacts are included, affecting the reconstructed image. Hence there is a compromise between acquisition time and quality of the reconstructed image.

Furthermore, results showed that improved images can be obtained combining a good synchronism between the acquisition and the respiratory cycle with a regular breathing pattern. This suggests that a respiratory gating and/or breathing training could be applied to improve SPECT quantification.

One major limitation to this study is the number of simulations performed to analyse each parameter, which is small. Another problem is related to the fact that cardiac contraction is not simulated, which in a real acquisition is always present. However, the issue of cardiac motion can be addressed using gating. In addition, as pointed out previously, scatter and noise were also not modelled in this study.

As a result of the carried investigation, contributions were made to the scientific community, aimed at a better understanding of the system operation.

A poster was accepted to the Workshop on Biomedical Engineering (WBME) 2012, which took place at FCUL, Lisbon, Portugal, entitled:

Evaluation of the D-SPECT System Using a Simulator

Filipa Costa[123], Débora Salvado[123], Elizabeth Howell[2], Kjell Erlandsson[2], Pedro Almeida[3], Brian F. Hutton[2]

[1]*FCUL, Lisbon, Portugal.*

[2]*INM, UCL, London, UK.*

[3]*IBEB, FCUL, Lisbon, Portugal.*

Organised by Biomedical Engineering and Biophysics students and professors, the WBME aims to present scientific work in the different areas of Biomedical Engineering, inviting both national and international speakers.

In addition, an abstract for oral presentation was accepted to the 40th British Nuclear Medicine Society (BNMS) meeting at the International Harrogate Centre, Harrogate, UK, entitled:

Evaluation of D-SPECT Acquisition Geometry Using a Simulator
Filipa Costa[123], Débora Salvado[123], Elizabeth Howell[2], Kjell Erlandsson[2], Pedro Almeida[3], Brian F. Hutton[2]
[1]*FCUL, Lisbon, Portugal.*
[2]*INM, UCL, London, UK.*
[3]*IBEB, FCUL, Lisbon, Portugal.*

The BNMS is an organisation concerned with the clinical practice, education, research and development of Nuclear Medicine within the UK.

6.3 Future Work

It is recommended that further research be undertaken. More broadly, a large number of simulations could provide more definitive evidence for the obtained conclusions, specially for the study regarding the effects of respiratory motion. Additionally, it would be valuable to compare the experiments simulated in this thesis work with the results obtained with a physical phantom.

Furthermore, in the study related to the acquisition geometry, modifications to the D-SPECT *Simulator* should be implemented to simulate scatter, and the dead time of the detectors due to rotation. Further research might also explore the effects of scanning patients with different sizes.

For the respiratory motion investigation, it would be interesting to further assess the effects of different realistic breathing patterns, and cardiac contraction. Also, more information on re-programming detectors would help establish new scanning procedures.

At last, together, this information could be used to improve clinical protocols, and diagnosis accuracy, towards a better patient healthcare.

6.4 Concluding Remarks

The study of this thesis focused in the evaluation of a new cardiac-dedicated system only available in a few countries worldwide: the D-SPECT system. Due to its novel design and scanning geometry, unexpected time-related effects may occur, and may lead to artefacts in the myocardial reconstructed images. These artefacts can be interpreted as perfusion defects, compromising cardiac assessment.

Effects of the acquisition geometry, attenuation, and respiratory motion were assessed, using a simulation tool to obtain myocardial images. Results demonstrated the importance of patient positioning, and development of attenuation correction algorithms,

in order to obtain good-quality images. Furthermore, they showed the compromise between reduced acquisition times and accurate reconstructed images, and suggested that a respiratory gating and/or breathing training could be applied to improve results.

Although these issues have been the focus of several research work for standard SPECT systems, there are no similar studies for the D-SPECT. Consequently further research in this area would be advisable. In any case, this study provides significant findings related to the D-SPECT system operation, and suggests that clinical protocols and diagnoses can be improved, for the benefit of both the healthcare provider, and the patient.

Bibliography

[1] M. Groch and W. Erwin, "Single-photon emission computed tomography in the year 2001: instrumentation and quality control," *Journal of Nuclear Medicine Technology*, vol. 29, no. 1, pp. 12–18, 2001. [Online]. Available: http://tech.snmjournals.org/content/29/1/12.full

[2] P. Slomka, J. Patton, D. Berman, and G. Germano, "Advances in technical aspects of myocardial perfusion SPECT imaging," *Journal of Nuclear Cardiology*, vol. 16, no. 2, pp. 255–276, 2009.

[3] G. Gullberg, B. Reutter, A. Sitek, J. Maltz, and T. Budinger, "Dynamic single photon emission computed tomography - basic principles and cardiac applications," *Physics in Medicine and Biology*, vol. 55, no. 20, pp. 111–191, 2010. [Online]. Available: http://iopscience.iop.org/0031-9155/55/20/R01/pdf/0031-9155_55_20_R01.pdf

[4] A. Baggish and C. Boucher, "Radiopharmaceutical agents for myocardial perfusion imaging," *Circulation*, vol. 118, no. 16, pp. 1668–1674, 2008. [Online]. Available: http://circ.ahajournals.org/content/118/16/1668.full

[5] G. Zeng, J. Galt, M. Wernick, R. Mintzer, and J. Aarsvold, *Emission Tomography: Fundamentals of PET and SPECT*. Elsevier Academic Press, 2004, vol. 23, ch. 7 "Single Photon Emission Computed Tomography", pp. 127–152. [Online]. Available: http://www.scribd.com/doc/28417300/emission-tomography-the-fundamentals-of-PET-and-SPECT

[6] P. Sharp and K. Goatman, *Practical Nuclear Medicine*, 3rd ed. Springer, 2005, ch. 1 "Nuclear Medicine Imaging", pp. 1–20.

[7] M. Madsen, *Biomedical Engineering and Design Handbook*, 2nd ed. McGraw-Hill, 2009, ch. 11 "Nuclear Medicine Imaging Instrumentation", pp. 317–346.

[8] M. Wernick and J. Aarsvold, *Emission Tomography: Fundamentals of PET and SPECT*. Elsevier Academic Press, 2004, ch. 2 "Introduction to Emission

Tomography", pp. 11–24. [Online]. Available: http://www.scribd.com/doc/28417300/emission-tomography-the-fundamentals-of-PET-and-SPECT

[9] M. Khalil, *Basic Sciences of Nuclear Medicine*, 1st ed. Springer, 2011, ch. 13 "Emission Tomography and Image Reconstruction", pp. 259–283. [Online]. Available: http://www.pic.iran-forum.ir/images/3vlrgya9p425zgt89i.pdf

[10] L. Shepp and Y. Vardi, "Maximum likelihood reconstruction for emission tomography," *IEEE Transactions on Medical Imaging*, vol. 1, no. 2, pp. 113–122, 1982. [Online]. Available: http://www-stat.wharton.upenn.edu/~shepp/publications/58.pdf

[11] D. Lalush and M. Wernick, *Emission Tomography: Fundamentals of PET and SPECT*. Elsevier Academic Press, 2004, ch. 21 "Iterative image reconstruction", pp. 421–441. [Online]. Available: http://www.scribd.com/doc/28417300/emission-tomography-the-fundamentals-of-PET-and-SPECT

[12] P. P. Bruyant, "Analytic and Iterative Reconstruction Algorithms in SPECT," *Journal of Nuclear Medicine*, vol. 43, no. 10, pp. 1343–1358, 2002. [Online]. Available: http://jnm.snmjournals.org/content/43/10/1343.full.pdf+html

[13] B. Hutton, H. Hudson, and F. Beekman, "A clinical perspective of accelerated statistical reconstruction," *European Journal of Nuclear Medicine*, vol. 24, no. 7, pp. 797–808, 1997.

[14] M. King, S. Glick, P. Pretorius, R. Wells, H. Gifford, M. Narayanan, and T. Farncombe, *Emission Tomography: Fundamentals of PET and SPECT*. Elsevier Academic Press, 2004, ch. 22 "Attenuation, Scatter, and Spatial Resolution Compensation in SPECT", pp. 473–477. [Online]. Available: http://www.scribd.com/doc/28417300/emission-tomography-the-fundamentals-of-PET-and-SPECT

[15] S. Gambhir, D. Berman, J. Ziffer, M. Nagler, M. Sandler, J. Patton, B. Hutton, T. Sharir, S. Ben-Haim, and S. Ben-Haim, "A novel high-sensitivity rapid-acquisition single-photon cardiac imaging camera," *Journal of Nuclear Medicine*, vol. 50, no. 4, pp. 635–643, 2009. [Online]. Available: http://jnm.snmjournals.org/content/50/4/635.full.pdf+html

[16] E. Garcia, T. Faber, and F. Esteves, "Cardiac dedicated ultrafast SPECT cameras: new designs and clinical implications," *Journal of Nuclear Medicine*, vol. 52, no. 2, pp. 210–217, 2011. [Online]. Available: http://jnm.snmjournals.org/content/52/2/210.full.pdf

[17] "About Spectrum," Spectrum Dynamics Ltd, 2008. [Online]. Available: http://www.spectrum-dynamics.com/about/sites.html

[18] K. Erlandsson, K. Kacperski, D. VanGramberg, and B. Hutton, "Performance evaluation of D-SPECT: a novel SPECT system for nuclear cardiology," *Physics in Medicine and Biology*, vol. 54, no. 9, pp. 2635–2649, 2009.

[19] T. Sharir, S. Ben-Haim, K. Merzon, V. Prochorov, D. Dickman, S. Ben-Haim, and D. Berman, "High-speed myocardial perfusion imaging initial clinical comparison with conventional dual detector anger camera imaging," *Journal of the American College of Cardiology Imaging*, vol. 1, no. 2, pp. 156–163, 2008. [Online]. Available: http://imaging.onlinejacc.org/article.aspx?articleid=1109242

[20] "D-SPECT Cardiac Scanner," medGadget, 2005. [Online]. Available: http://medgadget.com/2005/12/dspect_cardiac.html

[21] H. Zaidi and B. Hasegawa, *Quantitative Analysis in Nuclear Medicine Imaging*. Springer, 2006, ch. 1 "Overview of Nuclear Medical Imaging: Physics and Instrumentation", pp. 1–34. [Online]. Available: http://www.almhnds.com/7/NM/5.pdf

[22] M. Khalil, *Basic Sciences of Nuclear Medicine*, 1st ed. Springer, 2011, ch. 10 "Elements of Gamma Camera and SPECT Systems", pp. 155–178. [Online]. Available: http://www.pic.iran-forum.ir/images/3vlrgya9p425zgt89i.pdf

[23] G. Germano, "Technical aspects of myocardial SPECT imaging," *Journal of Nuclear Medicine*, vol. 42, no. 10, pp. 1499–1507, 2001. [Online]. Available: http://jnm.snmjournals.org/content/42/10/1499.full.pdf

[24] M. Ljungberg, *Basic Sciences of Nuclear Medicine*, 1st ed. Springer, 2011, ch. 14 "Quantitative SPECT Imaging", pp. 285–309. [Online]. Available: http://www.pic.iran-forum.ir/images/3vlrgya9p425zgt89i.pdf

[25] H. Gemmell and R. Staff, *Practical Nuclear Medicine*, 3rd ed. Springer, 2005, ch. 2 "Single Photon Emission Computed Tomography (SPECT)", pp. 21–34.

[26] J. Nuyts, *Nuclear Medicine Technology and Techniques*, 2011, vol. 16, no. 5. [Online]. Available: ftp://134.58.179.7/pub/nuyts/cursus/cursus_nucleo.pdf

[27] R. Seeley, T. Stephens, and P. Tate, *Anatomy and Physiology*, 6th ed. The McGraw-Hill Companies, 2004, ch. 20 "Cardiovascular System: The Heart", pp. 667–709. [Online]. Available: http://www.blogsua.com/pdf/20CardiovascularSystemTheHeart.pdf

[28] "Coronary heart disease statistics in England," British Heart Foundation, 2012. [Online]. Available: http://www.bhf.org.uk

[29] "Coronary Heart Disease," HealthKnowledge, 2006. [Online]. Available: http://www.healthknowledge.org.uk

[30] "Risk Factors for CHD," Heart UK, 2007. [Online]. Available: http://www.heartuk.org.uk

[31] "What is Coronary Heart Disease?" National Heart Lung and Blood Institute, NIH, 2011. [Online]. Available: http://www.nhlbi.nih.gov/health/health-topics/topics/cad/

[32] "Coronary Artery Disease," Beth Israel Deaconess Medical Center, 2012. [Online]. Available: http://www.bidmc.org/CentersandDepartments/Departments/Medicine/Divisions/CardiovascularMedicine/DiseasesandConditions/CoronaryArteryDisease.aspx

[33] M. Henzlova, M. Cerqueira, J. Mahmarian, and S. Yao, "Stress protocols and tracers," *Journal of Nuclear Cardiology*, vol. 13, no. 6, pp. 80–90, 2006.

[34] C. Hansen, R. Goldstein, O. Akinboboye, D. Berman, E. Botvinick, K. Churchwell, C. Cooke, J. Corbett, S. Cullom, S. Dahlberg, R. Druz, E. Ficaro, J. Galt, R. Garg, G. Germano, G. Heller, M. Henzlova, M. Hyun, L. Johnson, A. Mann, B. McCallister, R. Quaife, T. Ruddy, S. Sundaram, R. Taillefer, R. Ward, and J. Mahmarian, "Myocardial perfusion and function: single photon emission computed tomography," *Journal of Nuclear Cardiology*, vol. 14, no. 6, pp. 39–60, 2007.

[35] G. Germano, P. Kavanagh, H. Kiat, K. VanTrain, and D. Berman, "Temporal image fractionation: rejection of motion artifacts in myocardial SPECT," *Journal of Nuclear Medicine*, vol. 35, no. 7, pp. 1193–7, 1994. [Online]. Available: http://jnm.snmjournals.org/content/35/7/1193.full.pdf

[36] G. Germano, H. Kiat, P. Kavanagh, M. Moriel, M. Mazzanti, H. Su, K. VanTrain, and D. Berman, "Automatic quantification of ejection fraction from gated myocardial perfusion SPECT," *Journal of Nuclear Medicine*, vol. 36, no. 11, pp. 2138–47, 1995. [Online]. Available: http://jnm.snmjournals.org/content/36/11/2138.full.pdf+html

[37] R. Seeley, T. Stephens, and P. Tate, *Anatomy and Physiology*, 6th ed. The McGraw-Hill Companies, 2004, ch. 23 "Respiratory System", pp. 813–58. [Online]. Available: http://www.blogsua.com/pdf/23RespiratorySystem.pdf

[38] P. Keall, G. Mageras, J. Balter, R. Emery, K. Forster, S. Jiang, J. Kapatoes, D. Low, M. Murphy, B. Murray, C. Ramsey, M. VanHerk, S. Vedam, J. Wong, and E. Yorke, "The management of respiratory motion in radiation oncology report of AAPM Task Group 76," *Medical Physics*, vol. 33, no. 10, p. 3874, 2006. [Online]. Available: http://aapm.net/pubs/reports/RPT_91MPSynopsis.pdf

[39] H. Gray, *Gray's Anatomy of the Human Body*, 20th ed. Philadelphia: Lea & Febiger, 2000, ch. IV6c "The Muscles of the Thorax".

[40] L. Cerviño, J. Du, and S. Jiang, "MRI-guided tumor tracking in lung cancer radiotherapy," *Physics in Medicine and Biology*, vol. 56, no. 13, pp. 3773–85, 2011. [Online]. Available: http://iopscience.iop.org/0031-9155/56/13/003/pdf/0031-9155_56_13_003.pdf

[41] S. Davies, L. Hill, R. Holmes, M. Halliwell, and P. Jackson, "Ultrasound quantitation of respiratory organ motion in the upper abdomen," *The British Journal of Radiology*, vol. 67, no. 803, pp. 1096–102, 1994.

[42] P. Danias, M. Stuber, R. Botnar, K. Kissinger, R. Edelman, and W. Manning, "Relationship between Motion of Coronary Arteries and Diaphragm During Free Breathing: Lessons from Real-Time MR Imaging," *American Roentgen Ray Society*, vol. 172, pp. 1061–1065, 1999.

[43] K. Nehrke, P. Bornert, D. Manke, and J. C. Bock, "Free-breathing Cardiac MR Imaging: Study of Implications of Respiratory Motion - Initial Results," *Radiology*, vol. 220, no. 3, pp. 810–15, 2001. [Online]. Available: http://radiology.rsna.org/content/220/3/810.full.pdf+html

[44] J. Keegan, P. Gatehouse, G. Yang, and D. Firmin, "Coronary Artery Motion With the Respiratory Cycle During Breath-Holding and Free-Breathing: Implications for Slice-Followed Coronary Artery Imaging," *Magnetic Resonance in Medicine*, vol. 47, pp. 476–481, 2002. [Online]. Available: http://www.rbh-cmr.org/pubpdfs/Flow/5.pdf

[45] G. Shechter, C. Ozturk, J. Resar, and E. McVeigh, "Respiratory motion of the heart from free breathing coronary angiograms," *IEEE Transactions on Medical Imaging*, vol. 23, no. 8, pp. 1046–56, 2004.

[46] K. McLeish, D. Hill, D. Atkinson, J. Blackall, and R. Razavi, "A study of the motion and deformation of the heart due to respiration," *IEEE Transactions on Medical Imaging*, vol. 21, no. 9, pp. 1142–50, 2002. [Online]. Available: http://cds.ismrm.org/ismrm-2002/PDF6/1633.PDF

[47] J. Cooper, P. Neumann, and B. K. McCandless, "Effect of patient motion on tomographic myocardial perfusion imaging," *Journal of Nuclear Medicine*, vol. 33, no. 8, pp. 1566–71, 1992. [Online]. Available: http://jnm.snmjournals.org/content/33/8/1566.short

[48] E. Botvinick, Y. Zhu, W. O'Connell, and M. Dae, "A quantitative assessment of patient motion and its effect on myocardial perfusion SPECT images." *Journal of Nuclear Medicine*, vol. 34, no. 2, pp. 303–10, 1993. [Online]. Available: http://jnm.snmjournals.org/content/34/2/303.full.pdf

[49] J. Parker, "Effect of Motion on Cardiac SPECT Imaging," *Journal of Nuclear Medicine*, vol. 34, no. 8, pp. 1355–1356, 1993.

[50] J. Wheat and G. Currie, "Incidence and characterization of patient motion in myocardial perfusion SPECT: Part 1," *Journal of Nuclear Medicine Technology*, vol. 32, no. 2, pp. 60–5, 2004. [Online]. Available: http://tech.snmjournals.org/content/32/2/60.full

[51] P. Pretorius and M. King, "A Study of Possible Causes of Artifactual Decreases in the Left Ventricular Apex with SPECT Cardiac Perfusion Imaging," *IEEE Transactions on Nuclear Science*, vol. 46, no. 4, pp. 1016–1023, 1999.

[52] A. Bitarafan-Rajabi, H. Rajabi, F. Rastgou, and A. Sharafi, "Effect of respiratory motion on quantitative myocardial gated SPECT : a simulation study," *Annals of Nuclear Medicine*, vol. 23, pp. 587–593, 2009.

[53] P. Bruyant, B. Feng, P. Pretorius, and M. King, "Impact of Respiratory Motion Compensation in Cardiac SPECT When Attenuation Maps Are Not Motion-Compensated," in *Nuclear Science Symposium Conference Record*, vol. 4, 2004, pp. 2941–2945.

[54] A. Pitman, V. Kalff, B. VanEvery, B. Risa, L. Barnden, and M. Kelly, "Contributions of subdiaphragmatic activity, attenuation, and diaphragmatic motion to inferior wall artifact in attenuation-corrected Tc-99m myocardial perfusion SPECT," *Journal of Nuclear Cardiology*, vol. 12, no. 4, pp. 401–9, 2005.

[55] A. Pitman, V. Kalff, B. VanEvery, B. Risa, L. Barnden, and M. Kelly, "Effect of mechanically simulated diaphragmatic respiratory motion on myocardial SPECT processed with and without attenuation correction," *Journal of Nuclear Medicine*, vol. 43, no. 9, pp. 1259–67, 2002. [Online]. Available: http://jnm.snmjournals.org/content/43/9/1259.full

[56] K. Cho, S. Kumiata, S. Okada, and T. Kumazaki, "Development of respiratory gated myocardial SPECT system," *Journal of Nuclear Cardiology*, vol. 6, no. 1, pp. 20–28, 1999.

[57] W. Segars, D. Lalush, and B. Tsui, "A realistic spline-based dynamic heart phantom," *IEEE Transactions on Nuclear Science*, vol. 46, no. 3, pp. 503–506, 1999. [Online]. Available: http://www.bme.unc.edu/~wsegars/M5-3.pdf

[58] ——, "Modeling Respiratory Mechanics in the MCAT and Spline-Based MCAT Phantoms," *IEEE Transactions on Nuclear Science*, vol. 48, no. 1, pp. 89–97, 2001. [Online]. Available: http://noodle.med.yale.edu/zubal/library/TsuiPhan.pdf

[59] W. Segars and B. Tsui, "Study of the Efficacy of Respiratory Gating in Myocardial SPECT Using the New 4-D NCAT Phantom," *IEEE Transactions on Nuclear Science*, vol. 49, no. 3, pp. 675–679, 2002.

[60] W. Segars, S. Mok, and B. Tsui, "Investigation of Respiratory Gating in Quantitative Myocardial SPECT," *IEEE Transactions on Nuclear Science*, vol. 56, no. 1, pp. 91–96, 2009.

[61] G. Kovalski, O. Israel, Z. Keidar, A. Frenkel, J. Sachs, and H. Azhari, "Correction of Heart Motion Due to Respiration in Clinical Myocardial Perfusion SPECT Scans Using Respiratory Gating," *Journal of Nuclear Medicine*, vol. 48, no. 4, pp. 630–636, 2007. [Online]. Available: http://jnm.snmjournals.org/content/48/4/630

[62] J. Mitra, J. McNamara, K. Johnson, J. Dey, and M. King, "Estimation of rigid-body and respiratory motion of the heart for SPECT motion correction," vol. 7. Ieee, 2007, pp. 3570–3576.

[63] J. Mukherjee, J. McNamara, K. L. Johnson, J. Dey, and M. King, "Estimation of Rigid-Body and Respiratory Motion of the Heart From Marker-Tracking Data for SPECT Motion Correction," *IEEE Transactions on Nuclear Science*, vol. 56, no. 1, pp. 147–155, 2009.

[64] W. Segars, G. Sturgeon, S. Mendonca, J. Grimes, and B. Tsui, "4D XCAT phantom for multimodality imaging research," *Medical Physics*, vol. 37, no. 9, pp. 4902–4915, 2010.

[65] W. Segars and B. Tsui, "MCAT to XCAT: the evolution of 4-D computerized phantoms for imaging research," *Proceedings of the IEEE*, vol. 97, no. 12, pp. 1954–1968, 2009. [Online]. Available: http://deckard.mc.duke.edu/pdf/2010_Segars_ComputerizedPhantoms_IEEEProceedings.pdf

[66] "The 4D NCAT Phantom," W.P. Segars / Johns Hopkins Medicine, 2003. [Online]. Available: http://dmip.rad.jhmi.edu/people/faculty/Paul/Segars_research.htm#NCAT

[67] G. Lin, H. Hines, G. Grant, K. Taylor, and C. Ryals, "Automated quantification of myocardial ischemia and wall motion defects by use of cardiac SPECT polar mapping and 4-dimensional surface rendering," *Journal of Nuclear Medicine Technology*, vol. 34, no. 1, pp. 3–17, 2006.

[68] G. Germano, *Quantitative Analysis in Nuclear Medicine Imaging*. Springer, 2006, ch. 15 "Quantitative Analysis in Myocardial SPECT Imaging", pp. 471–193. [Online]. Available: http://www.almhnds.com/7/NM/5.pdf

[69] R. Dvorak, R. Brown, and J. Corbett, "Interpretation of SPECT / CT Myocardial Perfusion Images : Common Artifacts and Quality Control," *RadioGraphics*, no. p 2057, pp. 2041–2058, 2011.

[70] E. Garcia, T. Faber, C. Cooke, and R. Folks, *Emission Tomography: Fundamentals of PET and SPECT*. Elsevier Academic Press, 2004, ch. 24 "Computer Analysis of Nuclear Cardiology Procedures", pp. 541–549. [Online]. Available: http://www.scribd.com/doc/28417300/emission-tomography-the-fundamentals-of-PET-and-SPECT

[71] G. Germano, P. Kavanagh, P. Waechter, J. Areeda, S. VanKriekinge, T. Sharir, H. Lewin, and D. Berman, "A new algorithm for the quantitation of myocardial perfusion SPECT I: technical principles and reproducibility," *Journal of Nuclear Medicine*, vol. 41, no. 4, pp. 712–719, 2000. [Online]. Available: http://www.csaim.com/papers/germano-jnm-2000.pdf

[72] R. Deakin and D. Kildea, "A Note on Standard Deviation and RMS," *The Australian Surveyor*, vol. 44, no. 1, pp. 74–79, 1999. [Online]. Available: http://user.gs.rmit.edu.au/rod/files/publications/St_dev.pdf

Appendix A

D-SPECT Simulator

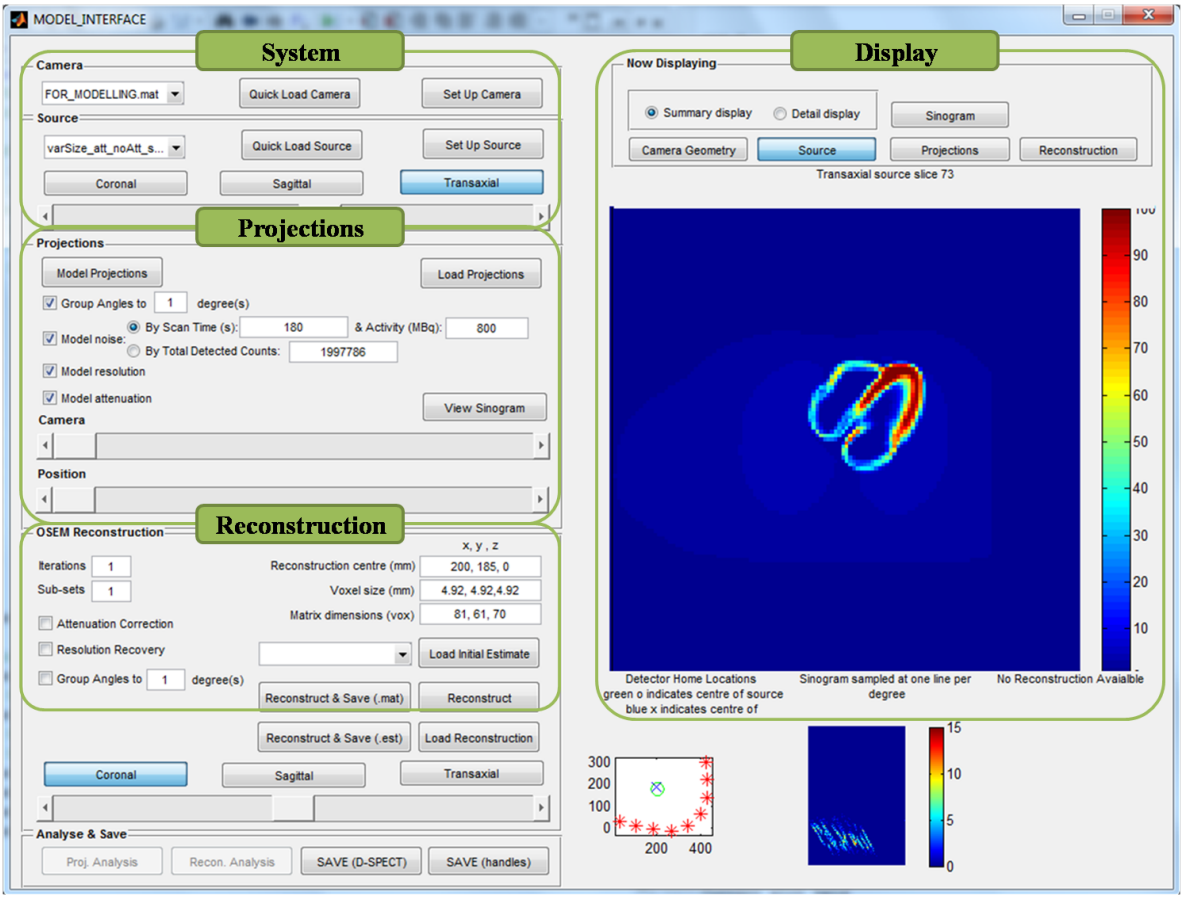

Figure A.1: Main interface of the D-SPECT *Simulator*. The four main parts of the *Simulator* are highlighted in green: system, projections, reconstruction and display. In the *system area*, the camera and the source of activity are defined; in the *projections area*, parameters regarding the simulation are set and projections can be estimated or loaded; in the *reconstruction area*, parameters regarding the reconstruction are set, and projections are reconstructed; in the *display area*, a display of the source, camera geometry, projections, sinogram or reconstructed image can be viewed.

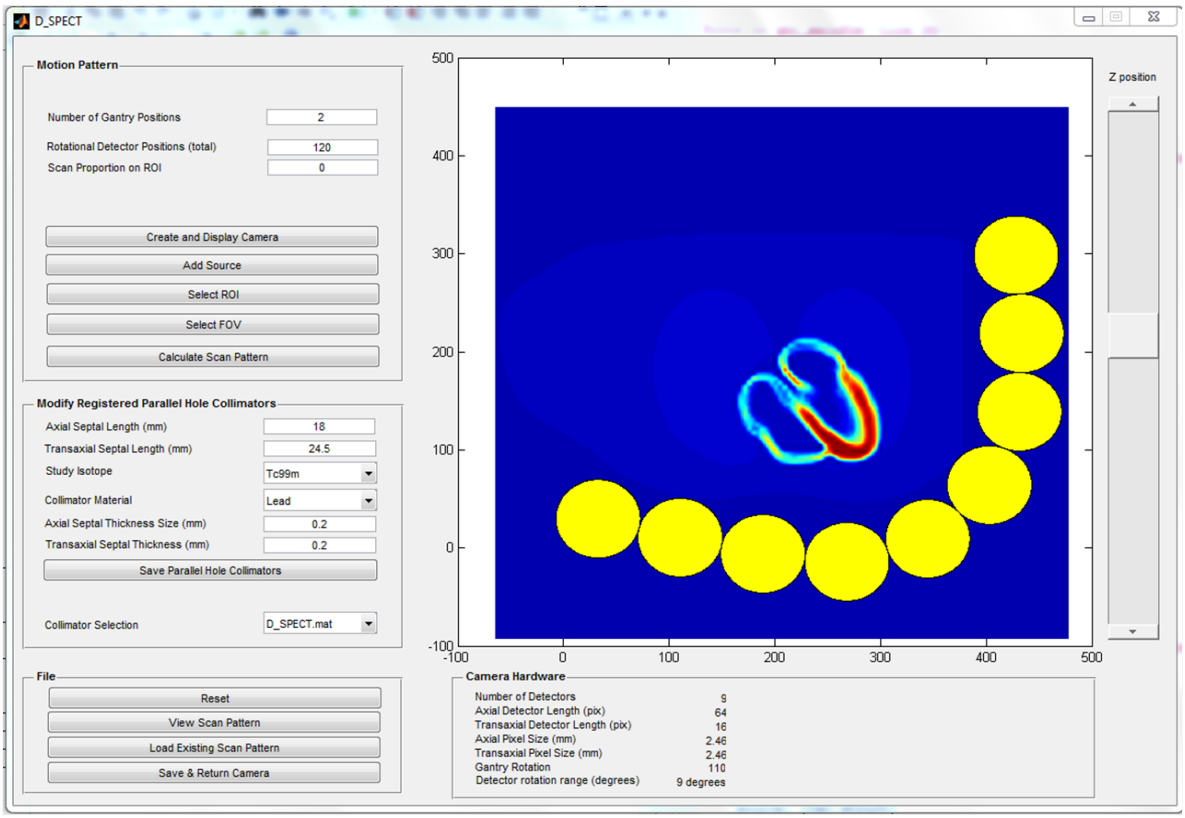

Figure A.2: `D_SPECT` interface of the D-SPECT *Simulator*. Parameters regarding the scanning pattern and the collimation system are defined here. Additionally it has a visualization area, which allows the user to check the system's geometry, and the calculated scanning pattern.

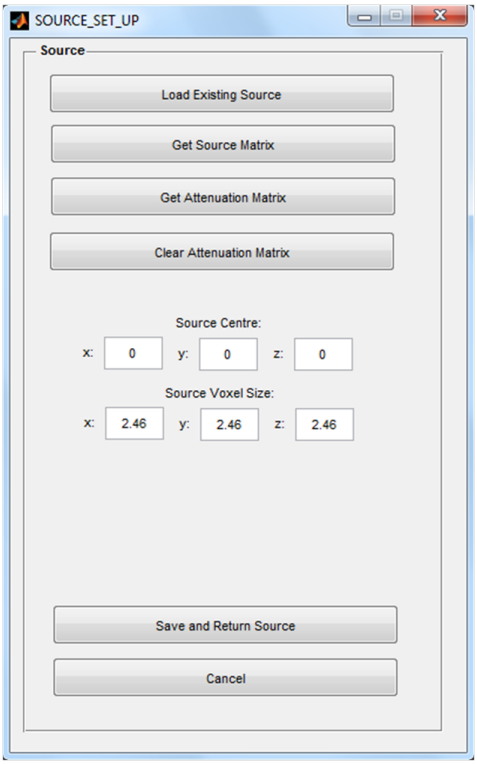

Figure A.3: `SOURCE_SET_UP` interface of the D-SPECT *Simulator*. Parameters regarding the source of activity position and matrix dimension are defined in this sub-interface.

Appendix B

Reconstruction Interface

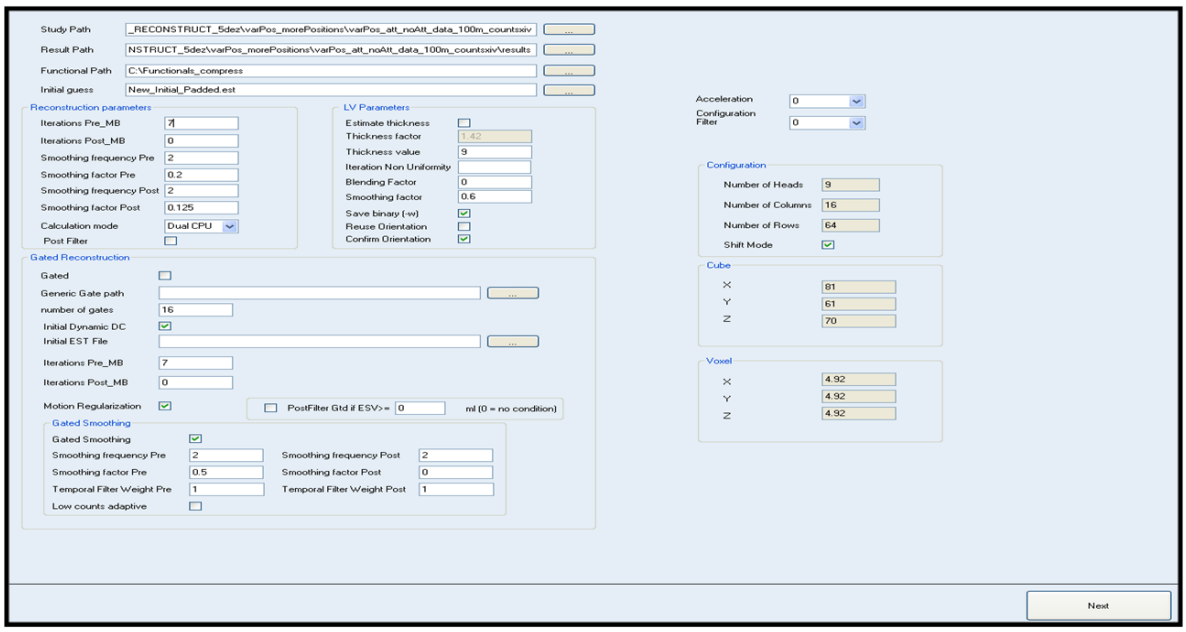

Figure B.1: Main interface of the D-SPECT reconstruction software. Parameters related to the OSEM-based reconstruction process are defined here.

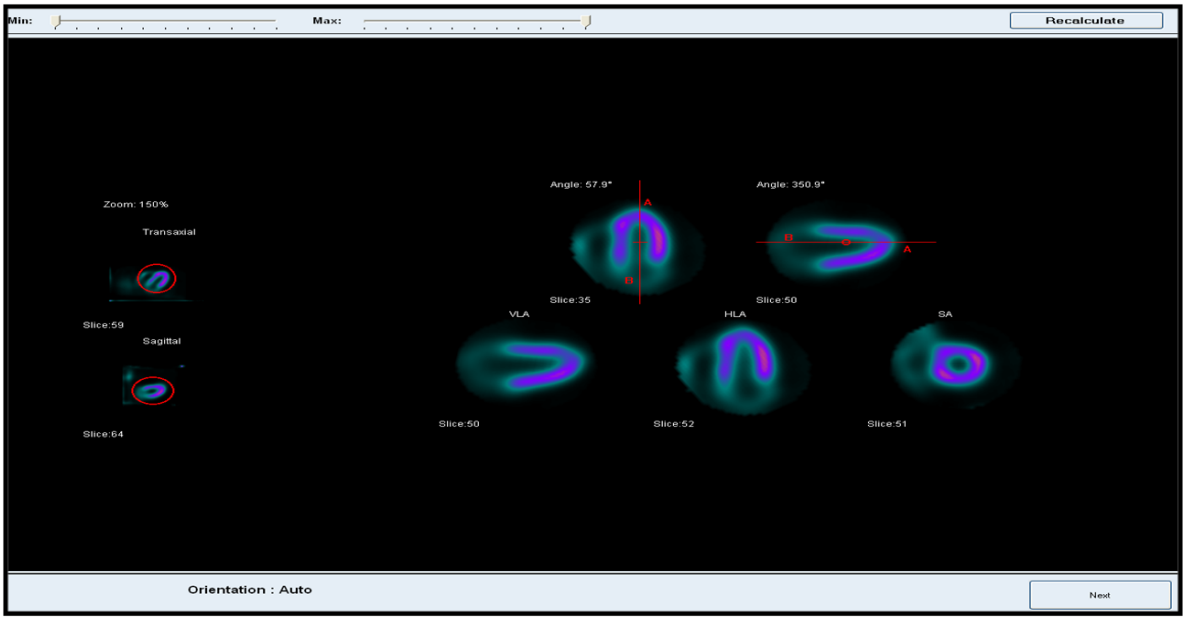

Figure B.2: Sub-interface of the D-SPECT reconstruction software. This interface allows the visualization of the reconstructed myocardium in the three standard views, as well as the manual re-orientation of the myocardial axes.